RWTH Aachen University
Chair and Institute for Flight System Dynamics

Master Thesis

Sustainable Space Logistics - Design of an On-Orbit Refuelling Infrastructure

presented by

Hannah Sophie BESSER

This thesis was submitted on
October 30, 2024

First Examiner: Univ.-Prof. Dr.-Ing. Dieter Moormann (RWTH)
Second Examiner: Sven Jackisch, M.Sc. (RWTH)

Supervision: Mathieu Udriot, M.Sc. (EPFL)
Max Hartmann, M.Sc. (RWTH)

This present thesis was submitted to the Institute of Flight System Dynamics.
It was carried out at the EPFL Space Center.

Abstract

To prevent further congestion of crucial orbits, more sustainable practices for space use are imperative. One potential solution is refuelling satellites in orbit to extend their lifespan and reduce debris accumulation by decreasing the number of defunct satellites from fuel depletion. GEO satellites, which allocate approximately 50% of their mass to propellant, are prime candidates for On-Orbit Refuelling (OOR) due to their long operational lifetimes, constrained orbital slots, and significant financial investment, offering potential for cost savings and enhanced utility.

This thesis work designs an OOR infrastructure tailored to service GEO satellites close to their End-of-Life (EOL) expecting depletion of onboard reserves. The infrastructure consists of a fuel depot and multiple servicing spacecrafts for in-space propellant transport. For a given set of GEO clients, selected launcher, servicer and depot design, the work optimizes the OOR scenario. It suggests various mission architectures with different fuel depot locations and numbers of servicers. The OOR design is the outcome of an iterative design procedure. Deployment and operation of the servicing architecture are simulated. Trajectories of servicers to rendezvous with clients are the result of a cost(Δv)-duration(Δt) trade-off. The logistics optimization problem is formulated as a Capacitated Vehicle Routing Problem (CVRP), and a tailored genetic algorithm minimizes mission cost for routing decisions. The OOR infrastructure design integrates trajectory selection, logistics optimization, and subsequent mission simulation.

The developments provide adaptive solutions, expandable to other servicing tasks, and can support long-term sustainable space logistics through scalable infrastructure design for guiding system of systems decisions. An OOR architecture for European GEO client satellites has been successfully optimized for total refuelling operation cost, while providing general design recommendations and pointing towards improvements in space logistics mission design.

Contents

List of Figures

List of Tables

List of Symbols

General Symbols

Υ		Vernal Equinox
a	[m]	Semi-major axis
b	[m]	Semi-minor axis
c	[J/kg]	Specific energy
E	[°]	Eccentric anomaly
e	[-]	Eccentricity
g	[m/s^2]	Gravitational constant
g	[-]	Generation
h	[m^2/s]	Angular momentum
h	[m]	Altitude
I	[s]	Impulse
i	[°]	Inclination
k	[-]	Number of complete orbits
m	[kg]	Mass
M	[°]	Mean anomaly
m	[-]	Number of servicers
N	[-]	Number

n	[-]	Number of clients
p	[m]	Semi-latus rectum
P	[s]	Period
PB	[-]	Probability
r	[m]	Radius
t	[s]	Time
u	[°]	Argument of latitude
v	[m/s]	Velocity

Greek Symbols

α	[°]	Phasing angle
ϵ	[-]	Structural coefficient
γ	[°]	Flight path angle
μ	[m^3/s^2]	Standard gravitational parameter
μ	[-]	Propellant ratio
ν	[°]	True anomaly
Ω	[°]	Right Ascension of the Ascending Node (RAAN)
ω_p	[°]	Argument of Perigee
Π	[-]	Payload ratio
τ	[s]	Reference time
Θ	[°]	Plane change angle

Subscripts

$\square_0$	Initial

$_{\nu}$	Tangential
$_{\mathrm{CX}}$	Crossover
$_{\mathrm{GEN}}$	Generations
$_{\mathrm{MUT}}$	Mutation
$_{\mathrm{POP}}$	Population
$_{\mathrm{rapid}}$	Rapid
$_{\mathrm{res}}$	Residual
$_{a}$	Apogee
$_{ch}$	Chaser
$_{c}$	Circular orbit
$_{e}$	Elliptic orbit
$_{f}$	Final
$_{kin}$	Kinetic
$_{pl}$	Payload
$_{pot}$	Potential
$_{p}$	Perigee
$_{p}$	Propellant
$_{r}$	Radial
$_{sp}$	Specific
$_{s}$	Structural
$_{tg}$	Target
$_{tot}$	Total
$_{t}$	Transfer

Abbrevations

A6	Ariane 6
ACO	Ant Colony Optimization
ADRIOS	Active Debris Removal and In-Orbit Servicing
AOCS	Attitude and Orbit Control System
Ap	Apogee
ATV	Automated Transfer Vehicle
CVRP	Capacitated Vehicle Routing Problem
DARPA	Defense Advanced Research Projects Agency
DLR	Deutsches Zentrum für Luft- und Raumfahrt
ECI	Earth-Centered Inertial
EOL	End-of-Life
ERM	European Refueler Module
ESA	European Space Agency
ESM	European Service Module
FLP	Facility Location Problem
GA	Genetic Algorithm
GEO	Geostationary Earth Orbit
GTO	Geostationary Transfer Orbit
IOD	In-Orbit Demonstration
ISAM	In-Orbit Servicing, Assembly and Manufacturing
ISRU	In-Situ Resource Utilization
ISS	International Space Station

ISTV	In-Space Transportation Vehicle
JAXA	Japan Aerospace Exploration Agency
LCA	Life Cycle Assessment
LEO	Low Earth Orbit
LRP	Location Routing Problem
M2M	Many-to-Many
MDVRP	Multiple Depot Vehicle Routing Problem
MEP	Mission Extension Pods
MEV	Mission Extension Vehicle
MGSRP	Multiple Geosynchronous Spacecraft Refueling Problem
MRV	Mission Robotic Vehicle
MWMP	Maximum Weight Matching Problem
NASA	National Aeronautics and Space Administration
NRHO	Near Rectilinear Halo Orbit
O2M	One-to-Many
O2O	One-to-One
OOP	Object-Oriented Programming
OOR	On-Orbit Refuelling
OOS	On-Orbit Servicing
OTV	Orbital Transportation Vehicles
P2P	Peer-to-Peer
Pe	Perigee
PMX	Partially Mapped Crossover
PoC	Proof-of-Concept

PSO	Particle Swarm Optimization
RAAN	Right Ascension of the Ascending Node
RAFTI	Rapidly Attachable Fluid Transfer Interface
RLV	Reusable Launch Vehicles
RRM	Robotic Refuelling Mission
RSGS	Robotic Servicing of Geosynchronous Satellites
SA	Simulated Annealing
SSTO	Single-Stage-To-Orbit
TCAT	Technology Combination Analysis Tool
TOF	Time of Flight
TSP	Travelling Salesman Problem
UML	Unified Modelling Language
VRP	Vehicle Routing Problem

1. Introduction

Within the last two decades, the number of objects in Earth orbits increased from around 7 500 to more than 35 000 in 2023 with increasing mass and density [25]. Satellite launches are projected to double space population by 2033 [46]. The status-quo heavily relies on one-time use and disposal [53], with a decrease in satellite design lifetime [24]. While planned constellations aggravate the situation in Low Earth Orbit (LEO), Geostationary Earth Orbit (GEO) slots are particularly limited due to their inherent orbital characteristics and specific applications. To prevent further congestion of crucial orbits and limit the collision risks through space debris, more sustainable space practices are imperative.

Space agencies are exploring new in-space economy concepts based on sustainable space logistics, giving rise to a paradigm shift in the design of space missions [58, 85, 87]. On-Orbit Servicing (OOS) allows to use assets of near-Earth locations more effectively, improving cost-benefit mission ratios [58]. It further assists deep space exploration. The use of in-orbit depots and in-space transportation infrastructure reduces the total mission cost of envisioned future missions by 40% [72]. Servicing not only extends operational lifetime, but also enhances mission design flexibility, satellite functionality, and overall reliability [53, 58]. A major cause of mission termination is the depletion of on-board fuel with the increase in system reliability and redundancy [12, 35, 55]. On-Orbit Refuelling (OOR) can broaden mission possibilities by enabling fuel-intensive manoeuvres, reducing manoeuvre durations, and enhancing overall manoeuvring capabilities. Reduced initial vehicle mass or increased payload capacity by reallocation of propellant mass to other critical subsystems can further extend mission potential. GEO satellites are prime candidates for OOS. Studies conclude that the telecommunications industry is highly interested in OOR [27]. The NASA Goddard Space Flight Center [58] recommends GEO satellite refuelling as a primary step for OOS. GEO satellites are particularly well-suited for in-orbit refuelling due to their enhanced durability, significant operational costs, and the substantial proportion of their mass dedicated to propellant [53]. GEO refuelling might lead to mission cost savings of $300 - 1000$ million $ [23].

No fully operational OOS mission has been realised yet, despite being envisioned within the space sector for more efficient and sustainable space utilisation. Designing such a servicing architecture is highly complex and dependent on specific use cases, necessitating a system of systems approach. This work aims to develop a tool to tackle this challenge. The topology of an OOR infrastructure to extend the lifespan of 15 European GEO satellites by five years is to be determined and evaluated for performance. The servicing infrastructure consists of a fuel depot and multiple servicing spacecrafts for in-space propellant transport. The placement of the fuel depot and the number of servicing vehicles for nominal operation are studied design variables. The design aims at minimizing orbital transfer costs in refuelling operations. An iterative design procedure combining mission design aspects and logistical concepts is developed. Deployment and operation of the servicing architecture are simulated following logistics optimization. A trade-off of orbit manoeuvre costs in terms of Δv and durations is integrated within the trajectory design of the servicing vehicles. The logistics optimization problem is formulated as a Capacitated Vehicle Routing Problem (CVRP), and a tailored genetic algorithm minimizes mission cost for routing decisions. The OOR infrastructure design, integrated into the Technology Combination Analysis Tool (TCAT) at the EPFL Space Center, combines trajectory selection, logistics optimization, and mission simulation for performance evaluation.

Chapter 2 includes a review of past and future OOS and OOR missions, outlines the current state of research in servicing infrastructure design methodologies, and introduces relevant theoretical considerations in spaceflight and space logistics.

Chapter 3 presents the use case for the refuelling architecture and describes the corresponding OOR mission scenario. Herein, design variables, parameters and performance indicators are defined, launcher and clients selected, and active spacecrafts configured. It further develops the methodology employed in this thesis. The approach to trajectory design and manoeuvre selection is derived and a genetic algorithm is tailored for optimization of the logistics scenario. Finally, the chapter presents the implementation of the methodology within the TCAT tool outlining its extensions.

Chapter 4 evaluates results for transfer trajectories, logistics optimization, and OOR design. Herein, a Δv-optimal design is identified, general design recommendations for servicing missions are proposed, and potential limitations and improvements are discussed.

Chapter 5 concludes the findings of this work and outlines directions for future work on OOS mission design.

2. Theoretical Background

Providing context for this work, this chapter first reviews the state of the art in On-Orbit Servicing and Refuelling missions, including historical demonstrations and future visions and concepts in section 2.1.1. Subsequently, previous research related to the design of On-Orbit Servicing and Refuelling missions is discussed in section 2.1.2. This review aids in identifying existing knowledge gaps, establishing the thesis objective, and situating the results within the framework of prior studies in chapter 2.1.3. Lastly, the chapter establishes the theoretical foundation of orbital spaceflight and logistics optimization, enabling the development of a system of systems, optimization-oriented approach to On-Orbit Refuelling operations and infrastructure design in section 2.2 and 2.3.

2.1. State of the Art in On-Orbit Servicing and Refuelling

Arney et al. [4] characterize In-Orbit Servicing, Assembly and Manufacturing (ISAM) as an emerging set of capabilities enabling inspection, repair, upgrade, assembly, relocation, and construction of space assets. ISAM is further classified into On-Orbit Servicing (OOS), On-Orbit Assembly, and On-Orbit Manufacturing, with OOS specifically referring to inspection, maintenance, refuelling, repair, upgrade, and relocation [78]. Within this context, servicing refers to any modification of a spacecraft following its launch [4]. On-Orbit Refuelling (OOR) is defined as the operation of refilling the fuel tank of a client satellite using a servicing spacecraft while in orbit. This involves the servicer performing rendezvous and docking with the client satellite [20]. Refuelling and fluid transfer are classified as one of the eleven ISAM key capabilities [4]. ESA favours the term ‘refilling’ over ‘refuelling’ as it covers all types of fluid transfers [86].

In this work, an On-Orbit Refuelling infrastructure consists of a number of servicing spacecrafts, so-called servicers, and a fuel depot. The notion of On-Orbit Refuelling mission refers to the deployment and operation of the OOR infrastructure to provide refuelling services to clients in space. The design of the OOR infrastructure involves determining key design variables that define its configuration and operational capabilities.

2.1.1. On-Orbit Servicing and Refuelling Operations and Missions

On-Orbit Refuelling has been demonstrated in previous space missions, albeit on a limited scale. Currently, no infrastructure exists that provides OOR services on a large scale, extending beyond individual fuel transfers. However, the development of such infrastructure is a key objective for both space agencies and private entities. Other On-Orbit Servicing missions, such as Active Debris Removal (ADR) and Life Extension Missions, pose some of the same technical challenges and concepts of operation as OOR. Therefore, the past and forthcoming missions illustrated in figure 2.1 are pertinent to the present study.

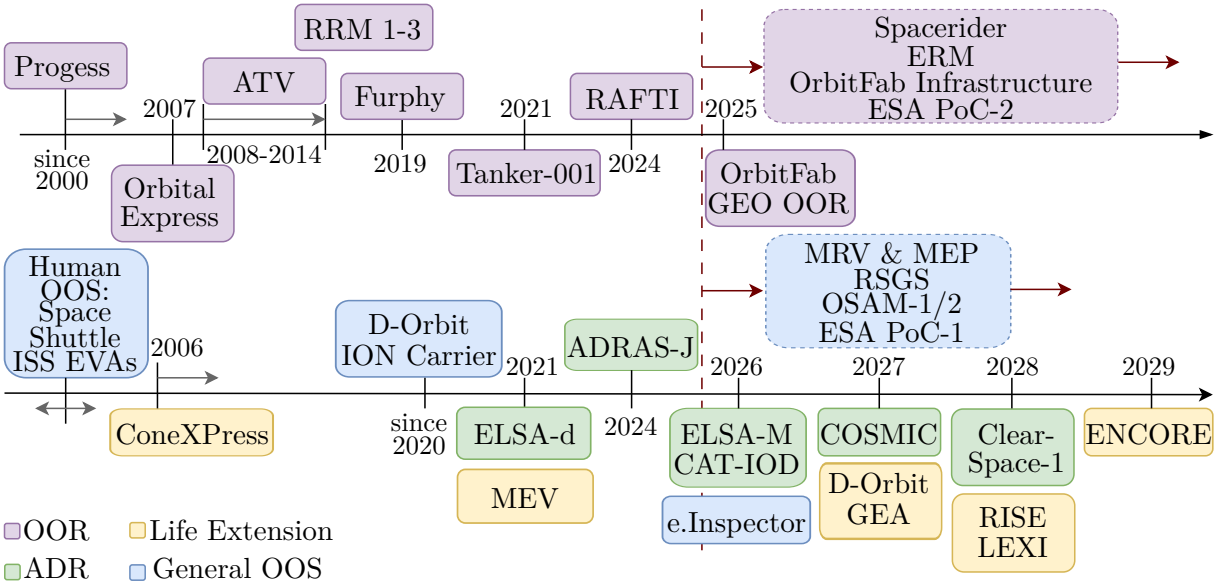

Figure 2.1.: On-Orbit Refuelling (top) and Servicing (bottom) Missions

The International Space Station (ISS) resupply missions represent a category of servicing missions with extensive space heritage, including fluid transfer capabilities. The ESA Automated Transfer Vehicle (ATV) supplied the ISS with water, propellant and air between 2008 and 2014. Building upon the technology demonstrated in this mission, the European Service Module (ESM) has been developed for the Orion Capsule supporting NASA's Artemis program. Additionally, the European Refueler Module (ERM), is set to enhance the Lunar Gateway's supply capabilities. Since 2000, the Russian Progress spacecraft consistently supplies the ISS with water, hydrazine, and nitrogen tetroxide [4]. Progress MS delivers up to 850 kg of propellant [31], while Thianzhou-2 transported 1.95 t of propellant to the Chinese Space Station [45]. In 2019, OrbitFab successfully resupplied the ISS with water as part of the Furphy project [9]. Fluid transfer of storable liquids like hydrazine has been demonstrated in missions such as the Robotic Refuelling Mission (RRM) [57]. However, cryogenic fuel transfer remains unproven in space, despite RRM-3

demonstrating zero-boil-off cryogenic fuel storage in 2019 [4]. The Orbital Express mission, conducted by the Defense Advanced Research Projects Agency (DARPA) in 2007, successfully transferred hydrazine between two spacecrafts and demonstrated autonomous rendezvous and docking capabilities [53]. This mission marked the first successful end-to-end robotic satellite servicing operation [58]. In 2021, OrbitFab launched Tanker-001 Tenzing, the first fuel tanker in space, into LEO as part of their initiative to develop an in-space propellant chain [9]. Tanker-001 is a small satellite designed to demonstrate the capabilities of OrbitFab's Rapidly Attachable Fluid Interface (RAFTI) system in orbit. The refuelling adapter qualified in 2024 provides a hydrazine flow rate of 0.505 kg/min [62]. Figure 2.2 shows components of OrbitFab's refuelling architecture in development including fuel depots and shuttles [32]. It is to day the sole effort of establishing an entire refuelling logistics network in space [38]. Hydrazine refuelling services in GEO are projected for 2025, initially targeting U.S. Space Force satellites and subsequently Astroscale's servicer LEXI [60, 73].

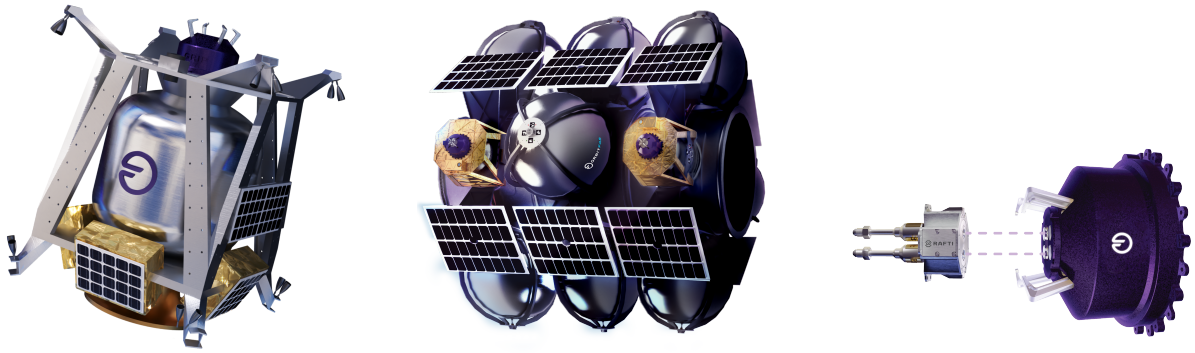

(a) Shuttle **(b)** SuperDepot **(c)** RAFTI Interface

Figure 2.2.: OrbitFab Refuelling Infrastructure Components [61]

ESA envisions a paradigm shift towards a European In-Space Transportation Ecosystem, ultimately aiming to establish a circular space economy [85]. To support this vision, ESA leads Proof-of-Concept (PoC) studies with the European SpaceTech industry developing enabling technologies for In-Space Transportation Vehicle (ISTV) solutions. PoC-1 contracted to OHB Systems and The Exploration Company aims at demonstrating key enabling in-orbit transport capability of automatic rendezvous and docking between two cooperative orbital systems [29]. The Exploration Company's reusable and refuelable Nyx vehicle has a mass of 10.5 t, while OHB proposes an ISTV with a mass of approximately 1.3 t [8]. A recently selected consortium will develop technologies for in-orbit cryogenic propellant storage and refilling for PoC-2 [64, 86]. The ESA ADRIOS programme could benefit from these advancements, encompassing missions for ADR and OOS, such as

e.Inspector, ClearSpace-1, CAT-IOD, RISE, and ENCORE, all planned for launch before 2030 [11]. In parallel, SpaceRider, Europe's first reusable transportation system to LEO, is developed. It will serve as an uncrewed robotic lab for In-Orbit Demonstration (IOD) of servicing technologies and perform OOS tasks like refuelling in future iterations [10, 26].

ADR servicing missions are not only in development, but already operational in orbit. Astroscale launched JAXA's ADRAS-J in 2024 to perform the first ADR in 2027 and plans launching the first multi-removal mission COSMIC in the same year targeting UK satellites [73]. With ELSA-d, Astroscale proved magnetic capture of an object in-orbit in 2021, preparing for ADR of an Eutelsat Oneweb satellite with ELSA-M [73]. ESA's first ADR mission is ClearSpace-1 for uncooperative and unprepared removal of PROBA-1 in 2028 [81]. CAT-IOD on the contrary aims at developing a system for prepared removal of six Copernicus Sentinel satellites [69]. The e.Inspector mission will conduct a fly-around inspection of space debris using a CubeSat in 2026, preparing such missions [52].

Life extension missions provide Attitude and Orbit Control System (AOCS) and propulsion or fuel storage capacities to satellites. As early as 2006, ESA and Orbital Recovery initiated the ConeXPress project to explore extending the lifespan of GEO telecommunications satellites by up to 12 years [12]. The Mission Extension Vehicle (MEV) doubled operational lifetime of two Intelsat GEO satellites by providing repositioning and station-keeping in 2020 and 2021 [53]. MEV-2 operates in GEO with a mass of 2.9 t [49]. Northrop Grumman's Mission Robotic Vehicle (MRV) supports tasks like inspection, repair, relocation, and ADR. It is planned to attach 400 kg Mission Extension Pods (MEP) to satellites for six years of orbit control [4]. The DARPA Robotic Servicing of Geosynchronous Satellites (RSGS) project further enhances GEO satellite servicing capabilities [30]. RISE is ESA's first IOS mission to perform GEO satellite life extension in 2028 with a D-Orbit servicer [28]. The GEA Logistics Vehicle, set for a 2028 launch, is designed to transport 2.5 t clients to GEO and perform OOS. The subsequent ENCORE mission aims to develop a refuelable OOS spacecraft for 2029 [16].

2.1.2. Review of Design of On-Orbit Servicing and Refuelling Missions

Research efforts in the design of OOS and OOR missions are categorisable in their application and methodology. Missions are designed to address various scenarios and use cases, including exploration endeavours and servicing in near-Earth orbits, the primary

focus here. Researchers adopt distinct design methodologies, typically centred around optimisation frameworks with different objectives. The logistical scenario and study focus drive design variables, considerations, and constraints of the servicing architecture. These variations, in turn, influence the modelling of OOS infrastructure including astrodynamics considerations, logistics problem formulation, and solution algorithms.

On-Orbit Servicing Applications and Scenarios

On-orbit servicing applications and scenarios guide the design of supporting infrastructure, divided into two primary areas: space exploration missions and near-Earth orbit servicing. Both mission types explore various servicing capabilities. Researchers find significant improvements for initial mass in exploration mission payloads through the use of new logistics concepts as detailed in A.1. Servicing in near-Earth orbits is investigated in various use cases. In an early study, Gürtuna and Trépanier [35] consider refuelling 100 satellites in LEO, MEO and GEO studying the placement of servicing platforms stationed at a fuel depot. Similarly, Sorenson and Pinkley [80] and Bourjolly et al. [6] schedule the refuelling of clients in all these orbits in a single mission. Meng et al. [55] explore different deployment methods concluding that same orbit deployment is advantageous. Luu and Hastings [53] review OOS advances for LEO constellations. The emergence of Mega Satellite constellations demands scalable OOS solutions [53], with Sirieys et al. [78] optimizing a servicing fleet for refuelling the Iridium constellation in LEO. The servicing of navigation constellations Galileo and GPS in MEO is also investigated [77]. Alfriend et al. [1] name robotic servicing of GEO targets as a second potential use case in addition to constellations with potential to reduce system cost. GEO refuelling remains a key research focus [1, 14, 48, 59, 100–102, 104]. An optimization of a servicing infrastructure is developed by Du Sarton Jonchay et al. [20] for providing a range of servicing capabilities to a GEO fleet. The study includes both short- and long-term use cases for deterministic and random servicing needs, which is complemented by research focusing on GEO OOS servicing demands [94]. In studies targeting operational level, the concrete application and ISAM capabilities are not relevant [21, 22, 75, 88]. Accordingly, Verstraete et al. [94] take into account multiple ISAM functions in optimizing an OOS infrastructure. Refuelling via formation flying has also been explored [5], as has refuelling in SSO [105].

Space agencies are developing holistic logistic strategies for future space economy systems as illustrated in figure 2.3. ESA's 2025-2050 roadmap envisions a 'Hub and Spoke' logistics network with payloads launched to high parking orbits by Reusable Launch Ve-

hicles (RLV). Satellites reach their final orbits via ISTVs, which is identified as the most efficient solution. ISTVs are made reusable through refuelling at depots [85, 86]. JAXA's 2040 roadmap similarly emphasizes a high-frequency, reusable transportation system to LEO, supported by Orbital Transportation Vehicles (OTV) [87]. The post-2040 Interorbital Transfer Network envisions Single-Stage-To-Orbit (SSTO) launchers, OTVs, OOS vehicles, space depots, and space stations. NASA's roadmap envisions a 'Space Superhighway', an in-space logistics network enabled by ISAM capabilities, featuring commercial launch vehicles, resupply tankers, orbital depots, and in-space tugs. This evolution begins with refuelling, advances to debris removal, and ultimately leads to depot establishment for deep space missions [84]. Roohi et al. [72] explore infrastructure concepts based on scenarios proposed by NASA and private companies. Their 2035-2055 case study covers servicing for LEO and GEO satellites, Mars and Moon missions, and space stations.

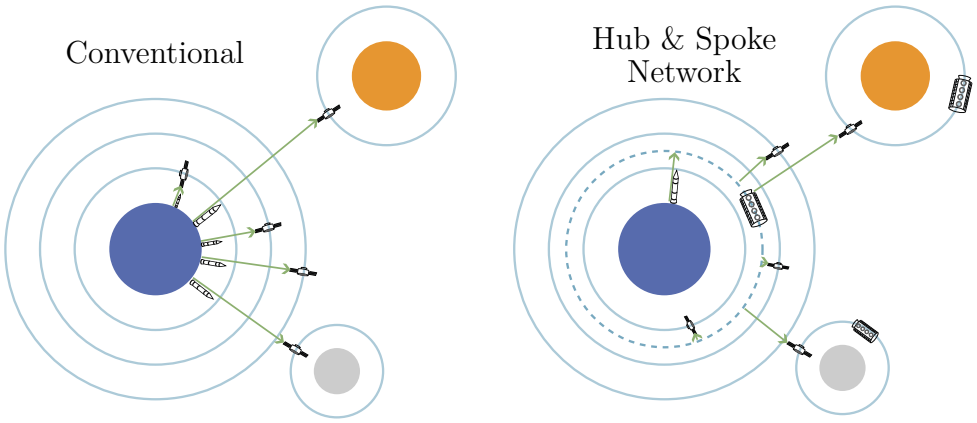

Figure 2.3.: Vision for Future Space Logistics Economy [85]

On-Orbit Servicing Design Methodology

Logistics problems are typically analysed at strategic, tactical, or operational level [35]. Strategic decisions address numbers of servicing spacecraft, orbital placement, or propulsion systems, while tactical analysis concerns annual service planning. Operational analysis optimizes routing and scheduling. Space logistics research to date focuses on strategic and operational levels.

The primary objective across most space servicing architecture designs is mission cost minimization, either through combined economic or operational costs measured by spaceflight performance indicators such as Δv as summarized in table 2.1. Architectures that minimize economic cost often use Earth-based resupply as the comparison baseline [72, 77]. Cost objectives typically include design, development, and testing expenses, as well

as infrastructure launch and operational supply costs [72]. Sirieys et al. [78] optimize the combined economic cost of manufacturing, launch, and operation, alongside infrastructure performance in extending satellite lifetimes. By including launch and insertion costs, different facility locations can be compared [77]. To maximize profit, revenue from extended satellite operations is considered [14, 20]. Assessing risk alongside revenue and time penalties allows for more informed decision-making [94]. A multi-objective optimization targeting economic cost simultaneously minimizes refuelling response time [55]. Research at the operational logistics level typically formulates the objective as minimizing Δv required for orbital manoeuvres along refuelling routes. The establishment cost of space infrastructure components extends operational evaluation [100, 104]. Bourjolly et al. [6] optimize both Δv and mission duration individually. Minimizing fuel consumption for refuelling missions is another approach on operational level [5, 102]. Mission duration and fuel consumption are minimized across some multi-objective studies [18, 44, 99]. In peer strategies, the objective is to minimize fuel distribution deviations for fuel equalization [22, 88]. More recently, maximization of the weighted number of refuelling tasks completed is performed by Sorenson and Pinkley [80].

Table 2.1.: Objectives of OOS Infrastructure Design Optimization

Optimization Objective	Literature
Economic cost	[14, 20, 72, 77, 78, 94]
Refuelling operation Δv	[1, 6, 19, 35, 42, 59, 74, 88, 98, 100, 101, 103–105]
Fuel consumption	[5, 18, 22, 44, 88, 99, 102]
Multi-objective with time	[6, 18, 44, 55, 99]
Multi-objective with depot cost	[100, 104]

The architecture scenario type determines the sizing of OOS infrastructure, evolving from One-to-One (O2O) refuelling scenarios to Many-to-Many (M2M) architectures, where multiple servicers support multiple clients as depicted in figure 2.4. In Peer-to-Peer (P2P) strategies, satellites act as servicers, moving within constellations to redistribute fuel [75]. These can be either cooperative, involving mutual satellite repositioning, or non-cooperative [21]. Cooperative refuelling shows potential fuel savings of up to 27% [19]. Table 2.2 highlights the corresponding studies. Tsiotras and Nailly [88] compare O2M and P2P refuelling strategies, concluding that a mixed approach can reduce total refuelling time and save fuel for large satellite constellations. X. Chen and Yu [14] compare O2M, M2M, and mixed P2P strategies, suggesting that the most efficient scenario depends on mission objectives and constraints.

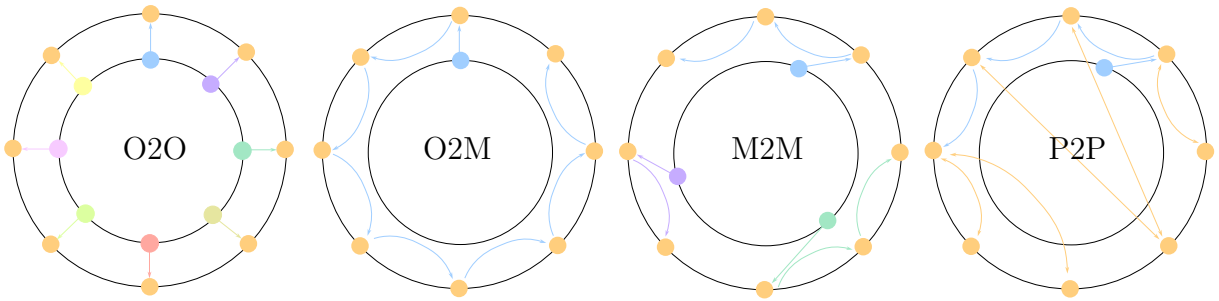

Figure 2.4.: Scenario Types for OOR Infrastructures

Number, distribution or allocation of servicers are frequent architecture design choices [78, 100]. The simplest problem involves optimizing the visiting order of a single servicer for multiple targets [1, 74], while P2P mission planning addresses task assignment and trajectory optimization for each servicing pair [98]. Multi-objective studies incorporate refuelling sequences, service times, and orbital transfer times as key variables [18, 44, 48, 99]. Daneshjou et al. [18] further investigate initial orbit locations, with the number of servicing and target satellites fixed. Several studies address the optimal placement of fuel depots, as well as the capacities of supporting infrastructure as detailed in table 2.2. Kong and Zhou [48] simultaneously optimize depot locations, task assignments, visitation order, and time distribution of orbital transfers. X. Chen and Yu [14] further incorporate servicer dry mass as a design variable, alongside fuel mass and mission sequence. Shimane et al. [77] optimize the number of facilities, their orbital slots, and client allocations. The arrangement of multiple fuel stations, incorporating servicer capacity constraints for defining servicing radii, and clustering of reachable targets, demonstrates that the number and location of depots significantly impact the refuelling schedule [104, 105].

Table 2.2.: Servicing Architecture Scenarios

Architecture Characteristics	Literature
O2M	[1, 5, 6, 14, 19, 42, 44, 88, 99, 101, 102, 105]
M2M	[5, 14, 18, 35, 48, 74, 77, 78, 80, 100, 104]
P2P	[14, 21, 22, 75, 76, 88, 98]
Propellant depot	[6, 14, 35, 48, 55, 59, 77, 80, 100, 102, 104, 105]
Infrastructure capacities	[14, 48, 55, 72, 80, 100, 104, 105]

Models of OOS infrastructure represent logistic structures as graph networks. Facility location problems focus on positioning depots at selected nodes [35, 77]. While most models are static, some incorporate transient demand and supply variations [72]. Sorenson and Pinkley [80] are the first to introduce time-evolving depot and client locations for optimizing refuelling schedules, while O'Brien and Sichler [59] evaluate high- and low-thrust

propulsion systems under time constraints. Logistical Problem Formulation involves framing the logistical scenario as a well-known problem, enabling the application of standard solution methods for optimization. The Vehicle Routing Problem (VRP) addresses network optimization by determining optimal routes for multiple vehicles serving all clients. Gürtuna and Trépanier [35] first introduced a space-based VRP, which has since been adapted for various space applications [59]. In GEO, where targets remain static, the VRP can be effectively formulated [104]. The Travelling Salesman Problem (TSP) is a specific VRP with one servicer, commonly used to model O2M scenarios [1, 42, 103]. Bourjolly et al. [6] extend the TSP to a time-dependent, moving target problem. More recently, Kong and Zhou [48] advanced the VRP to a Multiple Depot VRP (MDVRP) and further developed it into the complex Multiple Geosynchronous Spacecraft Refuelling Problem (MGSRP). The Facility Location Problem (FLP) optimizes the placement of servicing facilities [77], while the Location Allocation Problem simultaneously searches for facility locations and assigns demand points [104, 105]. Recent studies combine VRP and FLP into the Location Routing Problem (LRP) [100].

All of these problems are NP-hard, requiring advanced algorithms for efficient solutions. Logistics problems are typically formulated as linear or non-linear programming problems. Conventional solvers, such as Gurobi, CPLEX [77], and the simplex method [44], address linear programming problems. Metaheuristic methods handle more complex problems, such as the Clarke and Wright algorithm used for VRP solutions [35]. Heuristic methods are employed to tackle complex optimization problems involving non-linear functions and both discrete and continuous variables. Particle Swarm Optimization (PSO) is used for optimizing refuelling sequences and multi-objective problems [14, 18, 55]. Ant Colony Optimization (ACO) is applied to solve the Location Routing Problem (LRP) [100]. Studies focusing on multi-objective optimization suggest that Genetic Algorithms (GA) are more effective than PSO or Simulated Annealing (SA) [78]. GA is utilized to solve the VRP [59], the TSP [42, 96], and to determine refuelling order across various scenarios [5, 44, 94, 102, 103]. GA also applies to exploration mission optimization in multi-objective frameworks [33, 43], with variations [99, 105] and hybrid approaches [48]. Combining GA with random-search methods improves solutions but increases computation time [102].

Astrodynamics considerations in literature primarily address orbital manoeuvres performed by spacecraft. These are simplified in most studies to Hohmann transfers for in-plane changes and out-of-plane adjustments via the sine law. Phasing orbits enable adjustments in true anomaly, relying on differences in orbital period [53]. As illustrated

in table 2.3, these techniques form the foundation of orbital transfer modelling for space logistics problems. For the O2M problem, theoretical solutions are derived. When only out-of-plane manoeuvres are used, which are typically more fuel-intensive, the solution to the TSP involves identifying the path of minimum distance through the projection points of the client satellites' angular momentum vectors onto the equatorial plane [1]. Alternatively, if only phasing manoeuvres are applied, without out-of-plane changes, the optimal sequence for the O2M scenario is the orbit-wise or counter-orbit-wise sequential order, minimizing the total sweep angle as the servicer returns to its original slot [74].

Table 2.3.: Orbital Manoeuvres in Space Logistics Modelling

Orbital Manoeuvre	Literature
In-plane manoeuvre: Hohmann transfer	[35, 53, 78]
Phasing manoeuvres	[17, 18, 35, 44, 48, 53, 55, 74, 78, 80, 99]
Lambert problem	[5, 18, 22, 88]
J2 perturbations in LEO	[44, 53, 99]
Out-of-plane manoeuvres	[1, 48, 55, 100, 102]
Simultaneous in-plane and out-of-plane	[35, 48, 80]

2.1.3. Knowledge Gap

Current research in space logistics optimization predominantly focuses on minimizing economic costs or scheduling operational logistics, often neglecting a thorough evaluation of overall system performance, even within multi-objective optimization frameworks. However, comprehensive mission analysis is essential for informed decision-making during the early stages of design. Ehn [23] evaluates OOR performance through technology roadmapping, emphasizing technological factors but without integrating logistical considerations. This thesis aims to develop a methodology that allows for the flexible incorporation of spacecraft and mission parameters, preferences, and constraints into the scenario definition for the optimization process. The optimized architecture is then subjected to simulation, enabling a more holistic performance assessment not only in terms of the optimization objective but also across a range of mission performance indicators.

Launch and vehicle deployment costs are often simplified, with few studies accounting for orbital transfers. However, refuelling schemes are influenced by depot opening costs and locations [100]. This thesis extends the analysis by considering launcher performance, fairing volume, and insertion costs from GTO to orbit. Another aspect overlooked in

current architecture design is the integration of operational servicer transfers with additional OOR phases. Further, a simultaneous analysis of both nominal and rapid response scenarios has not been conducted previously. A comprehensive OOR mission simulation addressing the current gap is to be developed.

Most studies simplify orbital transfer cost computations using Hohmann transfers, phasing or plane changes, overlooking the variability in refuelling mission design that arises from complex trajectory decisions. These methods are further inadequate for non-circular orbits requiring simultaneous in-plane and out-of-plane changes. Furthermore, the critical trade-off between Δv and Δt, a fundamental aspect of space mission design, is not considered within trajectory design itself, though it is crucial for selecting manoeuvres that align with broader system design and operational constraints. This thesis introduces a trajectory selection method based on a $\Delta v/\Delta t$ priority prior to logistical optimization.

2.2. Fundamentals of Spaceflight

To address the objectives stemming from identified research gaps, presentation of relevant theoretical models and considerations is necessary. Identifying promising research directions, this thesis adopts methodological approaches highlighted blue in tables 2.1, 2.2, and 2.3: This thesis integrates strategic decisions on the number of servicing vehicles and depot placement with operational optimization for Δv within the framework of a M2M scenario for refuelling of GEO satellites. The established scenario and use case are further detailed in section 3.1. This chapter presents fundamentals of orbital mechanics in section 2.2.1 and spacecraft design principles as well as context for launchers and GEO satellites in section 2.2.2. Thereafter, chapter 2.3 outlines the Vehicle Routing Problem as logistics framework for this thesis and genetic algorithms as a potential solution approach.

2.2.1. Orbital Mechanics

Ideal Earth orbits are characterized as circular, a specific case of elliptical orbits with zero eccentricity. The spacecraft trajectories in this thesis are represented by elliptical orbits, as depicted in figure 2.5. The perigee (Pe) denotes the point at which the celestial body is at its minimum distance from the primary gravitational focal point, while the apogee (Ap) corresponds to the maximum distance. The inertial reference system used in this work is the Earth-Centered Inertial (ECI) system, with the equatorial plane as the reference. In this system, the x-axis points towards vernal equinox Υ, the y-axis is orthogonal

to it within the equatorial plane, and the z-axis is perpendicular to the equatorial plane. Spacecraft motion is assumed to be prograde, following Earth's rotational direction.

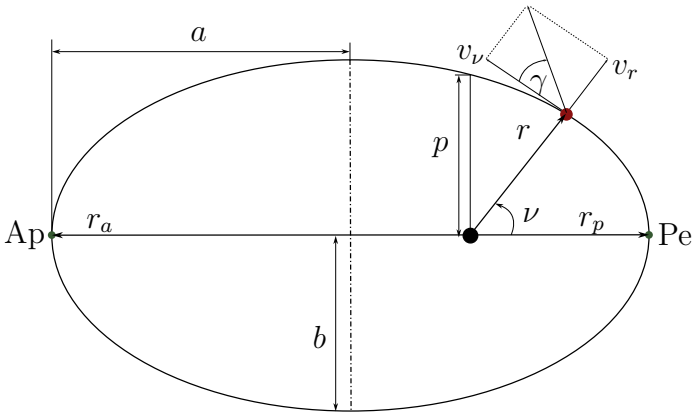

Figure 2.5.: Elliptical Orbit

To determine the trajectory of an object in space and its position along this path, six orbital parameters, as illustrated in figure 2.6, are required [56]:

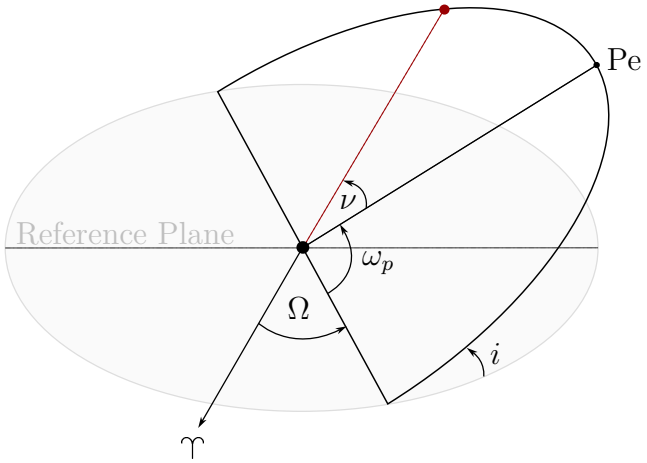

Figure 2.6.: Orbital Parameters

- Semi-major axis a, defining the orbit's size. It is computed for an elliptical orbit with the Earth's radius R_E, apogee height h_a, and perigee height h_p as:

$$a = \frac{2R_E + h_a + h_p}{2} \tag{2.1}$$

  Radius of apogee $r_a = a(1 + e)$ and radius of perigee $r_p = a(1 - e)$ are measured from the Earth's centre. For a circular orbit $a = r$ holds with $e = 0$.

- Numerical eccentricity e, defining the shape of the orbit.

- Inclination i, the tilt of the orbital plane relative to the Earth's equatorial plane.
- Right Ascension of the Ascending Node (RAAN) Ω describing the angle between the Vernal Equinox Υ and the point where the orbit crosses the equatorial plane from south to north.
- Argument of perigee ω_p, indicating the angular position of the perigee relative to the ascending node.
- True anomaly ν, indicating a satellite's position in its orbit relative to the perigee.

In conjunction with a, e defines the geometric properties of the conic section. i, Ω and ω_p define the orientation of the orbit in space relative to a fixed reference coordinate system. The period of an elliptic orbit with standard gravitational parameter μ representing the third law of Kepler is

$$P_e = 2\pi\sqrt{\frac{a^3}{\mu}} \tag{2.2}$$

Using elliptical geometry relations with semi-latus rectum p and semi-minor axis b, the parametric equation (2.6) is derived.

$$b = a\sqrt{1-e^2} \tag{2.3}$$

$$e = \sqrt{1-\left(\frac{b}{a}\right)^2} \tag{2.4}$$

$$p = a\left(1-e^2\right) \tag{2.5}$$

$$r = \frac{p}{1+e\cos\nu} = \frac{a\left(1-e^2\right)}{1+e\cos\nu} \tag{2.6}$$

Additional orbital characteristics encompass the different types of anomalies: Eccentric anomaly E and mean anomaly M, correlating true anomaly ν and time t to a reference time τ on elliptic orbits.

$$E = 2\arctan\left(\sqrt{\frac{1-e}{1+e}}\tan\left(\frac{\nu}{2}\right)\right) \tag{2.7}$$

$$M = E - e\sin E = \sqrt{\frac{\mu}{a^3}}\left(t-\tau\right) \tag{2.8}$$

The Vis-Viva equation 2.9 states that the specific energy c in an orbit is constant as a composition of kinetic energy c_{kin} and potential energy c_{pot}.

$$c = \frac{1}{2}v^2 - \frac{\mu}{r} = c_{kin} + c_{pot} = \text{const.} \tag{2.9}$$

With given constant for an elliptic orbit $c = -\frac{\mu}{2a}$ and its specific case of a circular orbit $c = -\frac{\mu}{2r}$, elliptic velocity v_e and circular velocity v_c are derived [56].

$$v_e = \sqrt{\frac{2\mu}{r} - \frac{\mu}{a}} \tag{2.10}$$

$$v_c = \sqrt{\frac{\mu}{r}} \tag{2.11}$$

The velocity is decomposed into its radial component v_r and tangential component v_ν, defined relative to the flight path angle γ as depicted in figure 2.5 with specific angular momentum $h = r \times v = r^2\dot{\nu} = \sqrt{\mu p}$.

$$v_r = \dot{r} = \frac{er^2 \sin\nu}{p}\dot{\nu} = \sqrt{\frac{\mu}{p}} e \sin\nu \tag{2.12}$$

$$v_\nu = r\dot{\nu} = \frac{\sqrt{\mu p}}{r} = \sqrt{\frac{\mu}{p}}\,(1 + e\cos\nu) \tag{2.13}$$

$$\gamma = \arctan\left(\frac{v_r}{v_\nu}\right) = \frac{e\sin\nu}{1 + e\cos\nu} \tag{2.14}$$

$$\tag{2.15}$$

The Earth's oblateness effect is a gravitational force of the planet's bulge, perturbing the idealized two-body problem. This results in the precession of RAAN and the advance of the argument of perigee [83].

$$\dot{\Omega} = -\frac{3\sqrt{\frac{\mu}{a^3}} J_2 R_E^2}{2a^2\left(1 - e^2\right)^2}\cos(i) \tag{2.16}$$

$$\dot{\omega_p} = \frac{\dot{\Omega}}{\cos(i)}\left[\frac{5}{2}\sin^2(i) - 2\right] \tag{2.17}$$

The design of orbital transfers is a trade-off between transfer duration and cost expressed in fuel expenditure Δv. Transfer orbits are required when initial and final orbit

do not intersect [65]. The propulsion type influences feasible orbital change manoeuvres, with chemical propulsion providing high thrust for impulsive instantaneous changes [65]. In-plane transfers are achieved through various methodologies as figure 2.7 points out. At intersection of an orbit 1 and 2, an single-impulse transfer manoeuvre is feasible. The required Δv amounts to the difference in velocity and flight path angle γ.

$$\Delta v = \sqrt{v_1^2 + v_2^2 - 2v_1 v_2 \cos(\gamma)} \tag{2.18}$$

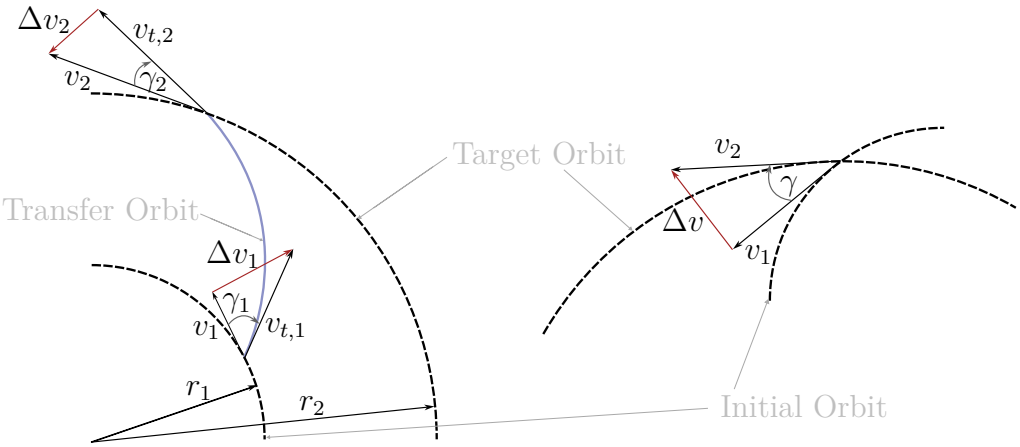

Figure 2.7.: General Single-Impulse (right) and Two-Impulse Transfers (left)

A general two-impulse transfer on a transfer orbit t requires a change in velocity direction indicated by flight path angles γ between velocities on initial orbit v_1 and final orbit v_2 in points of transfer and the according transfer velocities $v_{t,1}$ and $v_{t,2}$ [56].

$$\Delta v_1 = \sqrt{v_{t,1}^2 + v_1^2 - 2v_{t,1} v_1 \cos(\gamma_1)} \tag{2.19}$$

$$\Delta v_2 = \sqrt{v_{t,2}^2 + v_2^2 - 2v_{t,2} v_2 \cos(\gamma_2)} \tag{2.20}$$

$$\Delta v_{tot} = \Delta v_1 + \Delta v_2 \tag{2.21}$$

Minimizing Δv_{tot} for γ identifies the optimal transfer between circular coplanar orbits as occurring through a tangential impulse at a zero flight path angle, applied at either perigee or apogee [56]. This results in the classic elliptical trajectory of a Hohmann transfer illustrated in figure 2.8. The first impulse injects the spacecraft on the elliptic transfer orbit with $a_t = \dfrac{r_1 + r_2}{2}$ from the inner circular orbit applying Δv_1. Insertion in the higher circular orbit requires Δv_2.

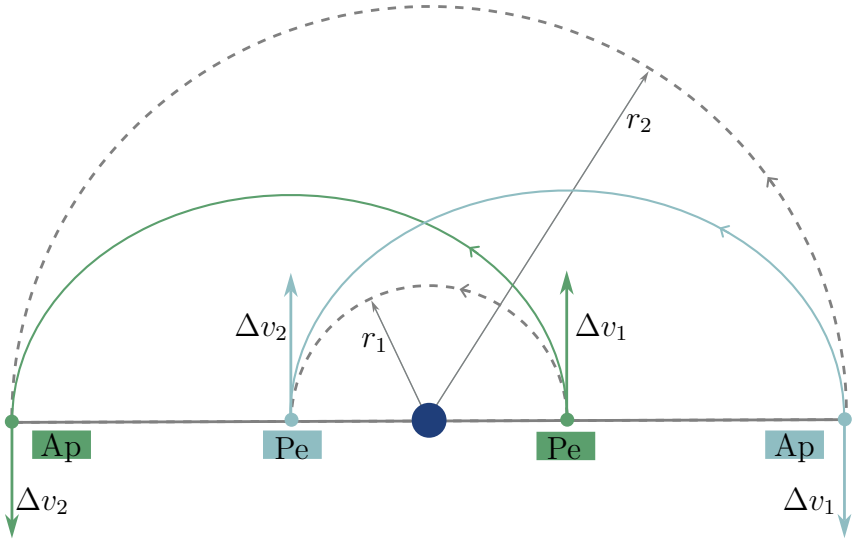

Figure 2.8.: Hohmann Transfer

$$\Delta v_1 = v_{e,p} - v_{c1} = \sqrt{\frac{2\mu}{r_1} - \frac{\mu}{a_t}} - \sqrt{\frac{\mu}{r_1}} \tag{2.22}$$

$$\Delta v_2 = v_{c2} - v_{e,a} - = \sqrt{\frac{\mu}{r_2}} - \sqrt{\frac{2\mu}{r_2} - \frac{\mu}{a_t}} \tag{2.23}$$

$$\Delta v_{tot} = \Delta v_1 + \Delta v_2 \tag{2.24}$$

To raise the orbit, thrusting at perigee where the speed is higher, is more energy-efficient which is explained by the Oberth effect stating proportionality of change in specific energy to orbital speed [66, 83]: $\Delta c_{kin} = \frac{1}{2}\Delta v^2 + v\Delta v$. For $r_2/r_1 < 11.93$, the two-impulse Hohmann transfer is always more efficient than a three-impulse bi-elliptic transfer, even through $r_3 \to \infty$. The Time of Flight (TOF) of a Hohmann transfer is

$$\mathrm{TOF}_{\mathrm{Hohmann}} = \frac{P_\mathrm{e}}{2} = \pi\sqrt{\frac{a_t^3}{\mu}} \tag{2.25}$$

To achieve rendezvous, the active spacecraft must not only transfer to the passive spacecraft's orbit but also match its true anomaly. Phasing adjusts the true anomaly ν by modifying the orbital period to synchronize the relative time difference between the initial and final orbits, applying thrust at the same point in the transfer orbit [21, 65]. This manoeuvre correlates with a Hohmann transfer to and from the same orbit [17]. To catch up with a target, the spacecraft moves to a lower orbit with a shorter period, while slowing down involves a higher phasing orbit with a larger semi-major axis. Du Sarton Jonchay et al. [20] formulate the phasing problem as follows: To eliminate

the initial relative angle ν_0, with $\alpha = 2\pi - \nu_0$, chaser ch and target tg must complete a respective number of orbits, k_{ch} and k_{tg}, before rendezvous. Dutta [21] identifies two phasing manoeuvres: Subsynchronous ($a_{ch} < a_{tg}$) and Supersynchronous ($a_{ch} > a_{tg}$) for $\alpha \geq np.pi$ or $\alpha < np.pi$ as shown in figure 3.7.

$$\mathrm{TOF}_{\mathrm{Phasing}} = k_{ch} P_{ch} = 2\pi k_{ch} \sqrt{\frac{a_{ch}^3}{\mu}} \tag{2.26}$$

$$\mathrm{TOF}_{\mathrm{Phasing}} = k_{tg} P_{tg} + \frac{\alpha}{2\pi} P_{tg} = \left(\alpha + 2\pi k_{tg}\right) \sqrt{\frac{a_{tg}^3}{\mu}} \tag{2.27}$$

Finding suitable pairs of k_{ch} and k_{tg} allows to determine the phasing orbit altitude a_{ch}. Constraining the transfer to a maximum time of flight, the boundary for k_{tg} is set.

$$a_{ch} = \left[\frac{\alpha + 2\pi k_{tg}}{2\pi k_{ch}}\right]^{2/3} a_{tg} \tag{2.28}$$

Change in RAAN Ω and inclination i require out-of plane manoeuvres as illustrated in figure 2.9 and cannot be handled by coplanar plane changes [65].

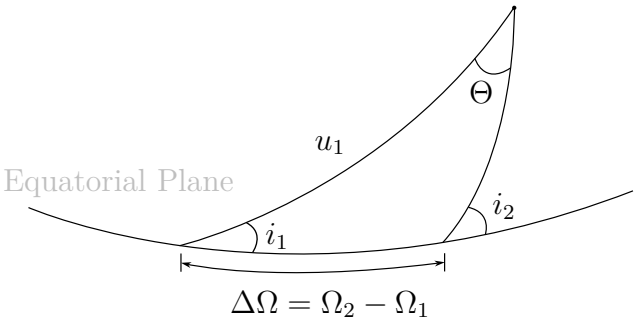

Figure 2.9.: Plane Change Triangle

Spherical trigonometry with angle of plane change Θ relates change in i and Ω at argument of latitude u_1 of the plane change. $u_1 = \omega_{p,1} + \nu_1$ is the arc measure from the ascending node which is the sum of argument of perigee and true anomaly of the initial orbit at time of thrust [66]. ν_1 thus determines the moment of thrust application (2.31) which can be calculated using (2.29) having determined Θ with (2.30).

$$\cos i_2 = \cos i_1 \cos \Theta - \sin i_1 \sin \Theta \cos u_1 \tag{2.29}$$

$$\cos \Theta = \cos i_1 \cos i_2 + \sin i_1 \sin i_2 \cos \left(\Omega_2 - \Omega_1\right) \tag{2.30}$$

$$\Delta v = 2v \sin\left(\frac{\Theta}{2}\right) \tag{2.31}$$

Simultaneous plane change Θ and size/type of orbit change requires [83]

$$\Delta v = \sqrt{v_1^2 + v_2^2 - 2v_1 v_2 \cos(\Theta)} \tag{2.32}$$

A pure change in inclination, without simultaneous change in RAAN, requires constraining the plane change manoeuvre to the equatorial crossing [15, 66]. The law of cosines (2.32) then simplifies for a pure inclination change Δi manoeuvre, where $v = v_1 = v_2$, to equation (2.33). An inclination change at lower speed is thus more efficient [66].

$$\Delta v = 2v \sin\left(\frac{\Delta i}{2}\right) \tag{2.33}$$

2.2.2. Spacecraft Design

The spacecrafts in this study include servicing spacecrafts, propellant depots, and client satellites with in-space propulsion systems, as well as launchers. The Tsiolkovsky equation (2.34) provides a mean to compute the available velocity increment Δv for a rocket, given the specific impulse I_{sp}, the gravitational constant g_0, initial vehicle mass m_0 and final vehicle mass m_f. This equation is essential for performance characteristics of propulsion systems and enables the analysis of mission profiles.

$$\Delta v = I_{sp} g_0 \ln\left(\frac{m_0}{m_f}\right) \tag{2.34}$$

The launch mass m_0 is comprised of three mass components: the structural mass m_s, the payload mass m_{pl}, and the propellant mass m_p. The structural coefficient ϵ_s, payload ratio Π_{pl}, and propellant ratio μ_p sum to unity.

$$m_0 = m_s + m_{pl} + m_p \tag{2.35}$$

$$m_f = m_s + m_{pl} \tag{2.36}$$

$$\epsilon_s + \Pi_{pl} + \mu_p = \frac{m_s}{m_0} + \frac{m_{pl}}{m_0} + \frac{m_p}{m_0} = 1 \tag{2.37}$$

Finally, to achieve Δv, the necessary propellant mass m_p can be determined using the mass relations (2.35) and (2.36) in conjunction with the rocket equation (2.34).

$$m_p = m_0\left(1 - e^{-\frac{\Delta v}{I_{sp} g_0}}\right) \tag{2.38}$$

The chosen launcher for the OOS infrastructure deployment is the European Ariane 6.4 launching in Kourou. The fairing volume constrains the payload volume in a cylinder of 4.57 m diameter and 11.185 m in height while the total fairing height is 18 m. GEO satellites are launched in GEO Transfer Orbit (GTO) with parameters as given in table 2.4 with reference to Kourou Meridian. The payload mass which represents the performance output of the selected launcher depends on insertion orbit parameters. [3]

Table 2.4.: Ariane 6.4 GTO Parameters [3]

h_p	250 km
h_a	10 000 − 80 000 km
i	6°
Ω	−120∘
ω_p	178°

The terminology in this work follows the orbital classes and corresponding parameters defined by the ESA Space Debris Office [24], as outlined in table A.1. Prime candidates for OOR are geosynchronous satellites. The number of objects in GEO nearly doubled between 2000 and 2022, reaching almost 1 000. Most satellites in GEO_{IADC} serve communication, with navigation, weather, imaging, and technology domains also contributing. Satellites in GEO are impacted by solar radiation pressure, gravitational perturbations, and atmospheric drag. The primary fuel demand for GEO station-keeping arises from countering latitude drift caused by third-body gravitational forces, particularly through north-south station-keeping [14]. At End-of-Life (EOL), satellites must clear the protected region by moving to higher altitudes, ensuring no re-entry within 100 years. As of 2022, only 55% of attempts succeeded, though clearance rates have averaged 80% since 2015 [24]. Telecommunications satellites typically have an operational lifespan of 15 years [12]. Statistically, a GEO satellite experiences early failure every 18 months, often due to propulsion or AOCS malfunctions [12]. Emergency needs for refuelling due to unforeseen events arise. For example, GEO satellites Orion 3 and the ChinaSat-9A [55] were placed in the wrong orbit consuming large amounts of propellant to manoeuvre to their final orbits. According to the Union of Concerned Scientists [91], there are 590 active GEO satellites, accounting for 7.8% of all satellites. Their lifetime is closely tied to fuel capacity for manoeuvres and station-keeping [90]. Kramer [49] cites a Northern Sky Research forecast predicting that 75 GEO satellites will require life extension by 2030, representing a market of $3.2b. GEO satellites are therefore chosen in this study as there is an apparent need for life prolongation, with a potential to make GEO environment more sustainable.

2.3. Space Logistics

Space logistics share similarities with terrestrial logistics, which initially informed orbital logistics research. On Earth, costs are linked to distance and time, whereas in space, they are governed by orbital mechanics, typically estimated through Δv and Time of Flight (TOF) or Δt. When depot and servicer positions are time-dependent, static cost mappings are not applicable. The deployment phase of infrastructure also has a significant impact on overall cost and duration [39]. The shift from centralized to decentralized and eventually distributed networks represents a major paradigm change in space systems architecture, complicating logistics scenarios further [72].

Logistic problems are modelled as networks or graphs, $G = (N, A)$, where N is a finite set of nodes $N = \{N_0, N_1, ..., N_n\}$ and A is a set of directed edges $A = \{(i,j) : N_i, N_j \in N, i \neq j\}$ connecting node pairs [51]. A path consists of a sequence of adjacent nodes or edges, with a length typically representing distances in Earth-based networks, or Δv or Δt in space logistics context.

2.3.1. Vehicle Routing Problem

The design of routes in such networks is addressed by routing problems [51]. The Vehicle Routing Problem (VRP) involves multiple vehicles servicing a set of clients across multiple routes, with the objective of minimizing an objective function, often representing the total length of feasible tours under constraints [51]. The mathematical formulation includes this objective function, decision variables, and constraints. When vehicle capacities are limited, the problem becomes the Capacitated Vehicle Routing Problem (CVRP). Gürtuna and Trépanier [35] formulate a space-based VRP, where a depot at node N_0 stations servicers required to visit clients located at nodes $N \setminus N_0$. This logistics problem is a single-depot CVRP that involves a fleet of m servicing vehicles, each with a maximum capacity of Q_i, along with a set of n client satellites. The servicing vehicles shall fulfil the non-negative demand of the clients D_i. The cost C_{ijk} for going from client i to client j is the Δv required for the orbit change with servicer k. $r(S) = \left\lceil \sum_{i \in S} D_i / Q \right\rceil$ assuming a constant vehicle capacity Q is the minimum number of vehicles needed to service the nodes in a subset of costumers S [36].

The objective function minimizes the total cost of all manoeuvres

$$\min \sum_{i=0}^{n} \sum_{j=0}^{n} \sum_{k=0}^{m} C_{ij} x_{ijk} \tag{2.39}$$

with decision variable

$$x_{ijk} = \begin{cases} 1 & \text{, if vehicle k travels from client i to j (client j visited right after client i)} \\ 0 & \text{, otherwise} \end{cases} \tag{2.40}$$

such that the following constraints are fulfilled: Every client is visited exactly once by exactly one vehicle. The servicers must visit a client, and then manoeuvre to visit another client. Each route starts and ends at the depot, ensuring the flow conservation equation at nodes is satisfied, as defined by equation (2.41). The Generalized Subtour Elimination Constraint (GSEC), represented by relation (2.43), ensures that the tour is complete and not divided into subtours [36]. Additionally, the total transported fuel within a vehicle on one route must not exceed the vehicle's capacity, a condition enforced by equation (2.42).

$$\sum_{i=0}^{n} x_{ihk} - \sum_{j=0}^{n} x_{hjk} = 0 \qquad \text{for} \quad h = 0, \ldots, n; \quad k = 1, \ldots, m \tag{2.41}$$

$$\sum_{i=0}^{n} \sum_{j=0}^{n} D_i x_{ijk} \leq Q_k \qquad \text{for} \quad k = 1, \ldots, m \tag{2.42}$$

$$\sum_{i \in S} \sum_{j \in S} x_{ij} \leq |S| - r(S) \qquad \forall S \subseteq N \setminus \{N_0\}, \quad S \neq \emptyset \tag{2.43}$$

2.3.2. Solution Schemes

The VRP to be solved is an NP-hard optimization problem for which heuristic approaches are weel suited when approximate solutions are sufficient. Exact solutions are only adapted to small networks [50]. The Clarke and Wright Savings algorithm, the most widely used method for efficiently solving the VRP, is further detailed in section A.1.3.

Genetic Algorithms (GA) as evolutionary algorithms are part of metaheuristic algorithms that are suitable to tackle NP-hard problems [96]. Population-based metaheuristics allow for diversity through multiple candidate solutions during the search process preventing trapping in local minima. A GA is based on the biologic evolution process employing chromosome representation for solution points. New generations are iteratively produced by biology-inspired operators applied to chromosomes. These include selection, mutation, and crossover. Chromosomes are selected based on their fitness value, assigned by the fitness function. Subsequent crossover varies subsequences between chromosomes creating off-springs whereas mutation randomly changes chromosome bits. [47]

The optimization algorithm follows the procedure in figure 2.10:

1. Random population initalization with individuals as a set of numerical values.
2. Fitness evaluation of each individual with the objective function.
3. Selection of the fittest individuals to determine the individuals participating in the reproduction process.
4. Crossover is applied to the selected individuals producing an offspring O.
5. Mutation is applied to offspring O generating a new offspring O' which is placed in a new population. It promotes genetic diversity.
6. The three reproduction operations selection, crossover and mutation are repeated on the current population until the new one is complete.
7. The process is terminated when a convergence criterion is met or when the maximum specified number of new generations is reached.

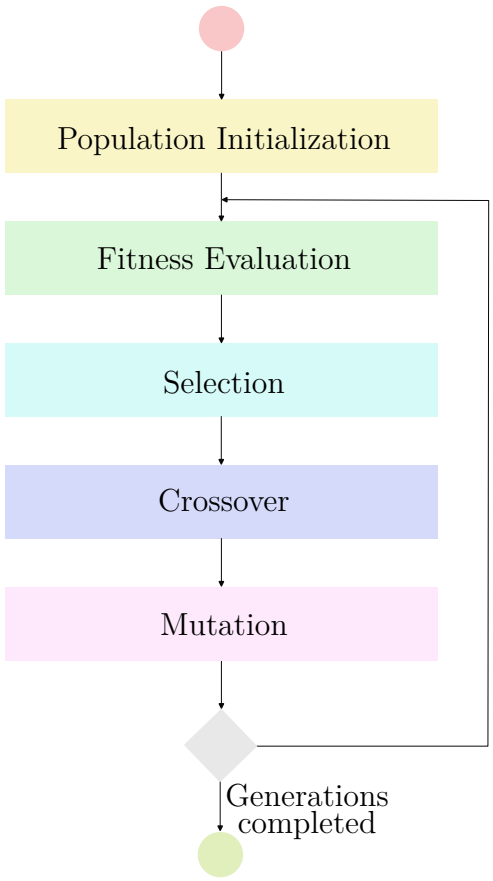

Figure 2.10.: Genetic Algorithm Flow

3. Model Development and Implementation

As highlighted, a need to develop a comprehensive methodology for OOR scenarios in GEO emerges. This methodology shall support system engineers in system of systems design by integrating mission priorities, constraints, variables and parameters within the design of OOR infrastructure. The methodology is developed for the scenario defined in chapter 3.1 followed by the derivation of trajectory design and logistics optimization in section 3.2. The chapter concludes with the implementation in section 3.3.

3.1. Refuelling Mission Scenario Description and Use Case Definition

The scenario for On-Orbit Refuelling of geosynchronous client satellites defines the mission sequence and interdependencies between its key components. It serves as a foundational framework, applicable to specific use cases. OOR is relevant for two potential refuelling mission scenarios:

- Nominal Refuelling Mission for planned operational lifetime extension. Fuel is supplied to satellite's orbit control system enabling it to maintain its GEO slot for an extended duration. The architecture is inherently optimized for this mission.
- Rapid Response Refuelling Mission for unplanned events such as propulsion leaks, payload misplacements, or emergency collision avoidance manoeuvres. The architecture's performance in handling such rapid response needs is also evaluated.

A M2M servicing architecture was selected to accommodate both mission types. Uncooperative refuelling is assumed as GEO satellites must stay within their orbital slots. The servicing architecture is placed in client altitude orbit, which has been shown to be the most efficient deployment mode for maximizing economic benefit and minimizing refuelling response time [55]. The scenario in figure 3.1 can be categorized as a MGSRP.

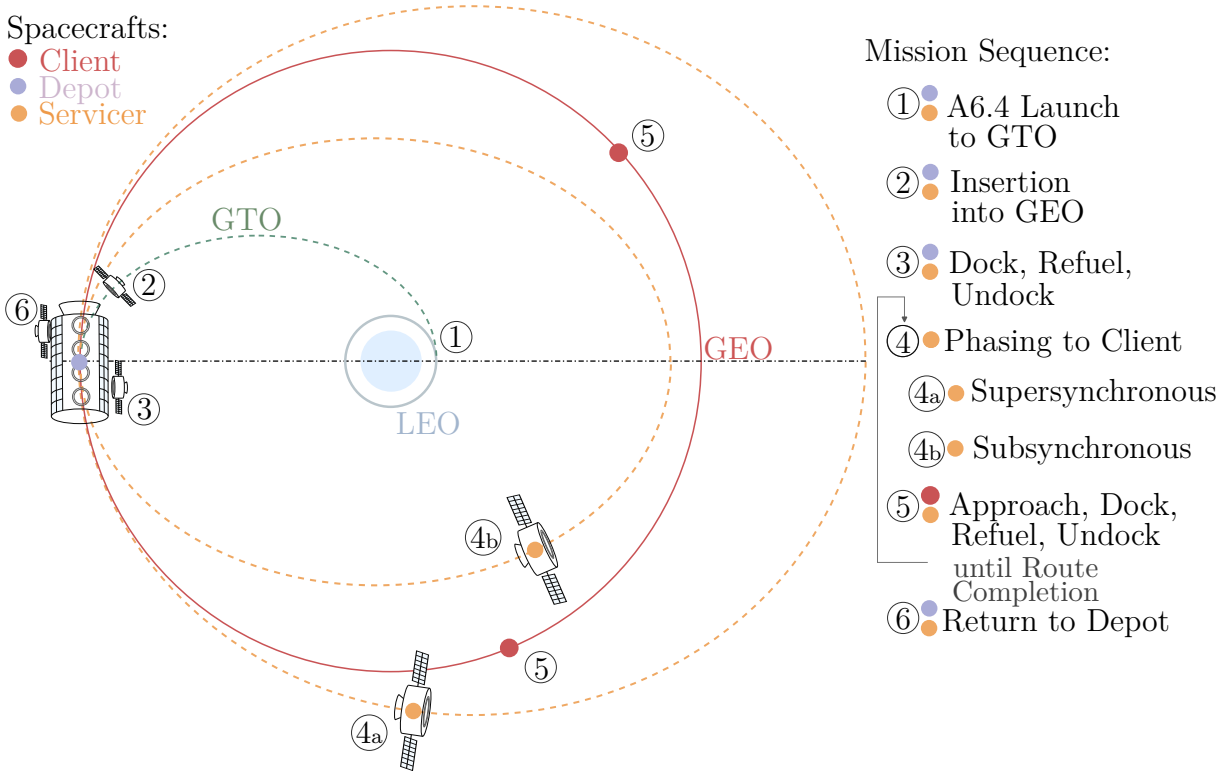

Figure 3.1.: GEO Refuelling Scenario

The infrastructure consists of servicing vehicles, also denoted servicers hereafter, which are responsible for refuelling client satellites. A single fuel depot enables reusability of the infrastructure. Figure 3.1 depicts the scenario of the OOR mission, providing a detailed breakdown of the individual mission sequences. All spacecraft, including the depot and servicers, are deployed into GTO by an Ariane 6.4 launch vehicle, with the orbit's apogee at GEO altitude ①. The number of launches required is contingent upon the specific servicing architecture design. Given that all GEO spacecraft are equipped with apogee engines [12], each vehicle within the scenario performs the second GTO burn for insertion using its own onboard propulsion systems ②. Upon insertion into the depot orbit, the servicers dock with the fuel depot, where they are refuelled by the depot ③. The available propellant mass is evenly distributed across all servicers to ensure balanced fuel allocation. After refuelling, the servicers undock from the depot simultaneously and each servicer proceeds along its designated route, defined within its individual mission plan, visiting client satellites sequentially ④. After completing their routes, the servicers return to the depot ⑥. Along their respective trajectories, they perform orbit changes with rendezvous ④a ④b, final approach, docking, refuelling, and undocking at each client satellite ⑤. The allocation and scheduling of the nominal operation poses the logistic optimization problem. To evaluate rapid response performance, an available refuelling vehicle suppos-

edly docked to the fuel depot, is assumed to directly transfer to the client with urgent fuel demand. In further operation, the fuel depot is refillable from Earth, allowing for another sequence of refuelling through the reusable servicers. This work only studies one cycle, but stays valid for further refuelling cycles to other potential sets of client satellites.

As the design of On-Orbit Servicing infrastructure and their performance are found to be highly dependent on the defined client constellation, the client selection should be relevant to a potential application case [78]. To draw conclusions about effective architecture configurations, this study finds a representative set of European client satellites as a use case for the On-Orbit Refuelling scenario. The 15 selected geosynchronous satellites in figure 3.2 and their modelling are further presented in section 3.1.2. The method can be directly applied to any other set of GEO client satellites by adjusting the client database.

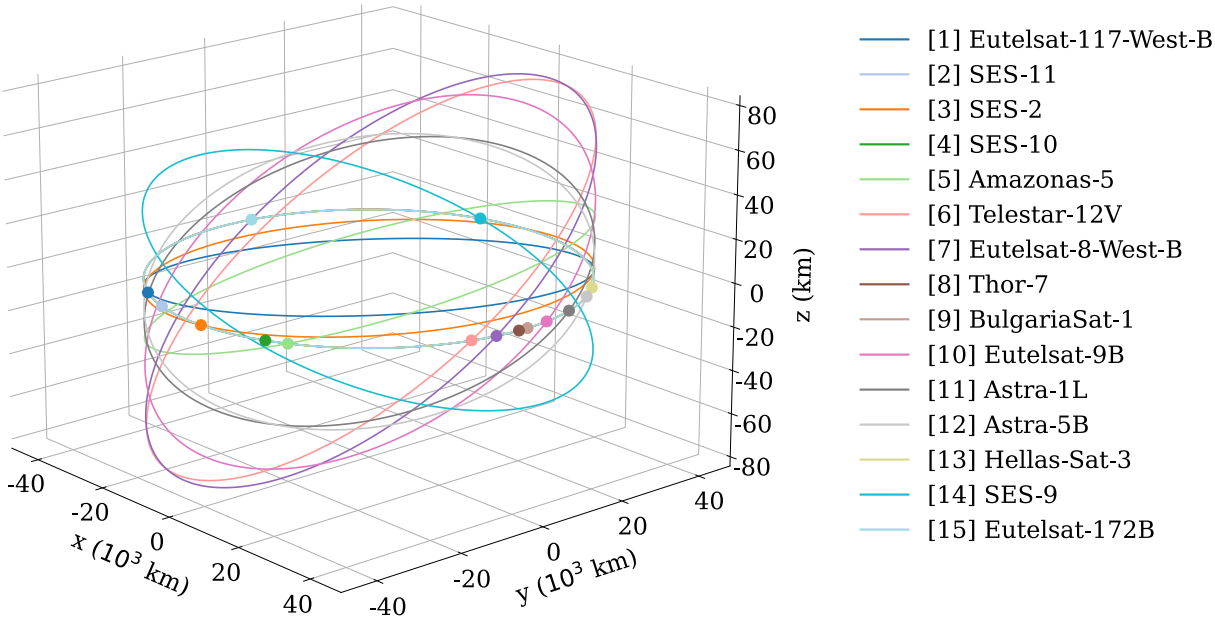

Figure 3.2.: Client Satellite Orbits in ECI Frame

3.1.1. Design Variables, Parameters and KPIs

In the process of OOR architecture design for the described use case and scenario, design variables are systematically varied, with each combination representing a unique system design point. The performance of each architectural configuration is assessed using Key Performance Indicators (KPIs). To ensure a well-defined problem space at acceptable complexity, parameter definitions are established and held constant.

Each OOR architecture is defined by two design variables: the fuel depot orbit and the number of servicers. Spacecraft are sized to allow for feasibility of each design point to assess the OOR's performance as a function of these variables.

- Fuel depot orbit: Both the depot and servicers are inserted into the operational orbit of the fuel depot. A discrete set of candidate depot locations is initially selected and refined in subsequent iterations for convergence. Given the variation in client RAAN, Ω is considered over the full range of $0 - 360°$. The fuel depot is assumed to be in a circular, geostationary orbit at GEO altitude with zero inclination. Although the methodology permits inclined depot orbits, geosynchronous orbits are less favourable due to the higher cost of out-of-plane manoeuvrers during refuelling. While inclined orbits may be worth exploring under reusability considerations, where the depot is refilled via Earth launches (Ariane insertion at 6° inclination into GTO), this extended mission scenario is not analysed in this study. To assure modelling as a stationary logistics problem, the moment the servicers depart from the depot, fixes the fuel depot location relative to the client satellites.

- Number of servicers: The minimum number of servicers, constrained in capacity, is determined by the total client demand. In the extreme case where one servicer refuels a single client, the O2O scenario, the maximum number of servicers considered equals the number of clients. In the defined use case, 4 to 15 servicers are studied.

The feasibility and performance of the refuelling mission are affected by fixed design parameters across the iterations of this study. However, the methodology remains flexible, allowing for modifications to these parameters, thereby facilitating informed system-level decisions in future concept evaluations. Table 3.1 outlines the primary scenario parameters, including a specified cost-duration trade-off preference $p_{\Delta v/\Delta t}$, along with constraints on both duration and cost for orbital transfers within the mission. $p_{\Delta v/\Delta t} = 0.0$ indicates a prioritisation of cost, while $p_{\Delta v/\Delta t} = 1.0$ reflects duration prioritisation. A value of $p_{\Delta v/\Delta t} = 0.1$ is chosen to maintain cost minimization as the primary objective, aligning with cost priority in Δv logistics optimization, while still encouraging more time-efficient solutions without significantly impacting overall cost. In the absence of real reference missions or openly available data, no predefined constraints or values are applied. The total mission duration is limited to a maximum of one month for the selected $p_{\Delta v/\Delta t}$, with phasing durations slightly shorter than full transfer durations. Additionally, the maximum cost is set sufficiently high to ensure it does not exclude any transfer options. Key parameters, including the spacecraft design of servicing vehicles and depots, are particularly significant and are represented as constants in figure 3.4. Additionally, the launcher

orbit in table 3.4 and client orbits in table 3.2 serve as input parameters to the scenario. Further scenario-specific parameters, such as those related to close proximity operations and refuelling, are provided in table 3.3. A comprehensive list of all parameters, along with their implementation, can be found in tables A.6 and A.7.

Table 3.1.: Scenario Parameters

Parameter	Value	Description
Demand Percentage	0.33	Client satellite demand level of the mission for lifetime extension by 10% to 100%
Cost vs. Duration $p_{\Delta v/\Delta t}$	0.1	Trade-off factor $\Delta v/\Delta t$ with $p_{\Delta v/\Delta t} = 0.0$ for cost priority and $p_{\Delta v/\Delta t} = 1.0$ for duration priority
Maximum Duration	12 d	Maximum duration for one orbit change
Maximum Cost	2000 m/s	Maximum Δv for one orbit change
$\mathrm{TOF}_{\mathrm{max}}$	10 d	Maximum time of flight for one phasing manoeuvre
Phasing Δa Search Factor	0.5	Maximum phasing altitude $\mathrm{a}_{\mathrm{max}}$ search factor

The mission objective is to minimize refuelling operation mission cost $\Delta \mathrm{v}_{\mathrm{OOR,tot}}$. The refuelling operation mission starts when the servicers depart on their individual routes to service all clients and concludes when the last servicer has returned to the depot. A trade-off exists between Δv and mission duration Δt, both of which are critical. The Key Performance Indicators (KPIs) include the objective $\Delta \mathrm{v}_{\mathrm{OOR,tot}}$ and total mission cost additionally taking into account architecture deployment $\Delta \mathrm{v}_{\mathrm{tot}}$. The overall mission duration, from GTO to GEO insertion at deployment after which the spacecrafts become active, to depot return after servicing operations, $\Delta \mathrm{t}_{\mathrm{tot}}$, as well as the refuelling operation duration only $\Delta \mathrm{t}_{\mathrm{OOR,tot}}$, are evaluated. The rapid refuelling duration $\Delta \mathrm{t}_{\mathrm{OOR,rapid}}$ measures the time required for the longest single round trip to a client from the depot. It represents the performance in a rapid refuelling scenario, while remaining within the cost-duration preferences. The residual fuel mass $\Delta \mathrm{m}_{\mathrm{res}}$ determines mission feasibility. Although the use case ensures feasibility across all design points, residual fuel mass indicates potential downsizing or inefficiencies in refuelling routes.

3.1.2. Client Definition and Spacecraft Sizing

The refuelling scenario and use case formulation necessitate the selection and detailed modelling of client satellites, accompanied by the precise sizing and modelling of servicing spacecraft, to ensure coherent system configurations. This study examines refuelling of commercial client satellites operated by European entities. Telecommunication industry

shows the prime interest in GEO life extension. Only chemical propulsion clients are considered in this analysis. All 18 satellites from the database [91] fulfilling the specified criteria with EOL after 15 years between 2029 and 2032, are listed in table A.3. 15 satellites are selected for servicing in a single mission, excluding those with similar Ω. Tables 3.2 and A.4 detail their nearly circular orbits, with Ω ranging from $-117°$ to $172°$ and inclinations of $0°$ to $0.1°$. Figure 3.3 depicts the clients in equatorial plane. The fuel demand is based on a lifetime extension factor relative to the fuel capacity of the clients. For satellites lacking publicly available propellant or dry mass data, the total propellant mass is estimated using an average ratio of $m_p/m_0 = 0.544$, highlighted grey in table 3.2. The initial fuel mass in GEO m_p is calculated by deducting the insertion propellant for $\Delta v = 1\,500\,\mathrm{m/s}$ as derived in chapter 3.2.3 using an engine with $I_{sp} = 320\,\mathrm{s}$, representing typical apogee motor efficiency [2]. The client satellite demand is quantified for a percentage of lifetime extension, aiming for a five-year extension, equating to a 33% increase. Longer extensions may be impractical due to potential subsystem failures and advancements in technology necessitating satellite replacement. Propellant demand m_d is thus estimated to be between 200 and 400 kg, consistent with the MEP's planned delivery of up to 400 kg, confirming the relevance of the demand estimates. The total propellant demand amounts to 3.69 t. To determine the propellant level post-refuelling, the initial propellant mass at refuelling is calculated using a linear decrease model from the initial GEO mass to zero mass at EOL, ensuring a conservative approach.

Table 3.2.: Selected European GEO Client Satellites for Refuelling Scenario

ID	Satellite	Ω [°]	e	i [°]	m_0 [kg]	m_p [kg]	$\frac{m_p}{m_0}$	m_d [kg]	EOL
01	Eutelsat 117 West B	−116.8	1.90e−4	0.02	5 500	3 200	0.582	367	2030
02	SES-11	−105.0	1.90e−4	0.00	5 200	2 829	0.544	282	2032
03	SES-2	−87.0	2.37e−4	0.01	3 200	1 755	0.548	178	2029
04	SES-10	−67.0	2.61e−4	0.00	5 271	2 463	0.467	152	2032
05	Amazonas-5	−61.0	4.74e−5	0.04	5 900	3 429	0.581	392	2032
06	Telestar 12V	−15.0	9.75e−5	0.10	4 900	2 666	0.544	266	2030
07	Eutelsat 8 West B	−8.0	4.86e−4	0.10	5 800	3 155	0.544	314	2030
08	Thor-7	−1.0	1.66e−4	0.00	4 600	2 800	0.609	347	2030
09	BulgariaSat-1	1.9	2.73e−4	0.00	3 669	1 995	0.544	198	2032
10	Eutelsat 9B	9.0	1.42e−4	0.08	5 200	2 829	0.544	282	2031
11	Astra 1L	19.3	3.08e−4	0.05	4 500	2 247	0.499	177	2032
12	Astra 5B	31.6	7.12e−5	0.05	5 724	3 114	0.544	310	2029
13	Hellas-Sat 3	39.0	1.22e−3	0.00	5 780	3 280	0.567	358	2032
14	SES-9	108.0	1.90e−4	0.05	5 271	2 436	0.462	143	2031
15	Eutelsat 172B	172.0	5.22e−4	0.00	3 600	1 958	0.544	195	2032
				Total	**81 985**	**42 997**	**0.544**	**3 960**	

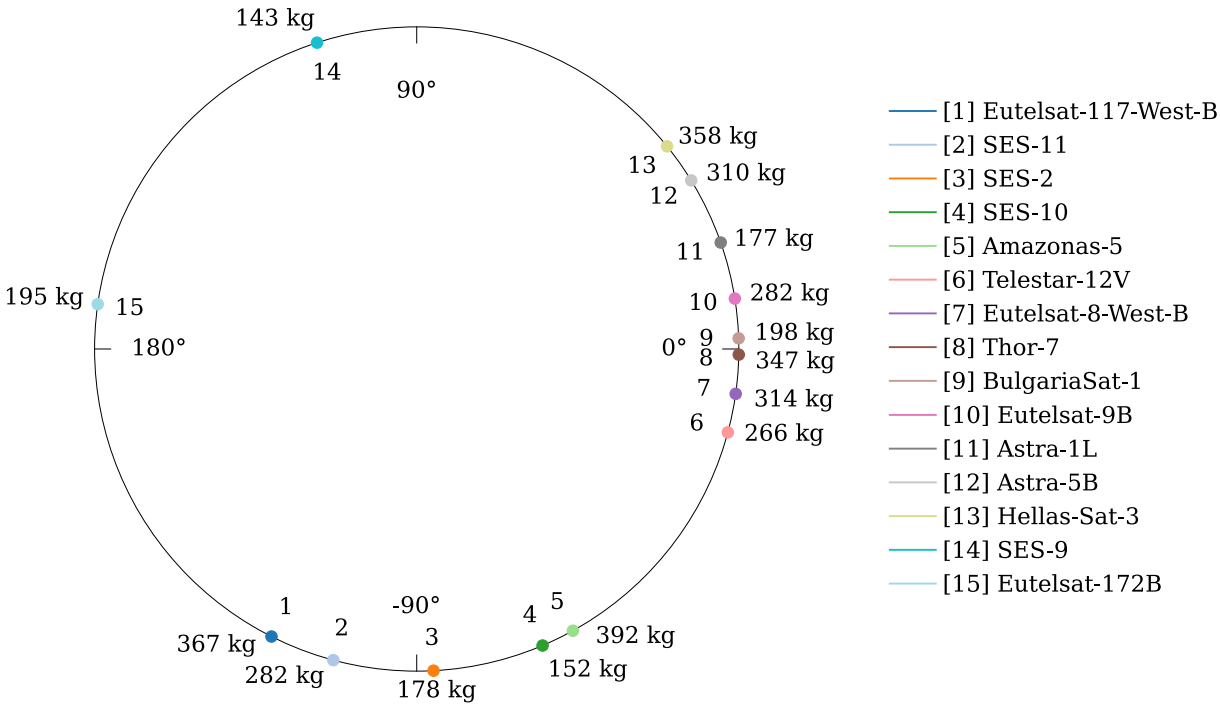

Figure 3.3.: Client Orbits in Equatorial Plane with Fuel Demand

Servicing spacecraft and propellant depot sizing for refuelling operations in this study are based on industry perspectives presented in table A.2 and existing concepts for planned missions to ensure relevance to realistic OOR missions. The sizing must allow feasibility of all design points within the defined mission sequence. In the planning of an actual refuelling mission, the number of servicers is predetermined, and their capacity and mass configuration are optimized to avoid excess mass. For the deployment of the OOR architecture, multiple servicers are launched into the same orbit. To maximize launcher efficiency, it is advisable to fully utilize the available launcher capacity. Therefore, herein, the number of vehicles per launch defines their individual launch mass. Ariane 6.4's performance to the target orbit is 11.09 t. Insertion into geostationary orbit at GTO apogee through a single thrust manoeuvre for circularization and out-of-plane change requires 1 491 m/s. Given the current spacecraft mass corresponding to its initial mass, the required propellant for GEO insertion can be computed with equation (2.38). The required propellant ratio for insertion Δv is $\mu_p \approx 38\%$. Market success is anticipated for refuelling large satellites ($\geq 2.55\,\mathrm{t}$) using depots and spacecraft of $\geq 1\,\mathrm{t}$ [8]. The selected use case corresponds to this anticipated vision and analysis. All spacecrafts considered in this study operate with chemical propulsion systems. Propellant reserved for refuelling purposes is denoted as payload propellant, while propulsion propellant is reserved for in-space manoeuvres. The maximum payload propellant mass represents the spacecraft's

capacity. Additionally, since reusability via Earth-based refilling is assumed, no propellant allocation for EOL manoeuvres is considered in the spacecraft sizing process. Graphic 3.4 depicts the final spacecraft parameters with complete spacecraft related data in table A.5.

With three spacecraft launched simultaneously, the wet mass m_0 of each servicer is 3 500 kg, allowing for launcher adapter margins. Assuming a structural coefficient $\epsilon_s = 30\%$, the resulting dry mass m_s is 1 050 kg. Launch insertion alone requires 1 323 kg of propellant. The total propellant demand for client satellites life extension amounts to 3.96 t. Servicer payload capacity is matched to this demand while allowing flexibility for uncertainties and route optimization. Although a servicer capacity of 1 000 kg is technically sufficient for refuelling with a minimum of four servicer, logistical optimization remains highly constrained. Therefore, a slightly higher capacity $m_{pl} = 1\,100$ kg is selected to improve solution robustness. The other extreme case of O2O refuelling is dimensioning for minimum propellant mass, with the available propellant for OOR manoeuvres relying on the depot's initial supply. This supply is equally divided among servicers, so as the number of servicers increases, the fuel allocated to each decreases proportionally. Preliminary simulation results of the O2O case show sufficiency of $m_p = 1\,350$ kg leaving slight margins. The order of magnitude aligns with the ISTV concept from ArianeGroup, which serves as reference for propulsion system and volume. The engine developed for the Ariane kick-stage ASTRIS is the BERTA bi-propellant thruster, delivering payloads of up to 3 t to GEO with a thrust of 5 kN [95]. Since the I_{sp} value is not published, it is assumed to match existing ArianeGroup bi-propellant engines with $I_{sp} \approx 320$ s [2]. The total dimensions of ASTRIS are 1.8 m in height and 4.5 m in diameter.

The fuel depot with $m_0 = 11$ t is launched into its orbit in one A6.4 launch to GTO. In contrast to the servicers, only insertion burn and station-keeping are performed, as the depot stays in its orbital slot. GEO insertion requires 4 170 kg of propellant, and assuming the structural coefficient $\epsilon = 30\%$, the dry mass m_s is 3 300 kg. Station-keeping in a geosynchronous orbit is predominated by North-South control manoeuvres requiring 45 m/s yearly [97]. Assuming a need for station-keeping over the four-year period before depot refilling, which aligns with the client satellites' EOL timeline, a total of 400 kg of fuel is reserved for this purpose. Finally, 3 100 kg remain for propellant payload capacity m_{pl}. Once in orbit, the tank capacity previously used for insertion propellant becomes available for payload propellant through refuelling from Earth, enabling multiple refuelling missions. Although this scenario is not simulated, it would allow for a payload capacity of 7.3 t. The ArianeGroup bi-propellant 400NBI thruster, designed for apogee orbit injection

into GEO, delivers a thrust of 425 N, weighs 4.3 kg, and has a specific impulse of 321 s [2]. Comparing to the propulsion system of the 10.5 t Nyx capsule, which also performs GEO insertion, a combination of ten apogee thrusters is used for the depot propulsion system.

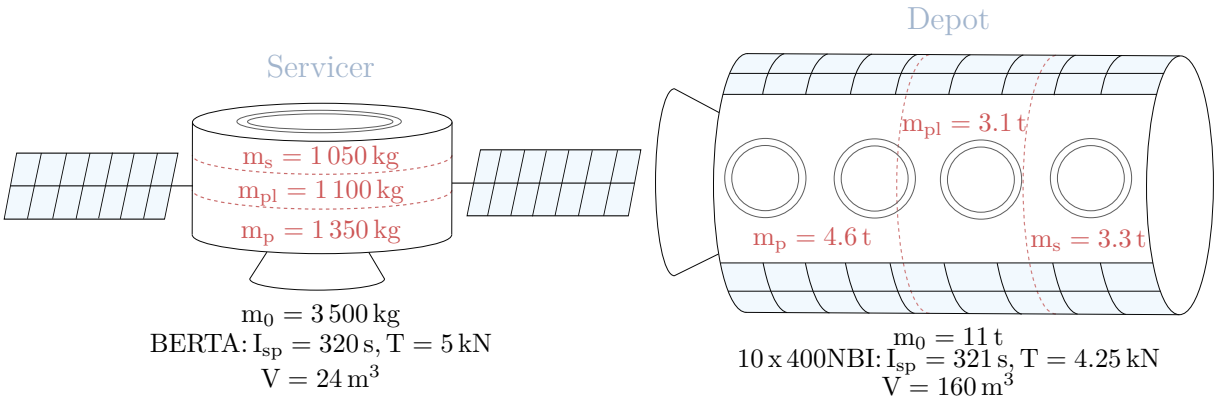

Figure 3.4.: Configuration of Refuelling Servicer and Fuel Depot

3.1.3. Assumptions and Simplifications

Several assumptions and simplifications reduce the complexity of the orbital mechanics model for streamlining the analysis with focus on mission design variables, while preserving the validity of the findings.

- Orbital mechanics are modelled by two-body physics omitting gravitational influence of other celestial bodies than Earth. Zhao et al. [101] demonstrate that Earth's triaxiality and Lunisolar effects only influence logistics optimization in long-duration transfers of more than 100 days. The simplification avoids the formulation of the problem as a three-body problem. The effect of Earth's oblateness is disregarded, as J2 perturbations similarly impact all client target orbits with equivalent GEO altitude and small inclinations. As a result, changes in RAAN and argument of perigee remain minimal, not significantly affecting the stationary assumption. Other potential perturbations, such as solar pressure, are considered negligible.

- All client orbits are assumed to be perfectly circular ($e = 0$) at geostationary altitude, with inclinations taken into account. The geostationary orbit has an orbital period of 23 hours 56 minutes and 4 seconds, corresponding to $P_{\mathrm{GEO}} = 86\,164\,\mathrm{s}$. The semi-major axis of this orbit, calculated using the equation (2.2), is $a_{\mathrm{GEO}} = r_{\mathrm{GEO}} = \sqrt[3]{\mu P_{\mathrm{GEO}}^2/(4\pi^2)} = 42\,164\,\mathrm{km}$, where $\mu = 398\,600\,\mathrm{km}^3/\mathrm{s}^2$. This results in an orbital altitude of 35 786 km, considering Earth's radius of $R_E = 6\,378\,\mathrm{km}$.

- Given the lack of data and the near-circular orbits, an argument of perigee of zero is assumed for all target satellites as a reference for true anomaly.

- Depot orbits are selected from a discrete set of geostationary orbits, refined in subsequent designs for convergence, but not treated as a continuous variable.

- Near-range manoeuvres, including Rendezvous, Proximity Operations, and Docking (PROD), are excluded from logistics optimization but are simulated according to standard operational phases of approach and docking. The rendezvous phase synchronizes orbits and phasing between vehicles, after which PROD is initiated. Constant values for propellant consumption and duration during final approach, docking, and undocking, derived from industry insights and typical operational ranges, are detailed in table 3.3. As the refuelling design interface, the RAFTI refuelling transfer rate is utilized to calculate the duration of the refuelling process based on the amount of propellant to be transferred.

Table 3.3.: PROD Parameters

Parameter	Value	Description
Propellant Transfer Rate	0.505 kg/s	RAFTI hydrazine transfer rate
Docking Duration	1 h	Docking/Undocking duration
Approach Duration	12 h	Proximity manoeuvres duration
Approach Mass	20 kg	Proximity manoeuvres mass consumption

Accurate scenario and use case definitions are crucial for resolving the logistics problem and detailing the mission sequence with precision.

- The logistics problem is formulated as a stationary problem, as the depot and clients exhibit no relative movement in the equatorial plane.

- Client satellites are refuelled based on estimated propellant needs rather than actual data, assuming nominal fuel depletion with a linear decrease from mission start to EOL. Refuelling need is limited to a fixed percentage of the initial propellant mass.

- Technical challenges and technological readiness levels are not evaluated, as they fall outside the scope of this study.

- All servicing spacecraft are standardized in mass configuration, with identical structural mass, refuelling payload capacity, and available propellant. The simulation is

executed using a fixed servicer and depot design, with any changes to design parameters reflected through modifications in the input data.

- At docking with client satellites, the servicers transfer the demanded amount of fuel from its payload propellant tank only.

- In the absence of specific data on the propellant used by client satellites, it is assumed that all clients use the same type of propellant. Alternatively, if the target satellites and servicing routes are known before mission launch, the servicers and depot can be stocked with the appropriate fuel types and quantities.

- The servicing vehicles are launched with their full propellant mass and refuel at the depot before beginning refuelling operations, with the depot's available propellant equally distributed among the servicers.

- Each client satellite is serviced only once, with each servicer completing a single round-trip for refuelling during one nominal mission operation cycle. All servicers depart from and return to the depot to complete their routes.

- At least one servicer is assumed to be available for rapid response performance calculations. Since the nominal refuelling mission lasts one month and the response time depends solely on the depot's orbit, this assumption is considered reasonable.

- Launcher performance for varying insertion orbits through GTO is calculated by interpolation from available Ariane 6.4 data based on input orbit specifications [7]. With Kourou longitude at $-53°$, the actual RAAN is $-173°$. Since GEO is circular and no rendezvous is required at insertion, $\omega_p = 0°$ without loss of generality. To compute Ω at intersection between GTO and GEO, considering the actual ω_p, angular relations yield $\Omega = -171°$. Table 3.4 gives the resulting orbital parameters.

Table 3.4.: A6.4 Launcher Insertion Parameters

h_p	250 km
h_a	35 786 km
i	$6°$
Ω	$-171°$
ω_p	$0°$

3.2. Design Methodology

The design flow and its implementation, as outlined in section 3.2.1, address two key areas necessitating methodological advancements: trajectory definition and logistics optimization. Section 3.2.2 systematically derives manoeuvres for the successive modification of all orbital parameters, resulting in the trajectory definition and selection methodology in section 3.2.3. The optimization of space logistics, which relies on the trajectory results, is elaborated in section 3.2.4.

3.2.1. Analysis Structure and Flow

The methodology in this study is structured into two levels. The first level focuses on the logistics optimization of the scenario, incorporating all given input parameters and constraints. The second step involves the execution/simulation of the mission, which utilizes the optimization output to define the individual spacecraft plans, from which the KPIs are derived. The implemented design process is depicted in figure 3.5. The top section, flowing from left to right, represents the first step, while the bottom section, flowing from right to left, corresponds to the second step. The figure includes graphical representations of the methods and results for each component, with references in brackets, providing context for the developments and findings presented. The overall design philosophy, providing broader context for this work, is illustrated in figure A.2. The figure highlights the various modules in the OOR mission design and their interconnections.

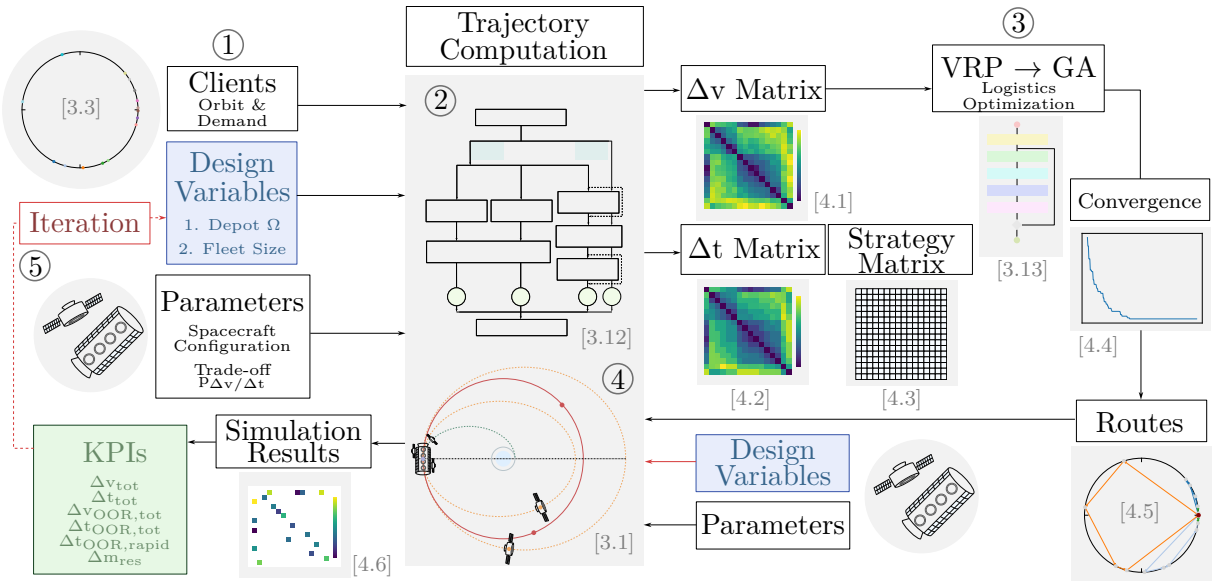

Figure 3.5.: Implementation Flow

Each combination of design variables represents a specific refuelling architecture, which undergoes the full process of mission definition, logistics optimization, and subsequent mission simulation. The design variables are iterated in two stages ⑤: an outer loop over discrete depot orbits and an inner loop over the number of servicers, ranging from the minimum to the O2O scenario. This process is refined by narrowing the depot orbit range with smaller step sizes, repeating until depot location convergence is achieved.

For each design point ①, consisting of fleet size, depot orbit, as well as the predefined parameters such as client and launcher orbits and states, the mission profile in terms of trajectory is computed. The selection of the trajectory is the first focus of this work. Under constraints and preferences for duration and cost, the optimal trajectory, composed of individual manoeuvres, is selected ②. The output includes a Δv matrix along with corresponding matrices for duration and strategy information, representing every possible transfer between all nodes in the mission. The cost matrix Δv serves as input for the logistics optimization. Solving the VRP using a GA forms the second key focus of this work ③. After the algorithm converges, the routes, including client allocation and scheduling for each spacecraft, are determined. With the input data and the now defined routes, mission procedures for each spacecraft can be defined and executed ④. This constitutes the scenario simulation within the TCAT tool, where all required mission phases including amongst others orbital transfers and refuelling, are calculated and executed by modifying the spacecrafts and their properties. The result is a complete set of performance parameters which is complemented by detailed mission plans.

3.2.2. Transfer Manoeuvres for Trajectory Design

The trajectory design is based on the computation of a sequence of orbital transfer manoeuvres required to alter specific orbital parameters from an initial orbit denoted with index 1 to a final orbit denoted with index 2. The scenario under consideration necessitates both in-plane and out-of-plane orbital adjustments. In the process of trajectory optimization, there exists a trade-off between minimizing time Δt and cost Δv. These competing objectives necessitate a compromise, represented by parameter $p_{\Delta v/\Delta t}$, to meet mission requirements effectively in both dimensions.

For a single-impulse transfer to be feasible, an intersection point between the two orbits must exist. Specifically, the radii of the two orbits must coincide, necessitating the solution of $\vec{r}_{ECI,1}(\nu_1) = \vec{r}_{ECI,2}(\nu_2)$ for the true anomalies ν_1 and ν_2 in ECI frame.

$$R_x(\eta) = \begin{pmatrix} 1 & 0 & 0 \\ 0 & \cos\eta & -\sin\eta \\ 0 & \sin\eta & \cos\eta \end{pmatrix} \qquad R_z(\eta) = \begin{pmatrix} \cos\eta & -\sin\eta & 0 \\ \sin\eta & \cos\eta & 0 \\ 0 & 0 & 1 \end{pmatrix} \tag{3.1}$$

Transformation of orbital parameters to ECI requires subsequent transformation in perifocal frame. The perifocal frame has Earth at the origin, where the x-axis points towards periapsis and the y-axis is orthogonal to the x-axis within the orbital plane. Transformation of r as given in equation (2.6) from trajectory orbital parameters is performed by projection on perifocal frame axes. For transformation of velocity components according to equations (2.12) and (2.13), rotation of ν around z-axis $R_z(\nu)$ is required.

$$\vec{r}_{\text{perifocal}}(\nu) = r \begin{pmatrix} \cos\nu \\ \sin\nu \\ 0 \end{pmatrix} = \frac{p}{1 + e\cos\nu} \begin{pmatrix} \cos\nu \\ \sin\nu \\ 0 \end{pmatrix} \tag{3.2}$$

$$\vec{v}_{\text{perifocal}}(\nu) = \begin{pmatrix} \cos\nu & -\sin\nu & 0 \\ \sin\nu & \cos\nu & 0 \\ 0 & 0 & 1 \end{pmatrix} \begin{pmatrix} \dot{r} \\ r\dot{\nu} \\ 0 \end{pmatrix} = \begin{pmatrix} \dot{r}\cos\nu - r\dot{\nu}\sin\nu \\ \dot{r}\sin\nu + r\dot{\nu}\cos\nu \\ 0 \end{pmatrix} = \begin{pmatrix} -\sqrt{\frac{\mu}{p}}\sin\nu \\ \sqrt{\frac{\mu}{p}}(e + \cos\nu) \\ 0 \end{pmatrix} \tag{3.3}$$

To define $\vec{r}$ and $\vec{v}$ in ECI, rotation matrices are applied to perifocal vectors according to the definition of orbital parameters: Rotation of ω_p around z-axis $R_z(\omega_p)$, rotation around x-axis by i $R_x(i)$, and finally rotation around z-axis by Ω $R_z(\Omega)$.

$$\vec{r}_{\text{ECI}} = R_z(\Omega)R_x(i)R_z(\omega_p)\vec{r}_{\text{perifocal}} \tag{3.4}$$

$$\vec{v}_{\text{ECI}} = R_z(\Omega)R_x(i)R_z(\omega_p)\vec{v}_{\text{perifocal}} \tag{3.5}$$

The system of three equations (3.6) is solved for ν_1 and ν_2. In a coplanar change, only the first two equations are non-zero. The objective function to be minimized (3.6) represents the distance between two points at ν_1 in initial orbit and ν_2 in final orbit. The quasi-Newton method is employed to solve the problem.

$$0 = \vec{r}_{ECI,1}\left(a_1, e_1, i_1, \Omega_1, \omega_{p,1}, \nu_1\right) - \vec{r}_{ECI,2}\left(a_2, e_2, i_2, \Omega_2, \omega_{p,2}, \nu_2\right) \tag{3.6}$$

Then, with known orbital parameters ν_1 and ν_2 at intersection, velocities in intersection

point can be calculated according to equation (3.5). The required impulse of a general single-impulse manoeuvre to simultaneously change all orbital parameters at once and instantaneously ($\Delta t = 0$) is:

$$\Delta v = \| \vec{v}_{ECI,2}\left(\nu_2\right) - \vec{v}_{ECI,1}\left(\nu_1\right) \| \tag{3.7}$$

Depending on start and target orbit properties and relations, the most energy efficient transfer might not be the single thrust strategy [56]. Two-impulse transfers are detailed in the following. Three-impulse manoeuvres, such as bi-elliptic transfers, are disregarded due to the short distances involved.

In-plane Change of Δa and Δe

Coplanar manoeuvres alter geometric properties of the conic section to modify orbit size and shape. The Hohmann transfer is the most efficient two-impulse manoeuvre. In the general case of transferring from an initial elliptical orbit 1 to a target elliptical orbit 2 via a transfer ellipse t, various transfer scenarios are possible, allowing simultaneous changes in the semi-major axis a and eccentricity e by adjusting the radii of apogee and perigee. The most cost efficient strategies have been derived and implemented in this work, as detailed in appendix A.2.2 and are displayed in figure 3.6. Equation (3.10) is the total cost of the Hohmann transfer between elliptic orbits with a first impulse at r_1 (3.8) on the initial orbit at apogee or perigee and a second impulse at r_2 (3.9) on the target orbit. The transfer orbit depends on the selected transfer strategy following $a_t = (r_1 + r_2)/2$.

$$\Delta v_1 = \left| v_t\left(r_1\right) - v_1\left(r_1\right) \right| = \left| \sqrt{\frac{2\mu}{r_1} - \frac{\mu}{a_t}} - \sqrt{\frac{2\mu}{r_1} - \frac{\mu}{a_1}} \right| \tag{3.8}$$

$$\Delta v_2 = \left| v_2\left(r_2\right) - v_t\left(r_2\right) \right| = \left| \sqrt{\frac{2\mu}{r_2} - \frac{\mu}{a_2}} - \sqrt{\frac{2\mu}{r_2} - \frac{\mu}{a_t}} \right| \tag{3.9}$$

$$\Delta v_{\text{tot}} = \Delta v_1 + \Delta v_2 \tag{3.10}$$

In case of two orbits intersecting on either apogee or perigee, a single impulse manoeuvre on the apsidal line is feasible and the required tangential velocity change simply equals

$$\Delta v = v_2\left(r_{a/p,2}\right) - v_1\left(r_{a/p,1}\right) \tag{3.11}$$

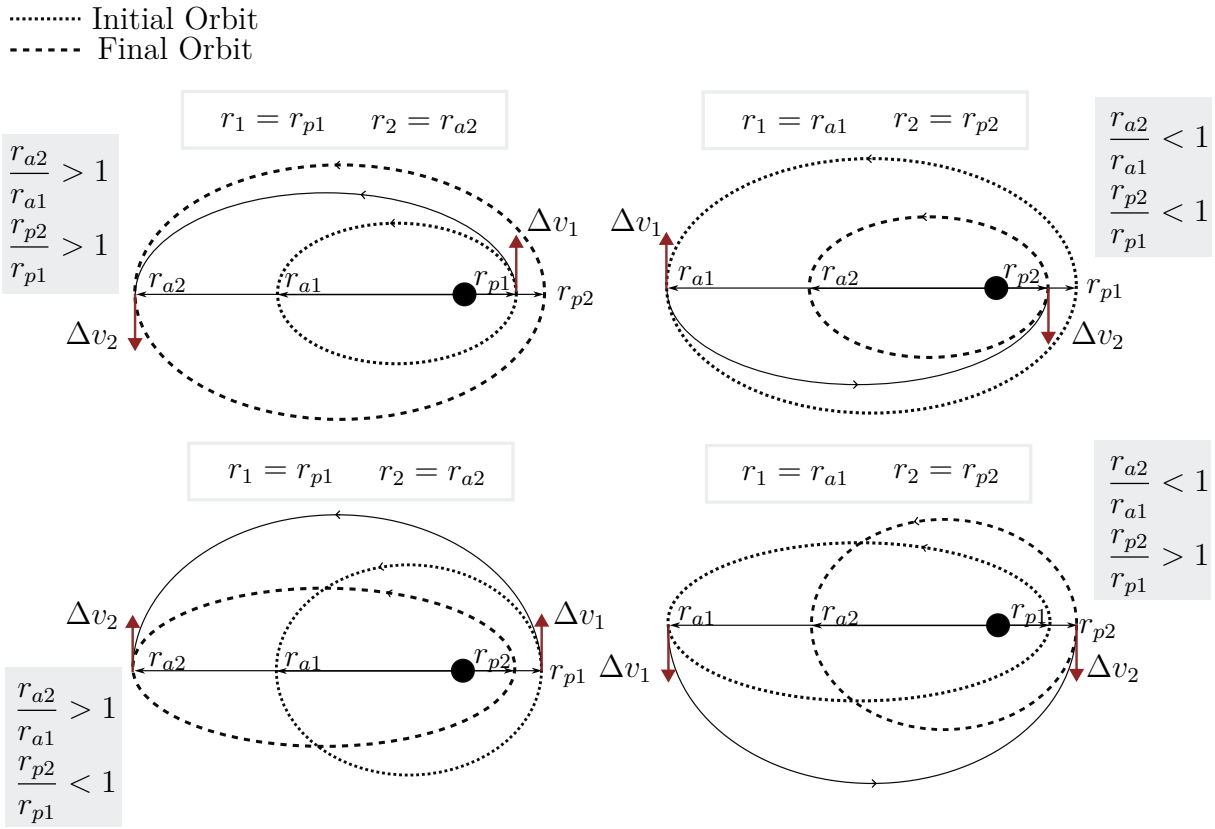

Figure 3.6.: Hohmann Strategies for Δv Optimal Manoeuvres between Elliptic Orbits

The transfer time depends only on the transfer orbit's a_t following equation (2.25) and is therefore strategy-dependent for elliptical orbits. The strategies for minimizing cost versus time are inherently conflicting, necessitating a trade-off, as derived in chapter A.2.2. Thus, the Hohmann transfer selection function is adapted to incorporate this preference parameter $p_{\Delta v/\Delta t}$. The waiting duration to reach a transfer initiation point is calculated from the current true anomaly using equation (2.8), requiring a transformation to the eccentric anomaly via equation (2.7).

$$\Delta t_{\text{wait}} = \frac{M_2(\nu_2, e) - M_1(\nu_1, e)}{\sqrt{\frac{\mu}{a^3}}} \tag{3.12}$$

The direction of motion on the orbit is important; if $\nu_2 < \nu_1$, the calculation must be adjusted to $\nu_2 + 2\pi > \nu_1$ to compute the correct waiting time from ν_1 to ν_2. After the Hohmann transfer, the orbit's semi-major axis a and eccentricity e are as required, but the true anomaly changes to $\nu_{\text{arrival}} = \nu_{\text{transfer}} + \pi$.

Rendezvous: Change of true anomaly $\Delta\nu$

The rendezvous of two spacecrafts translates into a change of true anomaly, achievable through the following manoeuvres:

1. Phasing at the point of intersection between a phasing and a target orbit. This method is applicable for adjusting exclusively the true anomaly when the spacecraft is already positioned within the target orbit.

2. In conjunction with an altitude change through a Hohmann transfer, the spacecraft remains in the initial orbit until the appropriate true anomaly is reached for the transfer to the final altitude. Refer to section A.2.2 for manoeuvre computations.

A phasing manoeuvre, illustrated in figure 3.7, adjusts the orbital phase by transferring the servicer at either apogee or perigee. Afterwards, the servicer and client complete a specified number of orbits before rendezvousing. The total number of orbits completed by the servicer in the phasing orbit is denoted as k_1, while the client completes k_2 orbits in its respective orbit. Multiple discrete solutions, denoted (k_2,k_1), exist offering different levels of performance. The choice of the phasing orbit's semi-major axis affects the transfer strategy, duration, and cost Δv.

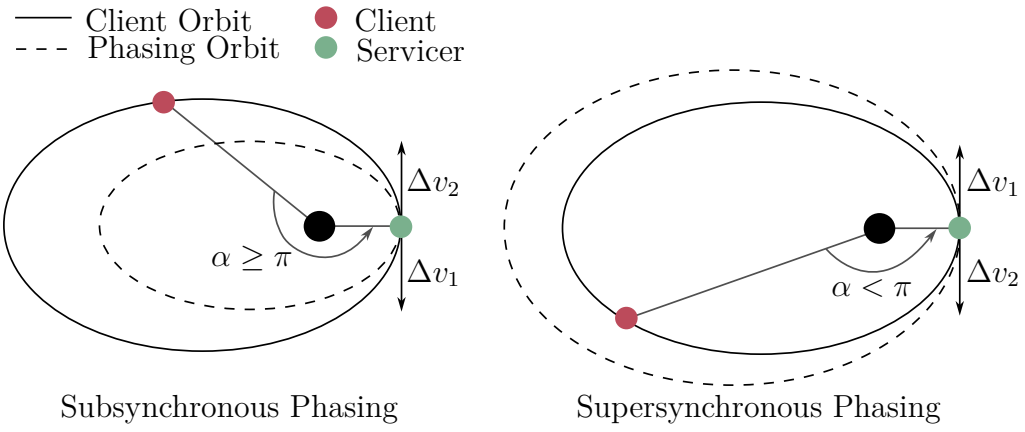

Figure 3.7.: Phasing Manoeuvres for Rendezvous

The design of the phasing orbit to eliminate the angle α, measured from the client to the servicer, follows this strategy:

1. The transfer strategy is selected based on the angle α as figure 3.7 indicates. If the client is behind the servicer ($\alpha < \pi$), supersynchronous phasing to a higher phasing orbit is initiated. A subsynchronous phasing orbit is chosen in case the client is in front of the servicer ($\alpha \geq \pi$). When $\nu_{\text{servicer}} \geq \nu_{\text{client}}$, $\alpha = \nu_{\text{servicer}} - \nu_{\text{client}}$; otherwise $\alpha = 2\pi - (\nu_{\text{client}} - \nu_{\text{servicer}})$.

2. With defined constraints for the time of flight, minimum and maximum number of client orbits before rendezvous k_2 are calculated according to $k_{2,\max/\min} = \frac{\mathrm{TOF}_{\max/\min}}{\mathrm{P}_{\mathrm{client}}} - \frac{\alpha}{2\pi}$ (2.27). All integer values in between are candidate solutions.

3. Constraining the phasing altitude, which defines the solution search space around the orbit, and increasing the number of complete phasing orbits k_1, the phasing orbit altitude $a_{\mathrm{phasing}} = a_{\mathrm{client}} \left(\frac{\alpha + 2\pi k_2}{2\pi k_1} \right)^{2/3}$ (2.28) is consecutively computed for all combinations of (k_2, k_1). Table 3.5 shows the parameters employed for this use case with $a_{\mathrm{phasing,\ max}} = (1 + m) \cdot a_{\mathrm{client}}$.

Table 3.5.: Phasing Manoeuvre Parameters

Parameter	Value	Description
$\mathrm{TOF}_{\max}$	10 d	Maximum time of flight for phasing manoeuvre
Phasing Δa Search Factor m	0.5	Maximum phasing altitude $\mathrm{a}_{\max}$ search factor

4. For valid (k_2, k_1), the algorithm obtains $\mathrm{TOF} = \mathrm{P}_{\mathrm{phasing}} = 2\pi k_1 \sqrt{\frac{a_{\mathrm{phasing}}^3}{\mu}}$ (2.26). In circular orbits, the transfer point is independent of the true anomaly, allowing it to begin at the current position. Otherwise, for both phasing strategies, the manoeuvre is initiated at perigee, where small Δv result in the most efficient change in orbital period due to the Oberth effect. The waiting time t_{wait} is computed as the time to reach the transfer point from current true anomaly (3.12). The phasing cost is

$$\Delta v_{\mathrm{phasing}} = 2 \cdot \left| \sqrt{\frac{2\mu}{r_{\mathrm{phasing}}} - \frac{\mu}{a_{\mathrm{client}}}} - \sqrt{\frac{2\mu}{r_{\mathrm{phasing}}} - \frac{\mu}{a_{\mathrm{phasing}}}} \right| \tag{3.13}$$

5. Each candidate solution of the form $\left[k_2, k_1, a_{\mathrm{phasing}}, \Delta v_{\mathrm{phasing}}, \mathrm{TOF}, t_{\mathrm{wait}}\right]$ is compared in terms of $\Delta v_{\mathrm{phasing}}$ and TOF. The solution is selected based on the input parameter $p_{\Delta v/\Delta t}$, indicating the priority between cost ($p_{\Delta v/\Delta t} = 0.0$) and duration ($p_{\Delta v/\Delta t} = 1.0$). The algorithm normalizes Δv and Δt across candidate solutions. A combined score, *sc*, is calculated following equation (3.14) for each solution, the candidate with the lowest score is selected as the optimal phasing manoeuvre for the given trade-off selection.

$$\mathrm{sc} = p_{\Delta v/\Delta t} \cdot \frac{\mathrm{TOF} - \mathrm{TOF}_{\min}}{\mathrm{TOF}_{\max} - \mathrm{TOF}_{\min}} + (1 - p_{\Delta v/\Delta t}) \cdot \frac{\Delta v - \Delta v_{\min}}{\Delta v_{\max} - \Delta v_{\min}} \tag{3.14}$$

Figure 3.8 and 3.9 depict the procedure for a supersynchronous transfer from client 10 to 2 with $\alpha = 114°$. Candidate solutions (k_2, k_1) show varying performance, with Δv plotted as a function of phasing to client orbit semi-major axis (fig. 3.8), and corresponding TOF values marked as points along the same axis (fig. 3.9). The selected solution $(7, 7)$, marked with a red cross, represents $p_{\Delta v/\Delta t} = 0.1$.

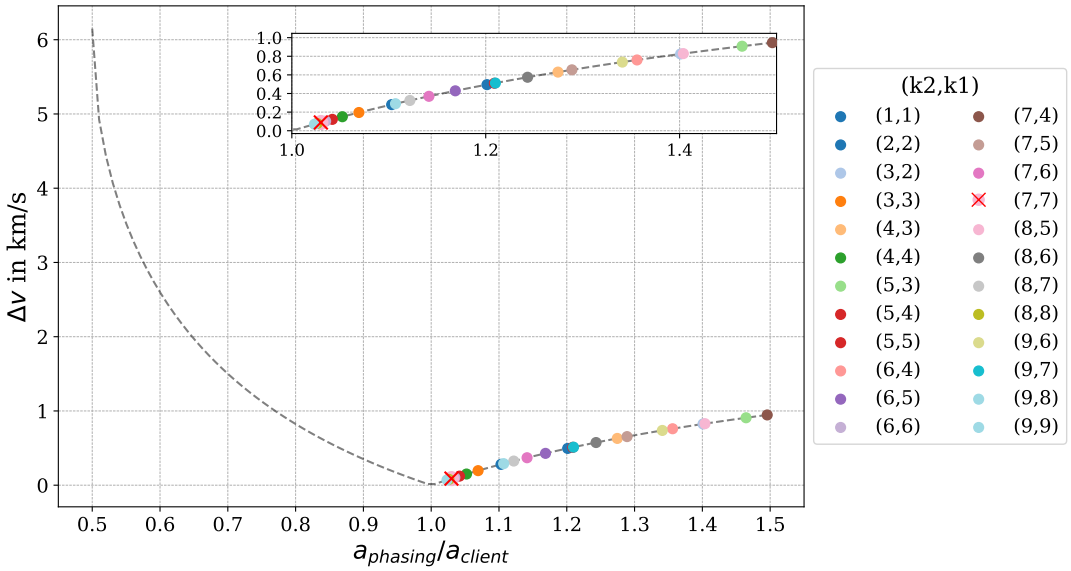

Figure 3.8.: Δv Comparison of Supersynchronous Phasing Manoeuvres

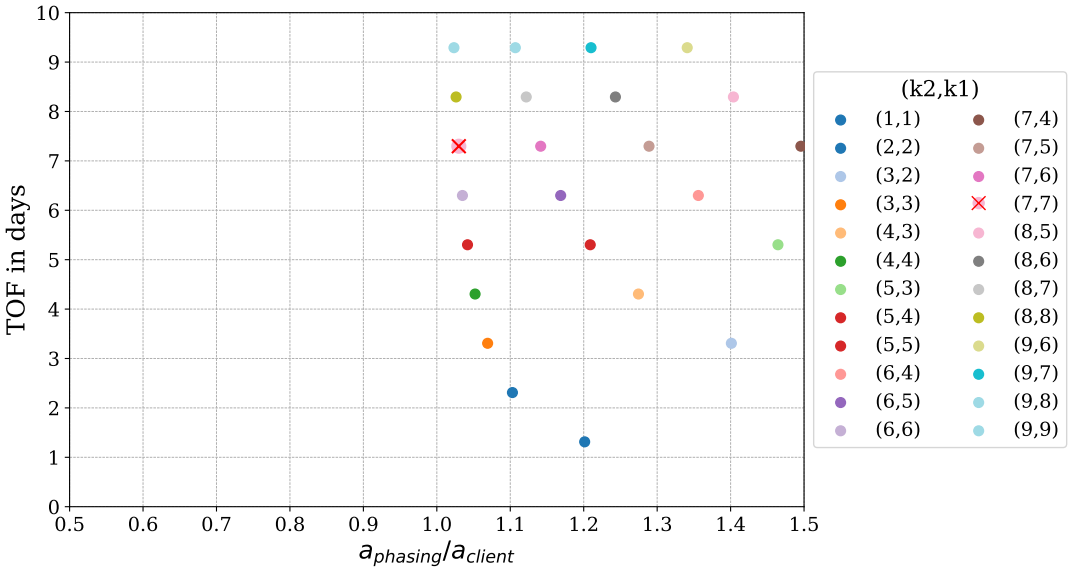

Figure 3.9.: TOF Comparison of Supersynchronous Phasing Manoeuvres

As the number of complete orbits k_2 increases, the TOF extends, while these longer-duration solutions demand less Δv. The plots show that closer phasing orbits demand

less Δv while offering an entire range of TOF options, making them preferable: The first garland-like line for TOF represents solutions with $k_2 = k_1$, showing the lowest Δv for the same TOF compared to solutions where the servicer completes fewer orbits. With decreasing k_1, the altitude differences from the client orbit are greater, leading to higher velocity requirements.

For subsynchronous transfers, the number of candidate solutions increases for the same $\mathrm{TOF}_{\max}$ due to the shorter orbital period. Figure 3.10 and A.3 demonstrate the effect. The depicted transfer corresponds to phasing from client 2 to 10 with $\alpha = 246°$.

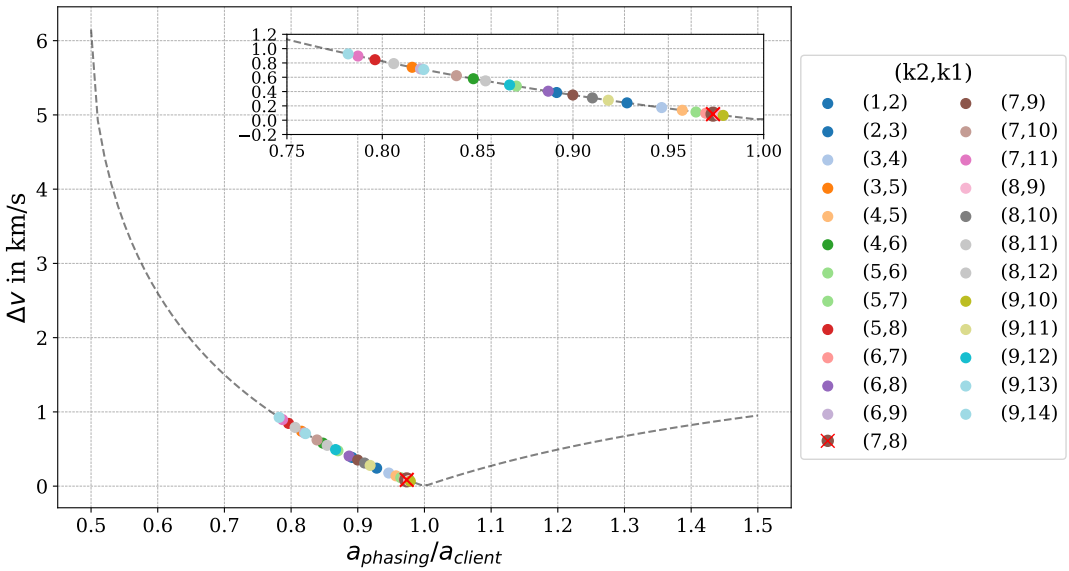

Figure 3.10.: Δv Comparison of Subsynchronous Phasing Manoeuvres

With an increase in manoeuvre options, the maximum cost among these, $\Delta v_{\max}$, also rises. However, all other extreme values for normalization remain comparable between subsynchronous and supersynchronous phasing at the same relative phase difference. This leads to a shift in scoring prioritizing duration favouring costlier transfers. Consequently, routing decisions are inherently restricted to supersynchronous orbits, even though subsynchronous transfers offer similar TOF and costs among the candidate solutions. Therefore, the lower phasing orbit altitude is bound to the same $\Delta v_{\max}$ as the upper supersynchronous orbit. With given input factor $m = \frac{a_{\text{phasing,sup}}}{a_{\text{client}}}$, $n = \frac{a_{\text{phasing,sub}}}{a_{\text{client}}}$ can thus be calculated using formula (3.17). As the velocity impulse acts in opposite directions for the two strategies, equation (3.16) is derived for equal absolute $\Delta v_{\max}$ (3.15) with $l = \frac{a_{\text{phasing}}}{a_{\text{client}}}$.

$$\Delta v_{\max} = 2 \left| 1 - \sqrt{\frac{2l-1}{l}} \right| \sqrt{\frac{\mu}{a_{\text{client}}}} \tag{3.15}$$

$$1 - \sqrt{\frac{2m-1}{m}} = -\left(1 - \sqrt{\frac{2n-1}{n}}\right) \quad (m < 1, n > 1) \tag{3.16}$$

$$m = \left(2 - \left(2 - \sqrt{2 - \frac{1}{n}}\right)^2\right)^{-1} \tag{3.17}$$

Inclination Change Δi

In addition to these in-plane changes, out-of-plane manoeuvres are required. Inclination changes can be achieved through the following manoeuvres:

1. Pure inclination change through rotation around the apsidal line as a single-impulse manoeuvre at the orbit's furthest point from the attractor. This manoeuvre is restricted to the ascending or descending node, requiring $\omega_p = 0$ or $\omega_p = \pi$.

2. Simultaneous inclination and RAAN change performed at the intersection line of two orbits. This manoeuvre is herein valid only for transfers between circular orbits at the same altitude, as it relies on spherical trigonometric relations to determine orbital properties.

3. If an altitude change is required, a Hohmann transfer with simultaneous inclination change is more efficient. This transfer requires alignment of the apsidal line and must be executed at the ascending or descending node to avoid altering other orbital parameters. Details of this manoeuvre are provided in section A.2.2.

A simultaneous inclination and RAAN change, as in equation (2.31), is inherently more efficient than conducting separate manoeuvres for each [66]. When a pure inclination change is performed away from the ascending node, it automatically induces a change in RAAN as well. With given inclinations and RAAN of both orbits, the total plane change angle Θ is calculated with formula (2.30). The thrust is to be applied at ν_1 following equation (2.29) which requires $\omega_{p,1}$.

$$\Theta = \arccos\left(\cos i_1 \cos i_2 + \sin i_1 \sin i_2 \cos\left(\Omega_2 - \Omega_1\right)\right) \tag{3.18}$$

$$\nu_1 = \arccos\left(\frac{\cos i_1 \cos\Theta - \cos i_2}{\sin i_1 \sin\Theta}\right) - \omega_{p,1} \tag{3.19}$$

The required velocity for the manoeuvre is obtained inserting equations (2.11), (2.6), (3.18) and (3.19) in equation (2.31)

$$\Delta v = 2v_1(\nu_1)\sin\left(\frac{\Theta}{2}\right) = 2\sqrt{\frac{\mu}{r_1}}\sin\left(\frac{\Theta}{2}\right) \tag{3.20}$$

The time to reach the required ν_1 on the initial orbit depends on the current position of the spacecraft. While the thrust itself is instantaneous, this time is accounted for as

$$\Delta t_{\text{wait}} = \frac{\nu_{1,transfer} - \nu_{1,current}}{2\pi} P_1 \tag{3.21}$$

Spherical trigonometry gives the change of argument of periapsis due to the plane change. The 2nd Law of Cosines applied to the spherical triangle in figure 3.11 determines u_2. ν_2 is given by the point of intersection allowing to find $\omega_{p,2}$.

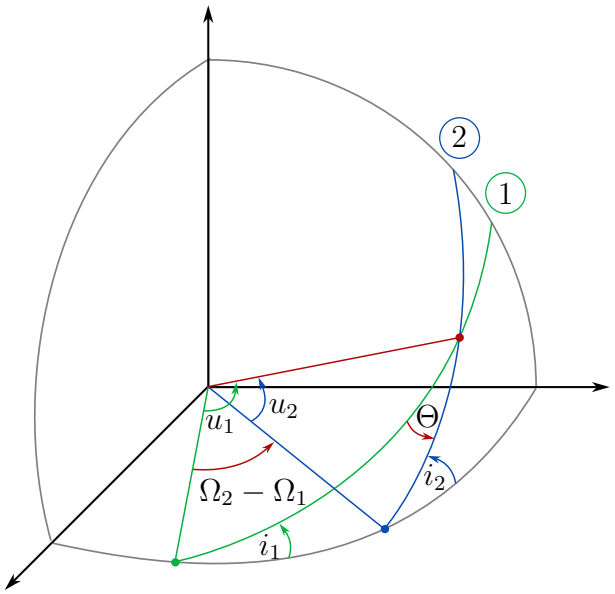

Figure 3.11.: Spherical Triangle

$$u_2 = \arccos\left(\frac{\cos i_1 - \cos i_2 \cos\Theta}{\sin i_2 \sin\Theta}\right) \tag{3.22}$$

$$\omega_{p,2} = u_2 - \nu_2 \tag{3.23}$$

To find the intersection, the position vector of orbit 1 at known intersection point is

transformed into ECI coordinates.

$$\vec{r}_{\text{ECI},1} = R_z(\Omega_1)R_x(i_1)R_z(\omega_{p,1})\vec{r}_{\text{perifocal, 1}} \tag{3.24}$$

$$\vec{r}_{\text{perifocal},2} = R_z(-\omega_{p,2})R_x(-i_2)R_z(-\Omega_2)\vec{r}_{\text{ECI},1} \tag{3.25}$$

$$\nu_2 = \arctan 2(\vec{r}_{\text{perifocal},2,x}, \vec{r}_{\text{perifocal},2,y}) \tag{3.26}$$

In the case of $\Omega_2 < \Omega_1$, the computation is conducted following the same methodology inversely assigning orbit annotations.

If one of the orbits is not inclined, and an intersection occurs at the ascending or descending node, a pure inclination change manoeuvre of $\Delta i = |i_2 - i_1|$ following equation (2.33) is feasible. The same applies when both orbits share the same RAAN, with an intersection at these nodes.

$$\Delta v = 2v \sin\left(\frac{|i_2 - i_1|}{2}\right) = 2\sqrt{\frac{\mu}{r}} \sin\left(\frac{|i_2 - i_1|}{2}\right) \tag{3.27}$$

For a general elliptical orbit, this can only be performed without altering other orbital parameters if the inclination change is applied at perigee or apogee, coinciding with the ascending or descending node. Thrust is applied at apoapsis since velocity is lower.

$$\Delta v = 2v(r_a) \sin\left(\frac{|i_2 - i_1|}{2}\right) = 2\sqrt{\frac{2\mu}{a(1+e)} - \frac{\mu}{a}} \sin\left(\frac{|i_2 - i_1|}{2}\right) \tag{3.28}$$

RAAN Change $\Delta\Omega$

Various manoeuvres can be employed to change the RAAN of an orbit. In the chosen use case of GEO satellites, client orbits exhibit the greatest variation in Ω.

1. Out-of-plane change manoeuvres with the use of simultaneous inclination change according to formula (3.20). It is time efficient, but requires thrusting.

2. In an ideal geostationary orbit, RAAN and true anomaly can be used interchangeably, assuming zero argument of perigee. Thus, phasing is sufficient to adjust the RAAN without requiring a plane change, provided both orbits lie in the same plane. The time and cost efficiency of the transfer depend on the selected phasing solution.

3. RAAN drift caused by J2-perturbations, according to equation (2.16), does not require thrusting but is time-intensive. For geostationary orbits, the changes in

RAAN and argument of perigee are not significant over the timescale of the planned refuelling mission.

$$\dot{\Omega} = -\frac{3\sqrt{\frac{\mu}{a^3}}J_2 R_E^2}{2a^2\left(1-e^2\right)^2}\cos\left(i\right) = -2.7021 \times 10^{-9}\text{rad/s} = 0.0133°/\text{day} \tag{3.29}$$

$$\dot{\omega_p} = \frac{\dot{\Omega}}{\cos\left(i\right)}\left[\frac{5}{2}\sin^2\left(i\right) - 2\right] = 5.4042 \times 10^{-9}\text{rad/s} = 0.0267°/\text{day} \tag{3.30}$$

Drifting is not considered a manoeuvre option, nor is it treated as a perturbation. Since all clients share the same orbital altitude with small inclinations, the relative differences in Ω and ω_p are insignificant.

4. A pure RAAN change can only be executed over the North or South Pole, requiring rotation around the Earth's axis, making such single-burn manoeuvres relevant solely for polar orbits, which are outside the scope of this thesis.

Change of argument of perigee $\Delta\omega_p$

The argument of periapsis can be adjusted at an intersection point of two elliptical coplanar orbits with $a_1 = a_2 = a$ and $e_1 = e_2 = e$, by rotating the apsidal line by $\Delta\omega_p$. The manoeuvre starts at a true anomaly of $\nu_1 = \frac{\Delta\omega_p}{2}$ [41], and the spacecraft arrives at $\nu_2 = 2\pi - \frac{\Delta\omega_p}{2}$. The argument of perigee correction $\Delta\omega_p$ requires [15]

$$\Delta v = 2e\sqrt{\frac{\mu}{a\left(1-e^2\right)}}\sin\left(\frac{\Delta\omega_p}{2}\right) \tag{3.31}$$

For circular orbits, the argument of periapsis does not require a change manoeuvre, resulting in zero cost. However, the argument of perigee serves as a reference for the true anomaly.

3.2.3. Trajectory: Orbit Change Strategy and Determination

Trajectory selection follows a general geosynchronous model applicable in a stationary scenario where orbit transfer costs remain constant. This model approximates real orbits for logistics optimization as described in section 3.1.3. Notably, all orbits share the same period and semi-major axis, a_{GEO}, with zero eccentricity, ensuring no relative motion. Orbits differ in RAAN, representing the phase position above Earth's equator, and in inclination. The argument of perigee is assumed to align with the ascending node. The stationary mode is used for all transfers between GEO orbits. A general mode is devel-

oped for selecting a trajectory for a general transfer between two orbits without property constraints. This model is used for transfers where geosynchronous assumptions are inapplicable, such as GTO to GEO insertion. It can also be extended in future works to calculate actual manoeuvres after optimizing the spacecraft visitation order. All manoeuvre strategies yield Δv and TOF for the required orbit change with rendezvous. Based on the cost-duration priority $p_{\Delta v/\Delta t}$, the algorithm selects the optimal strategy to achieve the desired trade-off with equation (3.14).

Stationary Orbit Change

The trajectory is composed of a series of manoeuvres presented in section 3.2.2, following the logic of subsequent changes of orbital parameters. To manoeuvre between geosynchronous clients, the trajectory options depending on initial and final orbit properties are depicted in figure 3.12 simplifying the complete selection process in figure A.8.

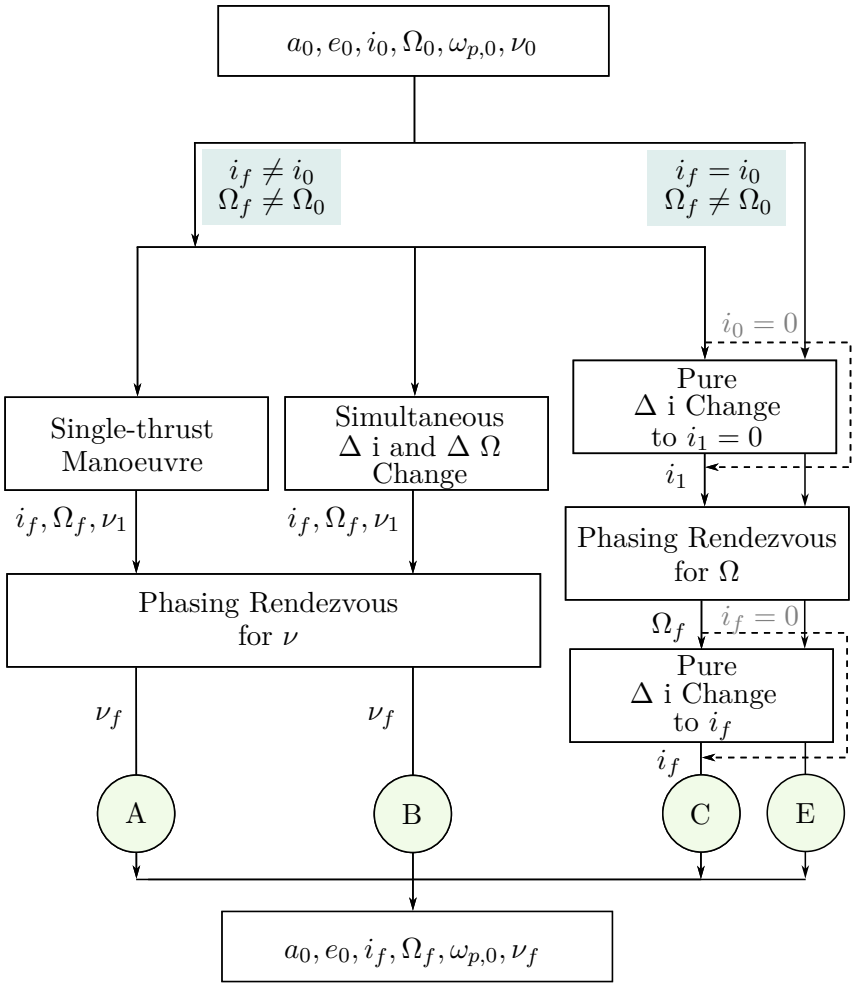

Figure 3.12.: Trajectory Determination through Orbit Change Strategy Selection

All transfers between clients in the selected use case necessitate a RAAN change. If orbits differ also in inclination, trajectory options (A) through (C) are available, otherwise trajectory (E) is executed. Changing RAAN and inclination is possible through: Single-thrust with subsequent phasing (A), simultaneous inclination and RAAN change with subsequent phasing (B) and phasing for RAAN combined with inclination changes between inclined orbits and equatorial plane (C). A single thrust manoeuvre (A) at intersection alters all orbital parameters simultaneously, with the exception of true anomaly. Consequently, additional phasing for ν is necessary to achieve rendezvous of spacecraft. For the feasibility of this approach, it is essential that the optimization algorithm finds an intersection, which is computationally expensive. Similarly, trajectory (B), changing Ω and i simultaneously in an out-of-plane manoeuvre, incurs a comparable cost Δv, as both are single-impulse manoeuvres. When no intersection is found, trajectory (B) remains executable. However, it necessitates additional plane changes to enable computation, by definition, when the orbits have zero inclination, as well as potentially requires rotation of the apsidal line, as outlined in A.8. Trajectory (C) is specific to the assumptions at hand. In geostationary orbits with $i = 0$ and $\omega_p = 0$, Ω and ν are interchangeable. Thus holding ν constant, the method leverages the true anomaly change function to effectuate the necessary adjustments in Ω. As this phasing for Ω is only applicable within the equatorial plane, an initial inclination change to $i = 0$ is required, succeeded by a final inclination change to final inclination i_f. Trajectory (E) for a pure RAAN change is analogous to (C). However since $i_0 = i_f$ holds for (E), either no or two inclination changes of the same magnitude to and from the equatorial plane are performed. In contrast, (C) always necessitates at least one additional inclination change before or after phasing for Ω.

When orbits intersect, all strategies yield the same phasing angle, $\alpha = \Omega_1 - \Omega_2$, leading to identical phasing manoeuvres. Comparing trajectories (A) and (C), phasing for ν after a single-thrust manoeuvre is equivalent to correcting Ω through phasing in equatorial plane. However, intermediary transfers to the equatorial plane, increase transfer cost Δv compared to (A). Otherwise, (A) and (C) result in the same Δv. Phasing for Ω is faster, as it is initiated directly at the ascending or descending node, while single-thrust manoeuvres must occur at orbit intersections, equating the durations only if the intersection occurs at the initial point. When one orbit's inclination is non-zero, (B) is slightly costlier than (A) as the additional changes to slightly inclined orbits are accounted for. Owing to the high computational cost of optimizing orbit intersections for strategy (A), this trajectory option is excluded from client transfers within design iterations of the refuelling architecture. However, it remains implemented for verification and general mode computations.

General Orbit Change

The generic trajectory design methodology in figure A.9, not restricted to the scenario at hand, is developed for all mission phases that do not take place within the scope of stationarity. Within the OOR scenario, this involves the insertion from GTO into GEO. If the launch occurs at the optimal time, a rendezvous computation is not required, and insertion into the depot orbit is assumed at the corresponding true anomaly. The single-thrust trajectory (A) finds an intersection at GTO apogee resulting in a required $\Delta v \approx 1\,491\,\mathrm{m/s}$. Computation via the law of cosines (2.32), where in- and out-of-plane change for GEO insertion are applied simultaneously as in (3.32), confirms this value. Trajectory (B) in the general mode entails a Hohmann transfer at apogee $r_a = a_{\mathrm{GEO}}$ with $\Delta v \approx 1\,472\,\mathrm{m/s}$ (3.33) and a simultaneous change of Ω and $\Delta i = 6°$ by $\Delta v \approx 322\,\mathrm{m/s}$ (3.34). Trajectory (A) is around 300 m/s more cost and time efficient, making it the preferred choice for all GEO insertion phase computations, given $p_{\Delta v/\Delta t} = 0.1$.

$$\Delta v_{\mathrm{GTO}\,\rightarrow\,\mathrm{GEO}} = \sqrt{\frac{4\mu}{a_{\mathrm{GEO}}} - \frac{2\mu}{a_{\mathrm{GTO}}} - 2\sqrt{\frac{2\mu}{a_{\mathrm{GEO}}} - \frac{2\mu}{a_{\mathrm{GTO}}}}\sqrt{\frac{2\mu}{a_{\mathrm{GEO}}}}\cos\left(\Theta\right)} \tag{3.32}$$

$$\Delta v_{\mathrm{Hohmann,\ GTO}\,\rightarrow\,\mathrm{GEO}} = \sqrt{\frac{2\mu}{a_{\mathrm{GEO}}} - \frac{2\mu}{a_{\mathrm{GTO}}}} - \sqrt{\frac{2\mu}{a_{\mathrm{GEO}}}} \tag{3.33}$$

$$\Delta v_{\Theta,\mathrm{GTO}\,\rightarrow\,\mathrm{GEO}} = 2\sqrt{\frac{2\mu}{a_{\mathrm{GEO}}}} \cdot \sin\left(\frac{\Theta}{2}\right) \tag{3.34}$$

This general methodology can be employed to quantify the effects of the simplifications made assuming perfect stationary orbits allowing for simplified manoeuvre computations. These amount to a marginal deviation of a maximum of 5 m/s for transfers between client satellites in the stationary case. Given the increased complexity of the methodology, it is therefore not utilized in the simulation after optimization to reduce computational complexity and processing time. However, this approach is implemented in the logistics tool and remains applicable to insertion computation in the use case at hand, other scenarios or future model enhancements.

3.2.4. Space Logistics Optimization: Solving the CVRP for On-Orbit Refuelling with a Genetic Algorithm

The logistics optimization problem at hand is a CVRP, as formulated in section 2.3.1, constrained by servicer capacities that cannot be exceeded and scenario-specific restrictions, such as single-return routes. The solution strategies for the Capacity Vehicle

Routing Problem include heuristic and metaheuristic methods to address its NP-hard nature as presented in chapter 2.3.2. The Clarke and Wright Savings Algorithm offers a faster, simpler solution by optimizing routes and determining servicer numbers, while the Genetic Algorithm provides greater design flexibility and superior solutions for complex scenarios. The GA was selected for its capacity to explore a range of servicer numbers, despite the higher computational cost, and its potential for extension to multi-objective optimization. Different types of GA were further successfully applied in related literature.

In the CVRP, the solution consists of a set of routes assigned to a fleet of vehicles. In the context of a GA, a candidate solution, or individual, must be encoded in a way that inherently accounts for the specific constraints of the scenario within its structure. The individuals in the developed GA are represented by two tailored arrays: one capturing the visitation order of clients, and the other assigning the appropriate vehicle. Since all routes start and end at the depot, the first array contains as many zero entries at the start and end as there are servicing vehicles, representing the depot. The second array assigns the corresponding vehicles to each route. Figure 3.13 depicts this representation and all steps of the developed GA. The methods for individual creation, fitness evaluation, crossover, mutation operations, and feasibility checks are specifically tailored to the CVRP at hand, as outlined below. The parameters of the genetic algorithm include the initial population size N_{POP}, crossover probability PB_{CX}, mutation probability PB_{MUT}, and the number of generations N_{GEN}. All parameters must be carefully selected to suit all design points in the scenario, keeping a balance between maintaining solution quality, ensuring sufficient exploration of the solution space, and minimizing computational effort.

1. The random initial population consists of a defined number of individuals, significantly fewer than the total number of candidate solutions [96]. A large initial population ensures diversity and avoids premature convergence to suboptimal solutions, but reduces computational efficiency. The number of generations must be sufficient for the algorithm to converge. As the number of servicing vehicles approaches the O2O scenario, the complexity of the optimization problem decreases. Consequently, the population size is reduced in a linear manner, as determined by an equation derived from experimental analysis of convergence behaviour with the number of clients n and the number of servicers m: $N_{\mathrm{POP}} = \left\lfloor \frac{600m}{1-n} + \left(700 - \frac{600}{1-n}\right) \right\rfloor$. With reduced complexity, the number of generations required for convergence also diminishes, establishing a direct relationship with the decrease in population size, expressed by $N_{\mathrm{GEN}} = \lfloor 0.4 \cdot N_{\mathrm{POP}} \rfloor$.

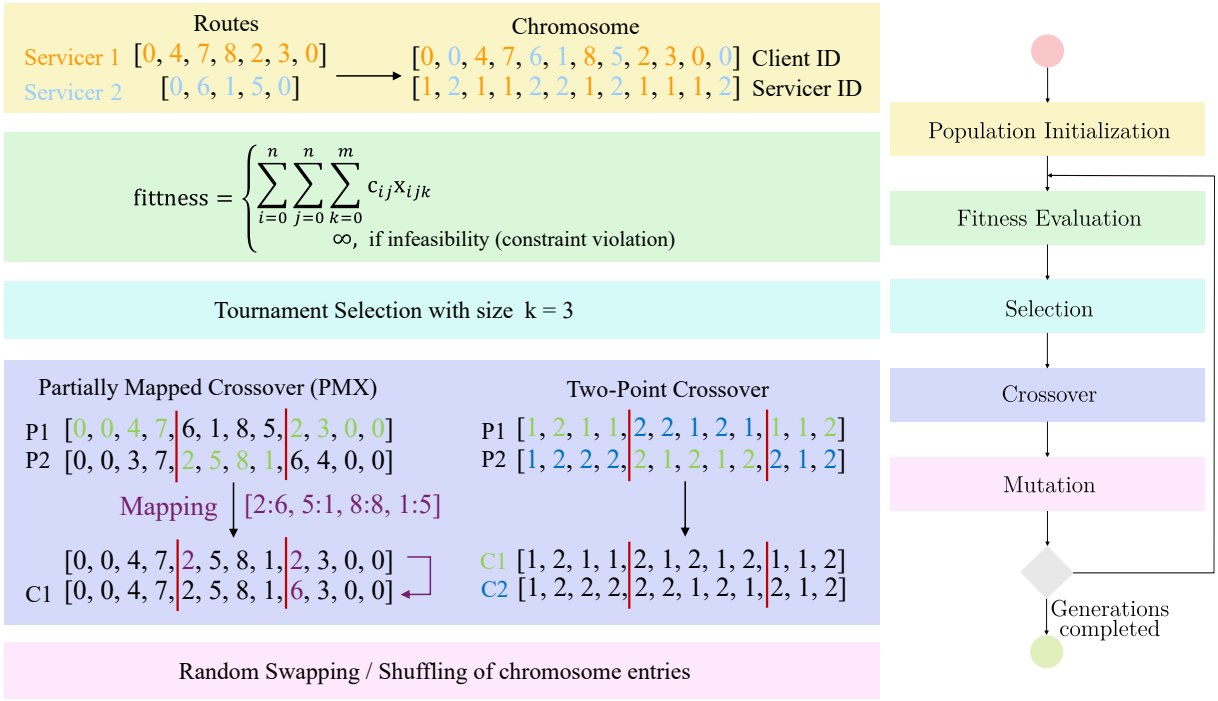

Figure 3.13.: Implementation of Genetic Algorithm

2. The individuals are evaluated using the objective function (2.39) for cost minimization in terms of Δv. The method constructs routes based on the individual's encoding and calculates the cost for each route. Infeasible solutions are penalized by assigning them an infinite cost, rather than the actual cost values from the route computations.

3. Tournament selection chooses the fittest individuals from a pool of k candidates. A higher k increases the likelihood of selecting highly fit individuals, but also raises the risk of premature convergence. A balanced trade-off was achieved with $k = 3$, determined through empirical testing to ensure robust convergence.

4. When adapting the solutions, it is essential to ensure that all clients are serviced. Therefore, a crossover operation must be defined to maintain this requirement. Partially Mapped Crossover (PMX) is used to modify the client list, ensuring all clients are preserved and the gene order is retained from both parents, promoting convergence in permutation-based optimization problems [47]. The PMX algorithm generates one child from two parents [63, 89]. As displayed in figure 3.13 for a specific example with eight clients and one depot, two random cut points are selected to construct a child and a mapping table. The next step is resolving duplicate clients in the child using the mapping table to ensure that all clients are visited. For the second list of attributed vehicles, a two-point crossover technique is chosen

to create two offspring [89]. Two random cut points are selected from the parents, then the middle section from one parent is combined with the entries outside the cut from the other parent to construct two children, each using the other's middle segment. Both crossover operations are designed to preserve the inherent structure of the individual, respecting the route constraint for depots. Random cuts are made beyond the index of the depot entries in the routes, and the crossover operations are feasible only for a number of clients greater than three. Crossover probability controls the recombination of genetic information, with high rates promoting diversity. Excessively high or low rates compromise solution quality.

5. Two mutation strategies are introduced: one for minor changes and another for more significant alterations. Minor variations are introduced by swapping two random entries in a list, while more significant changes involve shuffling entries between two random cuts. Mutation is applied to only one list within the individual, with both the mutation strategy and the list being selected at random. A high mutation probability enhances diversity through random changes, but must balance diversity with preserving good solutions. Hassanat et al. [37] find a Dynamic Decreasing of High Mutation Rate/Increasing of Low Crossover Rate (DHM/ILC) to show superior performance for large population sizes (≥ 200) to static rates. The rates change linearly with the generation number from 1 to 0 for Mutation Rate PB_{MUT}, and 0 to 1 for Crossover Rate PB_{CX}. With the current number of generation g, and the total number of generations N_{GEN}:

$$PB_{\mathrm{MUT}} = 1 - \frac{g}{N_{\mathrm{GEN}}} \tag{3.35}$$

$$PB_{\mathrm{CX}} = \frac{g}{N_{\mathrm{GEN}}} \tag{3.36}$$

6. A final feasibility check ensures compliance with the capacity constraint: the total client demands on each visited route must remain within the payload propellant capacity of the respective servicer attributed to the route.

To obtain a population of feasible solutions, only feasible individuals can be generated, which may increase computational effort. Raising the tournament size and mutation rate can promote the discovery of feasible solutions, but at the cost of the genetic algorithm's overall performance. Therefore, a loop is implemented to restart the algorithm if multiple generations fail to produce feasible solutions, ensuring a decoupling of the initial feasible population from the parameters themselves. In a final attempt, the initial population size

is significantly increased to test for feasible solutions. If no feasible solutions are found, it is assumed that the minimum number of vehicles needed to find a feasible solution is inherently insufficient due to strict capacity constraints. Even though the GA now minimizes Δv, it can equally be utilized for duration minimization replacing the cost matrix with the Δt matrix prior to optimization in its current version of implementation. The algorithm could be further easily extended for multi-objective optimization, enabling the concurrent minimization of Δv and Δt.

3.3. Implementation

The Technology Combination Analysis Tool (TCAT), developed by the EPFL Space Center, currently focuses on ADR and constellation deployment [7]. It supports engineers in the preliminary stages of mission design by evaluating different mission architectures and spacecraft configurations. This work aims to enhance TCAT's functionality by integrating an OOR scenario.

For implementation of the defined refuelling scenario and its use case, TCAT is extended with enhanced orbital transfer modelling, scenario optimization capabilities and OOR specific components. For refuelling scenario optimization, iterative infrastructure design is now implemented using the described GA, optimizing logistics during scenario setup. This first implementation step from figure 3.5 is a novelty requiring structural changes in the general tool setup. As mission options are limited to the needs of the current two scenarios, such as kick-stage deployment, additional components are required. New spacecraft, including servicer and depot, are introduced, alongside a launcher designed to support missions without kick-stages. A new module allows definition and manipulation of mission payloads, acting as propellant for OOR. A refuelling phase simulates fuel transfer across multiple actors and modes, and an approach phase models close-proximity operations. The existing capture phase is adapted for docking and undocking simulations. Additionally, the tool now supports a client satellite database, allowing for customizable and adaptable client satellites throughout the mission. Initial modelling of orbital dynamics in TCAT most significantly constrains the scope of possible missions and would not allow for this work. The new orbital transfer model supports full orbital parameter modification, enabling rendezvous, whereas the previous version only allowed for Hohmann transfers, inclination changes, and RAAN adjustments via J2 drifting not applicable in GEO. Supporting a $\Delta v/\Delta t$ trade-off, a universally valid trajectory selection process is now integrated, supporting both stationary and general

cases. These expansions improve mission flexibilities and capabilities for logistic scenarios.

The implementation within the tool follows the simplified structure in figure 3.14. The scenario is set up through user input, where a constellation of client satellites and a fleet of active spacecraft are defined based on the operational requirements. This setup includes specifying relevant orbits and spacecraft properties. It also contains the computation of the visitation sequence of clients by logistics optimization. During scenario execution, the fleet mission plan is executed. This involves configuring the required number of launch vehicles and other supporting spacecraft, such as servicers and depot, according to the scenario specifications. The spacecraft are initialized by defining their modules, which include propulsion, structure, payload, and docking systems. Once the fleet is operational, each spacecraft is assigned to service specific client satellites. The mission profile is then outlined, consisting of distinct mission phases, each associated with specific spacecraft modules. The subsequent execution of the mission plan applies each phase sequentially, modifying the state of the spacecraft and its modules, thereby simulating the entire mission progression. Upon successful simulation, KPIs and a detailed mission report are generated. Further information on the precise implementation are provided in appendix A.4 with the global architecture in figure A.10.

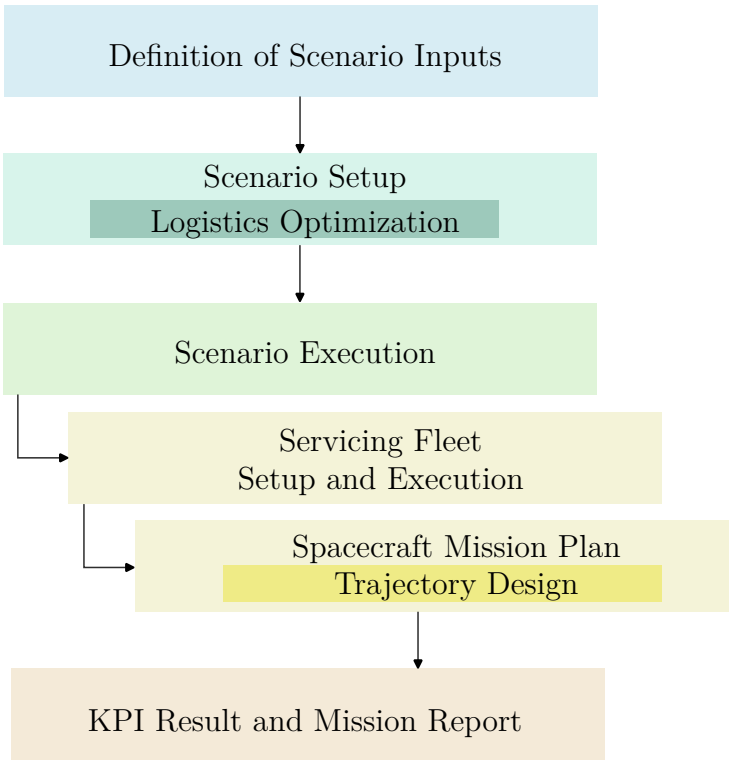

Figure 3.14.: Simplified Mission Simulation Structure in TCAT

4. Results

The core findings on trajectory selection, along with the corresponding transfer matrices and logistical optimizations, presented in chapter 4.1, are crucial for comprehending the performance outcomes across all infrastructure design points. These results, when integrated with simulation data, enable a comprehensive analysis of both the overall and detailed performance of various OOR architectures, specifically with respect to the two design variables: fleet size and depot placement, as discussed in chapter 4.2. The optimal architecture, in terms of minimizing total refuelling operation cost, is identified for the specified use case. Chapter 4.3 then critically examines the findings, highlighting the limitations of both the results and the employed methodology. Finally, chapter 4.4 offers general design recommendations and outlines potential areas for future research.

4.1. Trajectory Design and Routing Decisions

Prior to assessing the outcomes of various refuelling infrastructure configurations, it is imperative to rigorously analyse the results of the trajectory design in section 4.1.1 and logistics optimization in section 4.1.2. These results are provided for each design point, defined by servicer fleet size and depot location, within the scenario execution.

4.1.1. Transfer Results and Implications

The outcome of the trajectory design is encapsulated in three matrices, specifying transfer costs Δv (fig. 4.1), durations Δt (fig. 4.2), and manoeuvre strategies (fig. 4.3). The values on the x and y axes represent the IDs of the client satellites, numbered from 1 to 15, with the depot represented by 0, as illustrated in figure 3.3. The y-axis, corresponding to the rows, indicates the starting point of the transfer for a given ID, while the x-axis, corresponding to the columns, denotes the transfer's endpoint ID. Thus, the first row and column represent transfers associated with the depot orbit, which varies throughout the design process. The inner matrix, spanning IDs 1–15 along both axes, depicts the transfers between the client satellites and remains consistent across different depot locations.

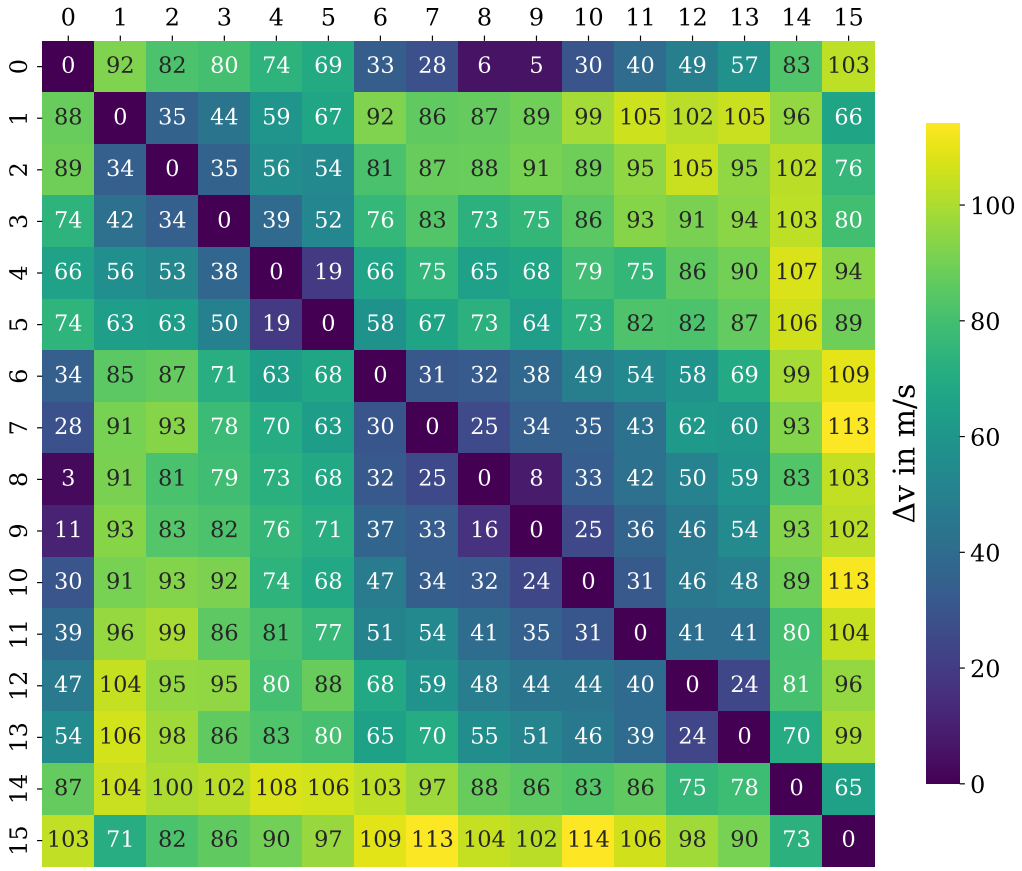

Figure 4.1.: Cost Δv_{OOR} Transfer Matrix for $p_{\Delta v/\Delta t} = 0.1$ and $\Omega = 0°$

Phasing manoeuvres predominantly influence the entries of the cost matrix for all transfers, due to the nearly circular nature of the orbits and small inclination variations. The maximum inclination change for the set of clients is 0.1°, necessitating a Δv of 5.4 m/s. The most significant impact of inclination adjustments is observed in the transfer between clients 7 and 8, where it constitutes approximately 20% of the total transfer cost, compared to 25 m/s required for phasing. The outcome in strategy matrix 4.3 contains the three available types of transfer trajectory, Ⓑ, Ⓒ, and Ⓔ, following the selection logic in figure 3.12. The strategies represent the sequential execution of orbital manoeuvres. Strategies Ⓑ and Ⓒ remain for the adjustment of RAAN and inclination. Single-thrust computation was eliminated due to its high computational demands, as it yields results identical to those obtained without it. Strategy Ⓔ is selected when no inclination change is required between client orbits. The corresponding Δt matrix entries represent the time of flight for strategy Ⓒ and Ⓔ. In the case of strategy Ⓑ, Δt entries encompass both the waiting duration required for initiating concurrent inclination and RAAN changes as well as the subsequent time of flight for phasing manoeuvres. The maximum TOF for

phasing manoeuvres is limited to 10 days, while the total transfer duration is constrained to 12 days. Given that one orbital period equates to one day, all concurrent RAAN and inclination changes are permitted. The maximum TOF, in conjunction with the priority parameter $p_{\Delta v/\Delta t}$, establishes the order of magnitude for both Δv and Δt. In scenarios where cost is the primary preference $p_{\Delta v/\Delta t} = 0.0$, all durations are close to the TOF_{max} as depicted in figure A.18b. The duration matrix presented in figure 4.2 illustrates Δt for the defined priority $p_{\Delta v/\Delta t} = 0.1$. For transfers characterized by lower total costs, thus for clients exhibiting lowest phasing differences, $p_{\Delta v/\Delta t}$ leads to the selection of reduced time of flight at the expense of cost, while still maintaining relatively low overall expenditures. Consequently, $p_{\Delta v/\Delta t}$ slightly diminishes the preference for lower-cost transfers in favour of higher-cost alternatives with lower durations during the route optimization process.

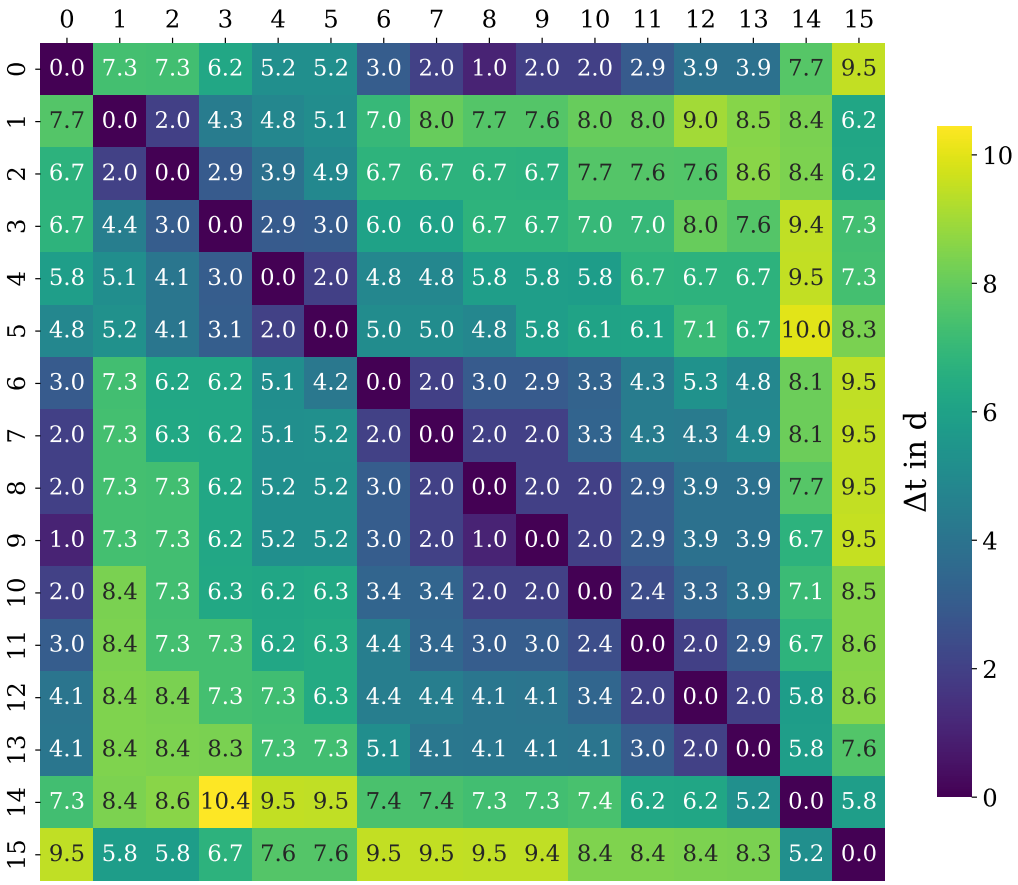

Figure 4.2.: Duration Δt_{OOR} Transfer Matrix for $p_{\Delta v/\Delta t} = 0.1$ and $\Omega = 0°$

The cost associated with phasing rises as the semi-major axis of the phasing orbit diverges further from the GEO altitude. As indicated by equation (2.28), the semi-major axis of the phasing orbit increases with an increasing phasing angle α, measured from the

	0	1	2	3	4	5	6	7	8	9	10	11	12	13	14	15
0		C	E	C	E	C	C	C	E	E	C	C	C	E	C	E
1	C		C	B	C	B	B	B	C	C	B	B	B	C	C	C
2	E	C		C	E	C	C	C	E	E	C	C	C	E	C	E
3	C	B	C		C	B	B	B	C	C	B	B	B	C	C	C
4	E	C	E	C		C	C	C	E	E	C	C	C	E	C	E
5	C	B	C	B	C		B	B	C	C	B	B	B	C	B	C
6	C	B	C	B	C	B		E	C	C	B	B	B	C	B	C
7	C	B	C	B	C	B	E		C	C	B	B	B	C	B	C
8	E	C	E	C	E	C	C	C		E	C	C	C	E	C	E
9	E	C	E	C	E	C	C	C	E		C	C	C	E	C	E
10	C	B	C	B	C	B	B	B	C	C		B	B	C	B	C
11	C	B	C	B	C	B	B	B	C	C	B		E	C	E	C
12	C	B	C	B	C	B	B	B	C	C	B	E		C	E	C
13	E	C	E	C	E	C	C	C	E	E	C	C	C		C	E
14	C	B	C	B	C	B	B	B	C	C	B	E	E	C		C
15	E	C	E	C	E	C	C	C	E	E	C	C	C	E	C	

Figure 4.3.: Transfer Strategy Matrix for $p_{\Delta v/\Delta t} = 0.1$ and $\Omega = 0°$

client to the servicer, as illustrated in graphic 3.7. In the context of supersynchronous phasing, with the servicer positioned ahead of the client, a reduction in the phasing angle corresponds to a decrease in the relative phase difference. Lowering the phasing orbit necessitates a smaller velocity change from GEO. Conversely, for subsynchronous phasing orbits, an increase in the phasing angle, now representing a decrease in relative phase, results in a higher phasing orbit. The spacecraft is thus closer to the GEO altitude, which leads to a reduction in the cost of the phasing manoeuvre. Thus, lower relative phase angles consistently yield lower transfer costs within the transfer matrix. Assuming a depot RAAN of zero, the servicers execute subsynchronous phasing manoeuvres to engage clients 9-15, while performing supersynchronous manoeuvres to await clients 1-8 in a higher orbit. The costs associated with transfers from $0 \rightarrow 1$ to $0 \rightarrow 8$ decreases as relative phase to the depot diminishes. In contrast, transitions from $0 \rightarrow 9$ to $0 \rightarrow 15$ exhibit increasing costs as the phasing angles increase. Transfers back from clients to the depot orbit require lower phasing orbits for routes $1 \rightarrow 0$ to $8 \rightarrow 0$ whereas higher phasing orbits are necessary for $9 \rightarrow 0$ to $15 \rightarrow 0$. Excluding the zero diagonal, which is not applicable since it does not imply any changes, the left and right sections of the diagonal predominantly represent transitions to lower and higher client numbers, respectively. Table 4.1 illustrates the trends described within the transfer matrix, which serves as the foundation for subsequent routing optimization, adhering to the aforementioned

logic. The cost matrix exhibits a symmetric structure. As the solutions are derived from a discrete set of options for subsynchronous and supersynchronous phasing, slight differences in symmetry are observed. Moreover, the preference for strategies Ⓑ or Ⓒ in matrix 4.3 as a transfer strategy result in small variations. Since the selection from discrete solutions is based on the trade-off model using equation 3.14, not all entries strictly follow the cost-based patterns described in table 4.1. Consequently, when interpreting transfer routes, it is essential to analyse the selected route entries, taking into account all three matrices to inform routing decisions. Simply assessing the phasing differences among clients is insufficient.

Table 4.1.: Phasing Strategy Matrix Analysis

Phase Angle	Phasing Mode	ID ↑	Example
$\alpha \geq \pi$	Subsynchronous	Δv ↑	1→2 to 1→13, 4→5 to 4→14
$\alpha < \pi$	Supersynchronous	Δv ↓	1→14 to 1→15, 4→1 to 4→3, 4 →15

4.1.2. Optimization Outcome for Routing Decisions

The output of the logistics optimization of each design point includes a convergence graph (fig. 4.4) to verify the quality of the solution, along with the selected routes (fig. 4.5) and their corresponding selected individual transfers (fig. 4.6). The convergence graph as depicted in figure 4.4 provides insights into the operation of the genetic algorithm and the quality of the solutions obtained. The function gives the best fitness value $\Delta v_{OOR,tot}$ (2.39) within the current population for each generation. As developed in the methodology, the parameters were tuned to achieve good convergence behaviour across all OOR design variable combinations. However, to ensure that the ideal optimum is found for each design point, the parameters would need to be experimentally adjusted on an individual basis. Analysing the solutions obtained through repeated executions of the genetic algorithm for the same design points yields insights into the remaining randomness inherent in the solutions generated by the GA. Even in cases where the convergence behaviour suggests premature convergence, the results are at most about 50 m/s away from the optimal solutions in terms of total cost. This indicates that the residual randomness does not distort the trends observed within the investigation of the design points. However, it may account for slight deviations from the ideal curves. During convergence towards ideal design points in the iteration process, as the total costs in the OOR process become more similar, this randomness becomes more restrictive in distinguishing performances of the solutions. This indicates a limit in precisely determining the final design variables.

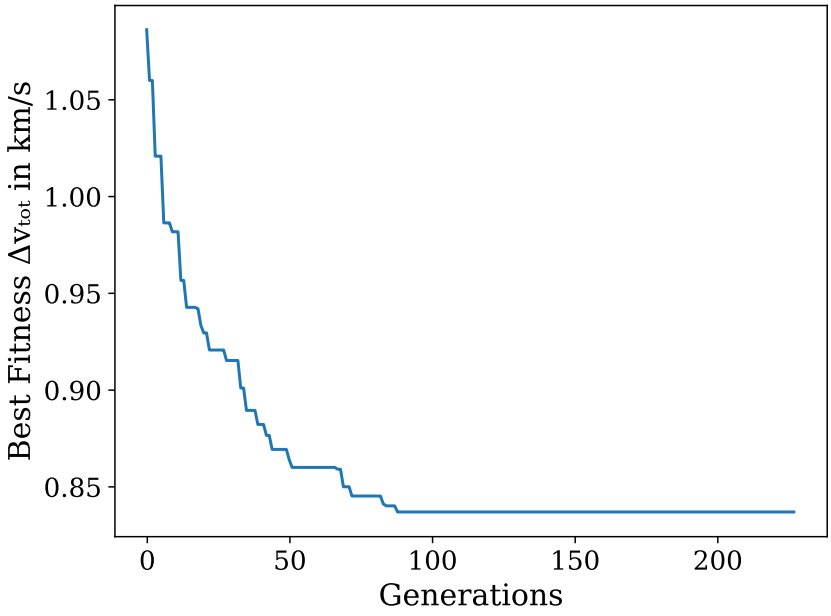

Figure 4.4.: GA Convergence for VRP with 4 Vehicles, $p_{\Delta v/\Delta t} = 0.1$ and $\Omega = 0°$

The routes are driven by variations in design variables and exhibit trends detailed and analysed in the following sections. Figure 4.5 presents the optimized refuelling routes for each of the four servicers, targeting all clients shown in grey.

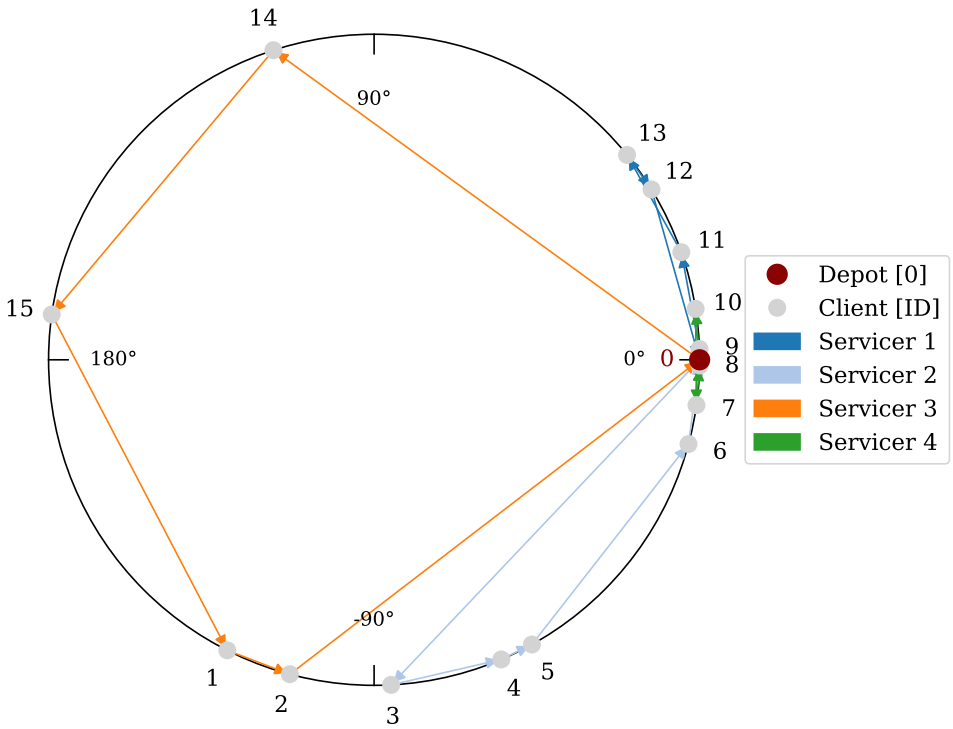

Figure 4.5.: Optimized Routes for 4 Servicers, with $p_{\Delta v/\Delta t} = 0.1$ and $\Omega = 0°$

The optimized routes for the depot at $\Omega = 0°$, illustrated by the red point with ID 0, represent a sequence of manoeuvres between client satellites. The routes in figure 4.5 correspond to entries in the cost and duration matrices in figures 4.6 and A.17. As an example, Servicer 3 manoeuvres along the route [0, 14, 15, 1, 2, 0], which spans the largest angular phase differences. This route, is indicated with red arrows in matrix 4.6, with the corresponding route costs for each orbit change highlighted in red boxes.

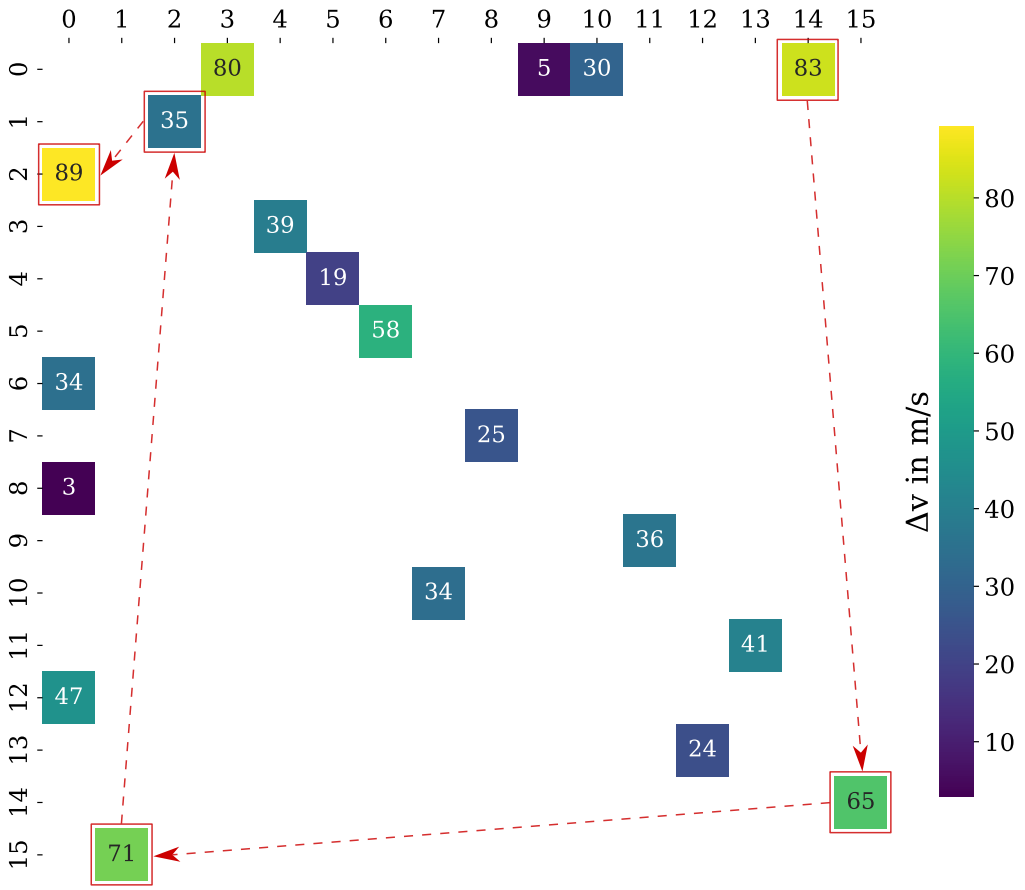

Figure 4.6.: Selected Route Costs for 4 Servicers, with $p_{\Delta v/\Delta t} = 0.1$ and $\Omega = 0°$

Analysing the selected entries in figure 4.6 from the complete matrix 4.1 provides insights into the algorithm's route construction process. As the number of servicers increases, more entries in the first row and column must be selected by the algorithm, as all routes must commence and conclude at the depot. This requirement constrains the remaining possible entries that can be selected from within the matrix. With a minimal number of servicers, transfers with low costs are predominantly chosen along the matrix diagonal. Additionally, lowest Δv entries for depot transfers are contained in the CVRP solution. Thus, to ensure that all clients are reached within a feasible route, occasional transfers with slightly higher Δv values are also selected.

4.2. Architectural Design Analysis for Mission Performance

In this chapter, the trajectory and logistics optimization results, previously analysed in chapter 4.1, are extended to allow for a more detailed examination of the design variables. Comprehensive simulations of the refuelling mission across the full range of these variables provide the KPIs for each OOR architecture explored in this study. The overall performance of the designed OOR missions, within the framework of the scenario definition, is presented herein. Additionally, the influence of the two design variables on mission performance is thoroughly analysed, focusing on the number of servicers in section 4.2.1 and the depot orbit Ω in section 4.2.2. The findings allow for general design recommendations within the scope discussed herein.

Overall On-Orbit Refuelling mission performance provides insights into the capabilities of the designed servicing mission. The total refuelling $\Delta v_{\mathrm{OOR,tot}}$, which is the sum of all individual refuelling route Δv values, ranges between 800 m/s and 2 700 m/s. It underscores the critical need for architectural design, particularly as these values are derived from a comprehensive optimization of each design parameter combination. The duration of the refuelling operations varies between 17 and 30 days, respectively. These magnitudes are governed by the choice of parameters $p_{\Delta v/\Delta t} = 0.1$ and $\mathrm{TOF}_{\mathrm{max}}$, and therefore represent the outcomes for this chosen compromise. For the defined scenario, smaller numbers of servicers result in the lowest total costs, and the design variable for the depot orbit can be situated within a range of approximately two degrees, depending on the number of servicers chosen. In the analysed use case, the optimal refuelling architecture is achieved with four servicers and a depot placed in a geostationary orbit with $\Omega = 2°$. Furthermore, the findings reveal overarching trends that provide valuable insights for the strategic design of refuelling architectures.

4.2.1. Number of Servicing Spacecrafts

For comparison of all design points of OOR infrastructure, performance in total refuelling operation route cost $\Delta \mathrm{v}_{\mathrm{OOR,tot}}$ and duration $\Delta \mathrm{t}_{\mathrm{OOR,tot}}$ are analysed. Figure 4.7 illustrates this total operational cost, $\Delta \mathrm{v}_{\mathrm{OOR,tot}}$, plotted on the y-axis as a function of the numbers of servicers on the x-axis. Each line represents a different depot location. The function plot suggest that $\Delta \mathrm{v}_{\mathrm{OOR,tot}}$ increases as the number of servicing vehicles rises. The variation in refuelling operation costs between depot placements is less pronounced when the number

of servicers is small, but becomes more significant as the fleet size grows. The relative difference in costs between the most optimal and least optimal depot locations amounts to approximately 300 m/s. In contrast, for the O2O scenario, the discrepancy increases to nearly 1 100 m/s. This suggests that the depot orbit's influence on OOS mission design becomes more critical as the ratio of servicers to clients increases. With fewer servicers, the routes tend to cover a broader range of Ω locations, rendering the depot's specific position along the GEO orbit less impactful on the overall cost. Conversely, as the number of servicers increases, the relative phasing between the depot and individual clients gains in importance, as these phase differences translate directly into increased costs. This finding is relevant regardless of the clients in question. However, the magnitude of this effect may vary depending on the specific use case. In this use case, depot orbits within the range of −30° to 30° show the best cost efficiency and necessitate further refinement. The depot orbit at Ω = 0° exhibits the lowest overall cost, leading to a more detailed investigation of the optimal number of servicing vehicles for that specific depot location.

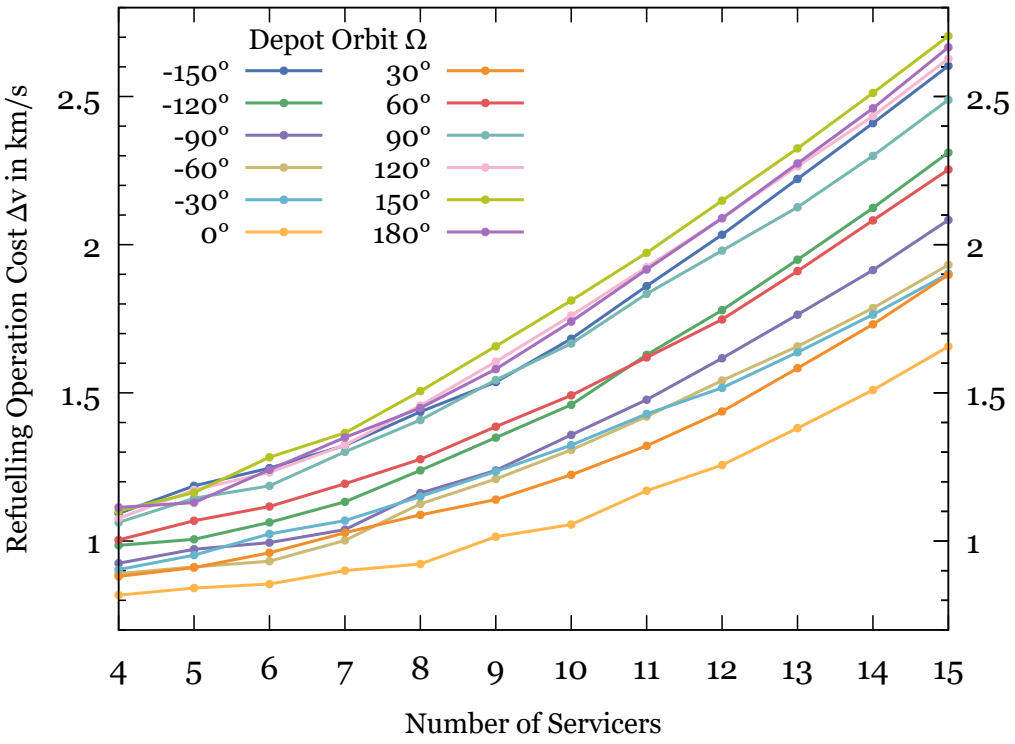

Figure 4.7.: Refuelling Operation Cost $\Delta v_{OOR,tot}$ of OOR Architecture Designs

A more detailed analysis of the routes reveals that, initially, with four servicers, the optimal configuration consists of one long, one medium-length, and two shorter routes as depicted in figure 4.5. As the number of servicers increases, shorter routes are preferentially subdivided first, as figure 4.8 suggests, comparing routes for 8 and 12 servicers.

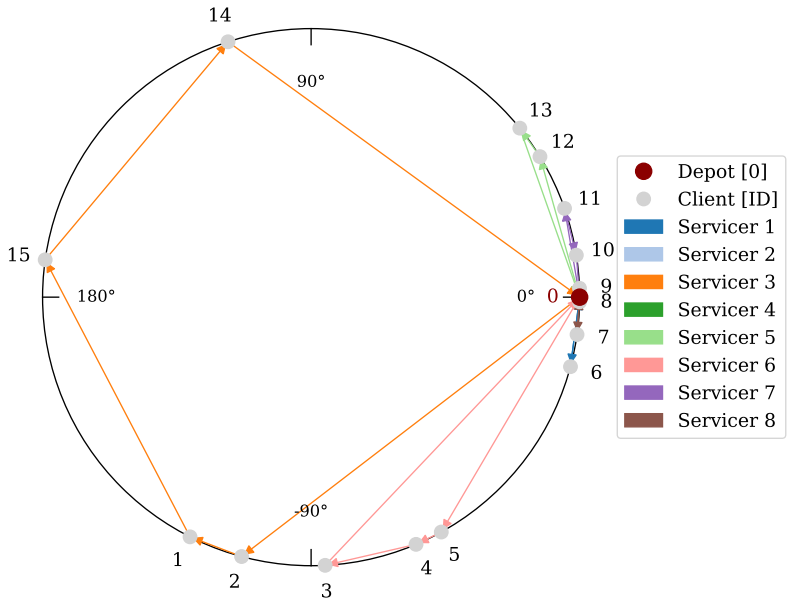

(a) Routes of 8 Servicers

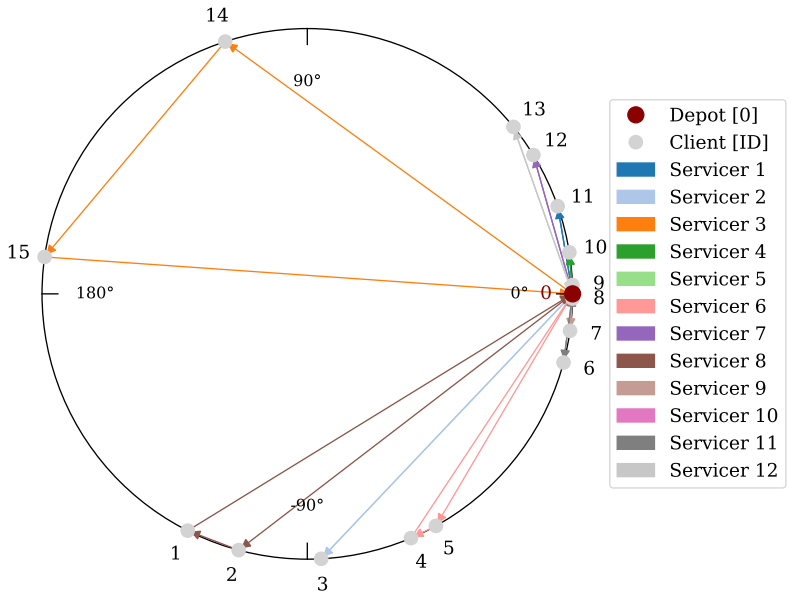

(b) Routes of 12 Servicers

Figure 4.8.: Change of Servicing Routes with Increasing Fleet Size for $\Omega = 0°$

The corresponding changes in the matrix entries in figure 4.9 indicate the reason for this behaviour. The next most cost-effective depot connection routes are selected, and subsequently complemented by routes drawn from the interior matrix entries to complete logistical constraints. Only when the number of servicing spacecraft reaches 9, does the long route become subdivided into shorter segments. At this point, none of the individual routes exceeds 180° degrees in terms of phase difference. As the number of servicing

spacecraft engaged in refuelling increases, the influence of depot locations on the overall route configuration becomes more pronounced, as fewer options remain for optimizing the combination of routes between clients.

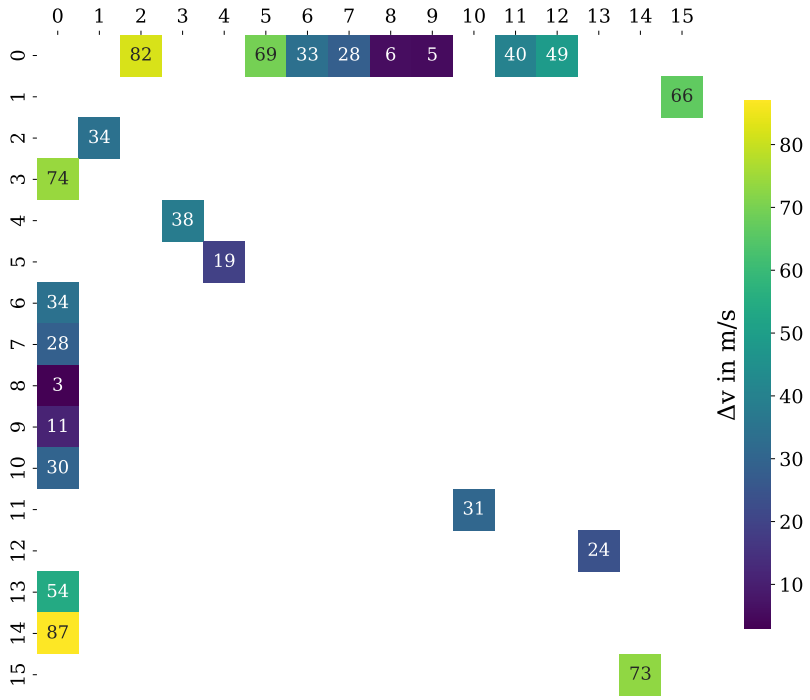

(a) Selected Route Costs for 8 Servicers

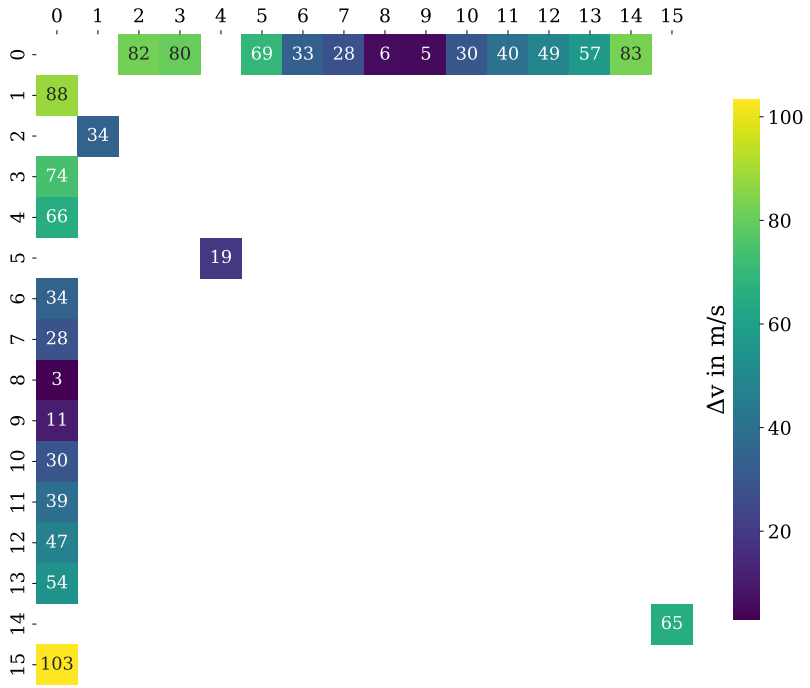

(b) Selected Route Costs for 12 Servicers

Figure 4.9.: Change of Servicing Route Costs with Increasing Fleet Size for $\Omega = 0°$

The total duration of the refuelling operations, $\Delta t_{OOR,tot}$, is shown in figure 4.10. This figure presents trends across varying numbers of servicers on the x-axis, with distinct lines representing different depot locations. The duration consistently decreases towards the O2O scenario, which exhibits a significantly shorter duration by approximately ten days compared to the case with the minimum number of servicers. While the cost graphs in figure 4.7 show continuous trends based on both depot orbits and the number of servicing vehicles, the duration performance demonstrates relatively large fluctuations depending on the depot orbit. This can be attributed to the fact that the total duration is not determined by the sum of all refuelling route durations, but by the maximum duration of all individual routes, as the servicers execute their manoeuvres in parallel. The optimal routing solution identified by the genetic algorithm prioritizes minimizing total route costs, which can result in longer individual route durations.

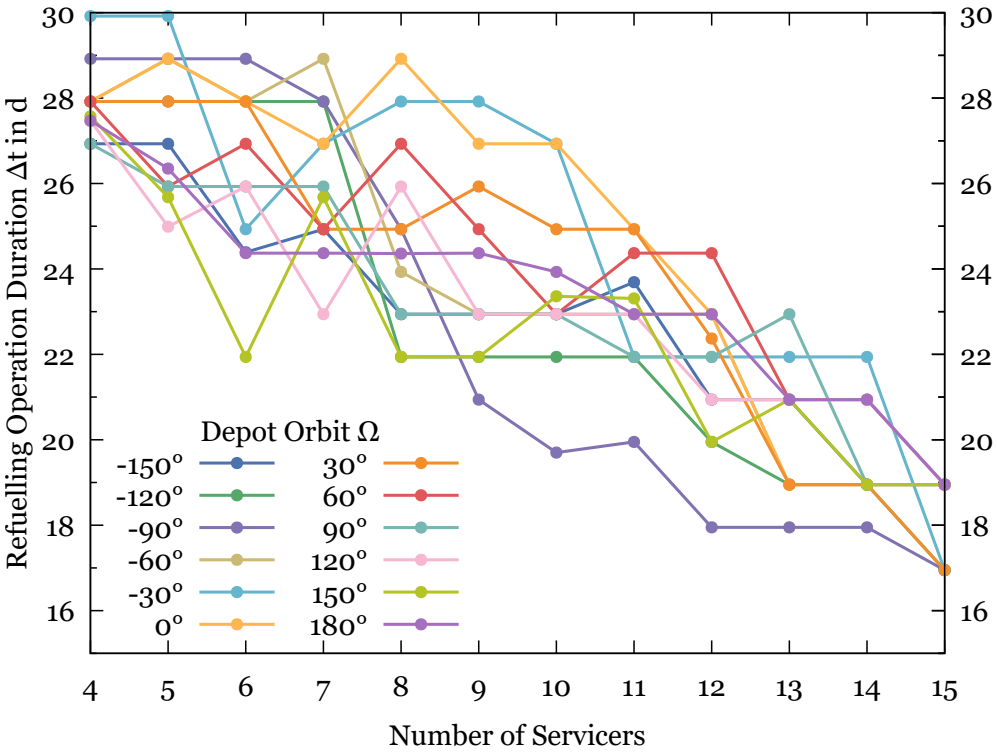

Figure 4.10.: Refuelling Operation Duration $\Delta t_{OOR,tot}$ of OOR Architecture Designs

Overall mission performance, in terms of total cost and duration across varying numbers of servicers on the x-axis, is depicted in figure 4.11. Illustration 4.11b presents plots of $\Delta v_{OOR,tot}$ on the left y-axis and $\Delta t_{OOR,tot}$ on the right y-axis for the fixed depot orbit parameter $\Omega = 0°$, as shown in figures 4.7 and 4.10, respectively. Figure 4.11a indicates the total mission cost, Δv_{tot}, and total mission duration, Δt_{tot}. This total cost includes

primarily the deployment of the servicer infrastructure composed of the GEO insertion costs of all servicers, along with predefined costs and durations for close approach and proximity manoeuvres, in addition to the refuelling operations.

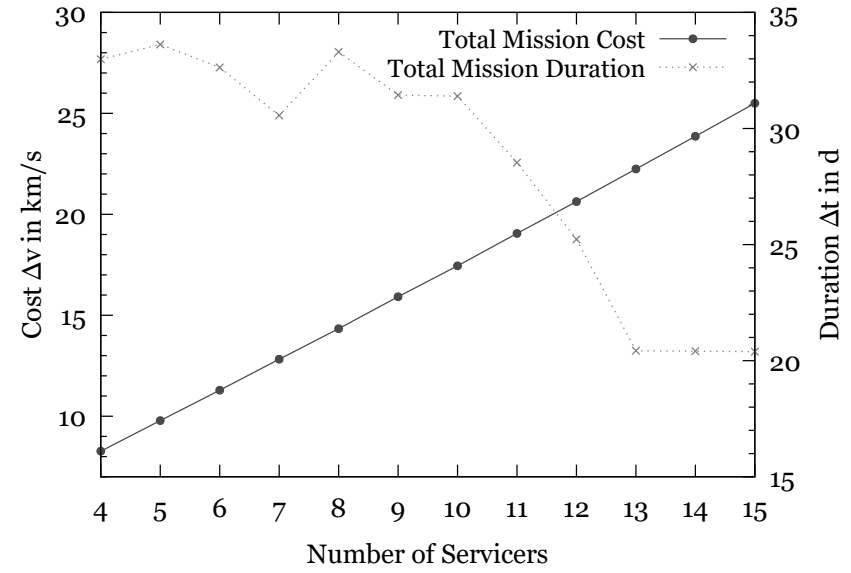

(a) Overall Mission Δv_{tot} and Δt_{tot}

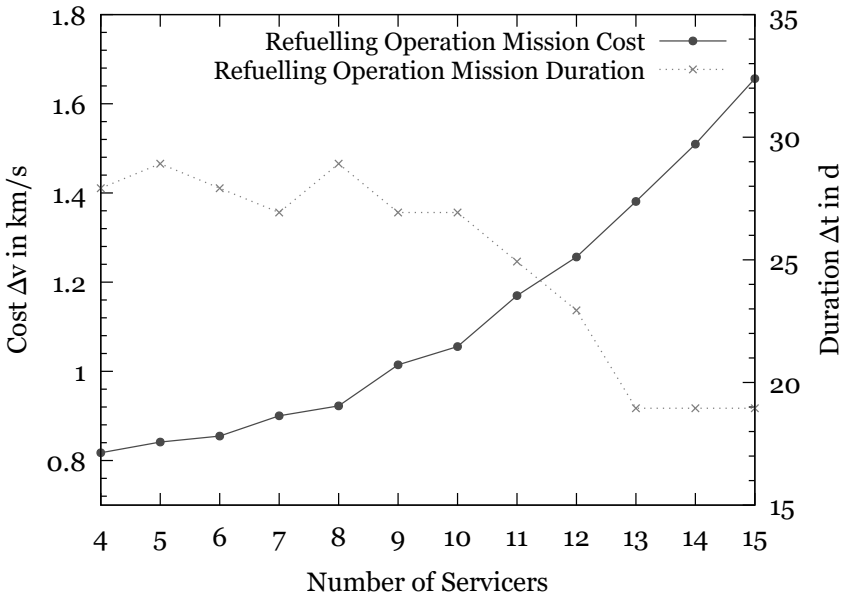

(b) OOR Operation $\Delta v_{OOR,tot}$ and $\Delta t_{OOR,tot}$

Figure 4.11.: Mission Performance: Total Cost and Duration for $\Omega = 0°$

The total mission cost, Δv_{tot}, exhibits a linear increase with the number of servicing vehicles. The costs associated with close approach, proximity manoeuvres, and docking contribute only a constant addition to each design point, as they depend solely on the

number of clients being serviced. Due to the significantly higher magnitude of insertion costs into GEO, which is applied per servicing vehicle, the route costs are effectively smoothened, resulting in a linear relationship. The total mission duration, Δt_{tot}, follows the trend observed in $\Delta t_{OOR,tot}$, driven primarily by the long phasing manoeuvres that dominate overall mission duration. The difference in mission duration between both graphs is also attributed to the additional time required for close approach, proximity manoeuvres, and docking. The total duration is related to the servicer with the longest operational timeline. For scenarios involving a lower number of servicers, the effect in time increase is more pronounced, with a difference of around four days, as each spacecraft is responsible for servicing more clients. In contrast, for the O2O scenario, the duration difference is reduced to just one day, as each servicer handles only a single client.

To gain a deeper understanding of total mission performance evolution, individual servicer route cost and duration statistics are analysed for different servicer fleet sizes. Figure 4.12 presents the mean cost (4.12a) and duration (4.12b) μ of a servicer route within the architecture. The minimum and maximum values correspond to the cost and duration for the least and most demanding servicer routes among the entire fleet. The standard variation σ indicates the variability within the servicer fleet regarding individual costs and operation durations. The mean servicer cost reaches its highest values for fleets consisting of four servicers, despite these configurations having the lowest total OOR cost. The lowest mean servicer costs are observed for fleets of eleven servicers, with a slight increase as the number of servicers rises beyond this range. Employing more than eleven servicers is neither beneficial for total mission cost nor for individual servicer costs. This is attributed to increasing route costs when fewer clients are assigned to each route. These tendencies suggest that reducing mission duration may be more effectively achieved by adjusting the priority parameter for maximum phasing duration, rather than by increasing the number of servicers beyond eleven. Although the objective is to minimize total mission cost, this leads to the highest individual route costs, which necessitates sizing the servicers accordingly. The increased individual route costs directly translate to higher propellant mass requirements for each transfer, as indicated by the Tsiolkovsky equation, potentially implying an increase in the required dry mass. When the servicer design is identical across all vehicles, the system must be sized based on the most demanding route. Interestingly, while the maximum route cost decreases with an increasing number of servicers, the minimum route cost remains constant starting at five servicers, since one specific route remains unchanged and consistently represents the lowest cost. Furthermore, the figure highlights that the lowest standard deviation is achieved with the maximum number of

servicers, as route costs become more homogeneous, making equivalent servicer design more viable.

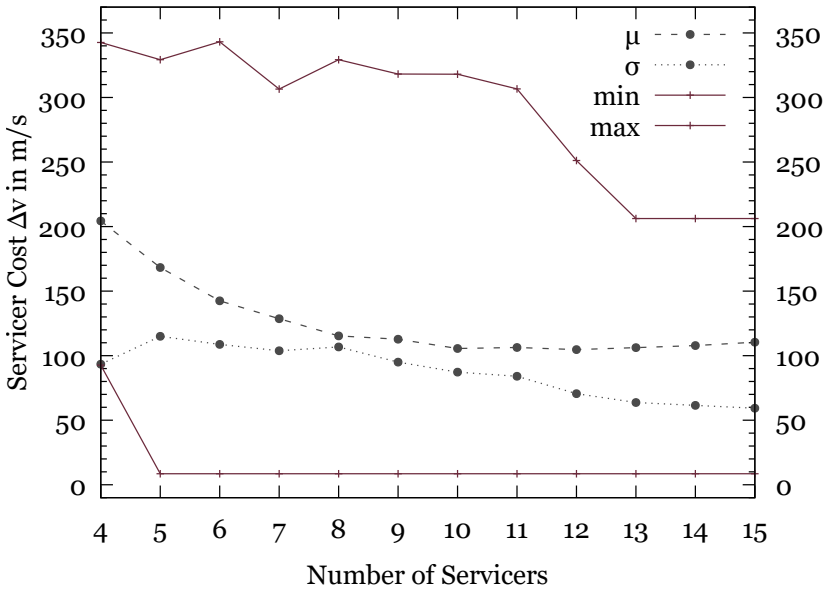

(a) OOR Operation $\Delta v_{OOR,tot}$

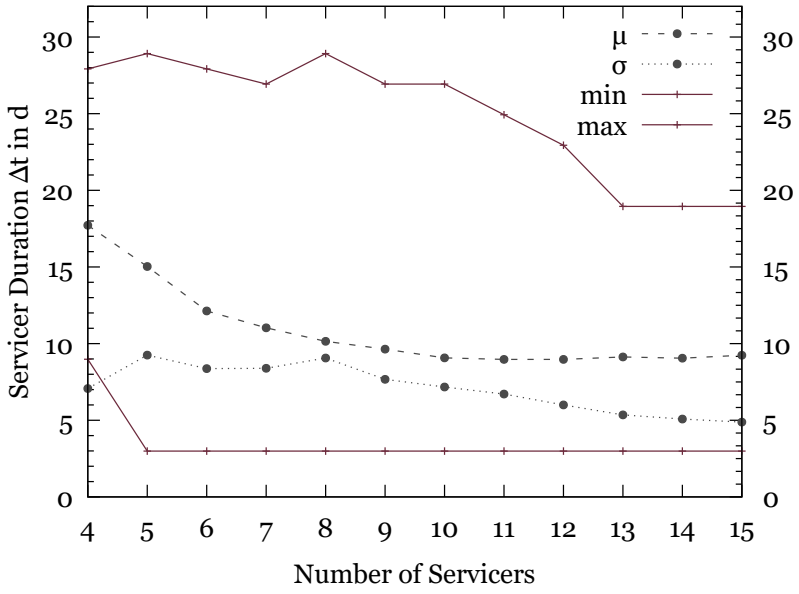

(b) OOR Operation $\Delta t_{OOR,tot}$

Figure 4.12.: Servicer Statistics for Refuelling Operation Cost and Duration for $\Omega = 0°$

This evolution of route costs reflects a shift towards greater uniformity in performance as the fleet size increases beyond eight servicers. For 5-8 servicers the routes are even more imbalanced than for 4 servicers as more short routes are generated at the expense of intermediary ones. Due to the previously discussed effects of $p_{\Delta v/\Delta t} = 0.1$ on the Δv

and Δt matrices in section 4.1.1, routes with higher Δv values also tend to have longer durations. Consequently, both graphs 4.12a and 4.12b exhibit similar trends.

As illustrated in figure 4.13, the total residual propellant mass, $\Delta m_{res,tot}$, across all servicers exhibits a linear increase with the number of servicers. This trend corresponds to the linear growth in total payload residual propellant available to client refuelling. Since each servicer has an equivalent payload capacity for payload propellant, and all clients are serviced regardless of the number of servicers, the linear increase is solely a result of the uniform tank capacities used for refuelling.

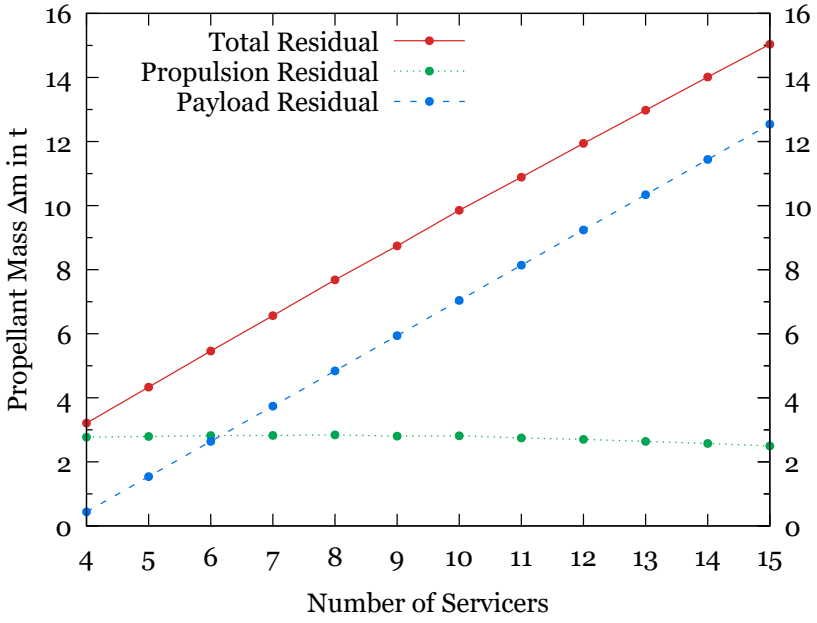

Figure 4.13.: Overall Mission Residual Propellant Mass for $\Omega = 0°$

In contrast, the total residual propellant mass in propulsion tanks, available for manoeuvres, remains nearly constant, with only a slight decrease as the servicer fleet grows. After GEO insertion, each servicer has a low initial propellant mass, replenished by uniformly distributed depot fuel of 3.1 t. For instance, with four servicers, each receives 775 kg of propellant, while in the O2O scenario, only 210 kg is allocated per servicer, reducing their manoeuvring mass by 400 kg. This, along with the lower Δv requirements per servicer from figure 4.12a, suggests that fuel consumption per servicer decreases. However, the increased total operational cost for the routes $\Delta v_{OOR,tot}$, shown in figure 4.11b, more significantly impacts the total residual propulsion propellant mass, underlining the importance of overall system optimization.

The number of servicers is critical for OOR mission feasibility, with the residual mass distribution of each servicer as a key factor. If any servicer exhibits a negative residual mass, the architectural design is infeasible. Figure 4.14 presents the statistics for propellant mass allocated per servicer.

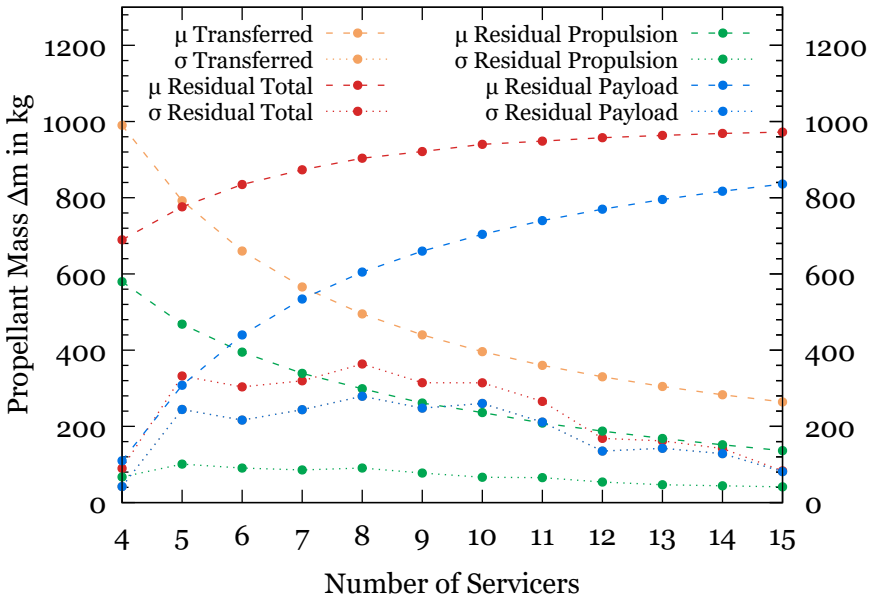

(a) Constitution and Distribution

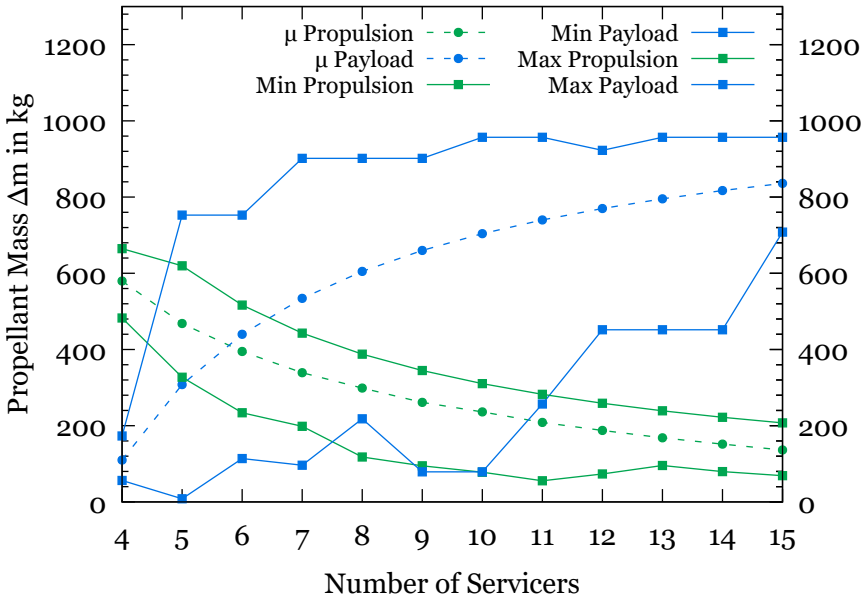

(b) Extreme Values

Figure 4.14.: Servicer Statistics for Residual Propellant for $\Omega = 0°$

Figure 4.14a displays the mean μ and standard deviation σ of total residual propellant per servicer and the propellant mass transferred from servicers to clients across varying numbers of servicers. Additionally, the plots show the breakdown of total propellant into payload and propulsion system components, highlighting their trends as fleet size increases. Figure 4.14b shows the minimum, maximum, and mean remaining propellant mass in both the payload and propulsion tanks per servicer, illustrating the variation across the servicer fleet as the number of servicers increases.

Complementary behaviour of remaining payload mass and transferred mass is evident, as, by definition, clients are refuelled exclusively with payload propellant. In a larger fleet, each servicer transfers less fuel. As the tanks were designed for the conservative case, the remaining payload propellant increases with the fleet size. Particularly relevant for feasibility is the remaining amount of propulsion fuel, which decreases on average as the number of servicers increases. However, as previously explained, the reduction is primarily due to the fact that less fuel was available to each servicer, as the depot fuel is distributed across the fleet in the defined scenario as explained previously. Thus, this does not provide insight into the fuel consumption along the routes. Since the mass available to each servicer remains constant across all scenarios, the cost graph per servicer 4.12a is more informative, revealing a minimum. Additionally, the standard deviation of the remaining fuel mass decreases with an increasing number of servicers. This suggests that with a larger fleet, the routes become more balanced, which is also reflected in the reduced variation in route costs.

The spacecraft design parameters were selected to ensure feasibility across all scenarios. In this case, for the cost-efficient depot location, 20-40 kg of propellant remain in the servicers at the end of the mission, in the two extreme cases as seen in figure 4.14b. For the smallest number of servicers, this concerns the remaining payload propellant, while for the largest fleet, it reflects the remaining propulsion propellant. For other depot Ω, these values can drop below 10 kg. For both four and fifteen servicers, minimum and maximum remaining payload mass are relatively close. While the maximum remains fairly constant, the minimum increases as the number of servicers grows. This observation, consistent with previous conclusions, suggests that routes with lower costs are maintained even as the number of servicers increases, and the remaining servicers handle fewer clients. The capacity of the servicers currently limits refuelling to a maximum of four clients. Increasing this capacity would provide additional flexibility in the optimization process and could further reduce overall mission costs.

4.2.2. Depot Orbit

As the relative phase difference between the servicer and client is the primary driver of route costs, minimizing $\Delta v_{OOR,tot}$ is largely focused on reducing phasing angles. Figure 4.15 demonstrates that varying the number of servicers leads to similar tendencies regarding the most efficient depot location. It plots $\Delta v_{OOR,tot}$ against the depot orbit RAAN, with different lines representing the various numbers of servicers. The functional behaviour exhibits a periodic pattern, with a minimum occurring within the range of $-30°$ to $30°$, while a RAAN of $150°$ results in the highest costs. Depot orbits with RAAN between $-30°$ and $30°$ warrant further refinement. Since eight European client satellites are clustered at longitudes above Europe, these depot locations exhibit lower phase differences relative to the clients, allowing for less fuel-intensive phasing manoeuvres. As previously observed, the graph highlights that the differences between depot locations become more pronounced as the fleet size increases. Specifically, for fleets of four to six servicers, the cost differences across depot locations are not as distinct. Notably, at $0°$ and $30°$, all three infrastructure configurations show very similar costs, with minimal variation between them. The choice of servicer numbers can result in differences of up to 1 600 m/s in the case of $\Omega = 150°$, while for $\Omega = 0°$, the maximum difference is 900 m/s. Thus, in absolute difference, the impact of the number of servicers is higher on $v_{OOR,tot}$ than Ω.

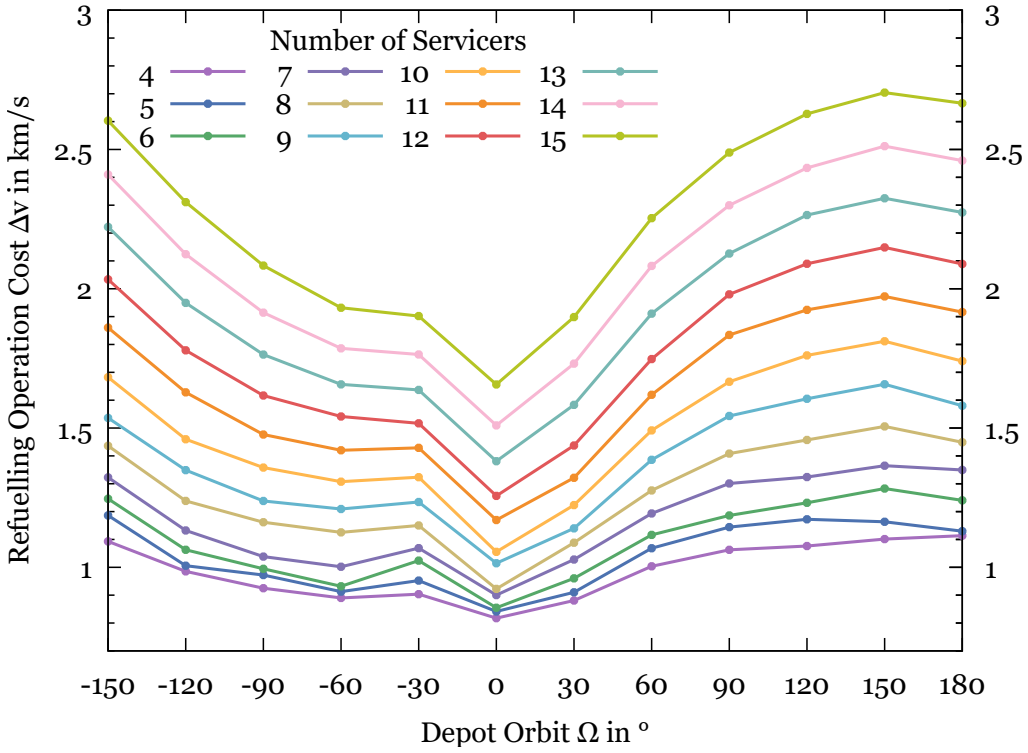

Figure 4.15.: Refuelling Operation Cost $\Delta v_{OOR,tot}(\Omega)$ of OOR Architecture Designs

For all choices of depot locations, the O2O scenario results in the fastest refuelling operation, as shown in figure 4.16, followed by the configuration with 14 servicers, as previously noted. There are no consistent patterns across different depot orbits that can be generalized for all numbers of servicers. This is because the total mission duration is dictated by the longest servicer route within each architecture, while only the cost is optimized for route selection. For a fleet of eight servicers, the variation in mission duration due to the choice of depot orbit is most pronounced, with differences reaching up to seven days. In contrast, with 15 servicers, the fluctuations in duration along the RAAN are minimal, limited to just two days. Consequently, depending on the fleet size, the temporal impact of the depot orbit selection becomes more or less significant.

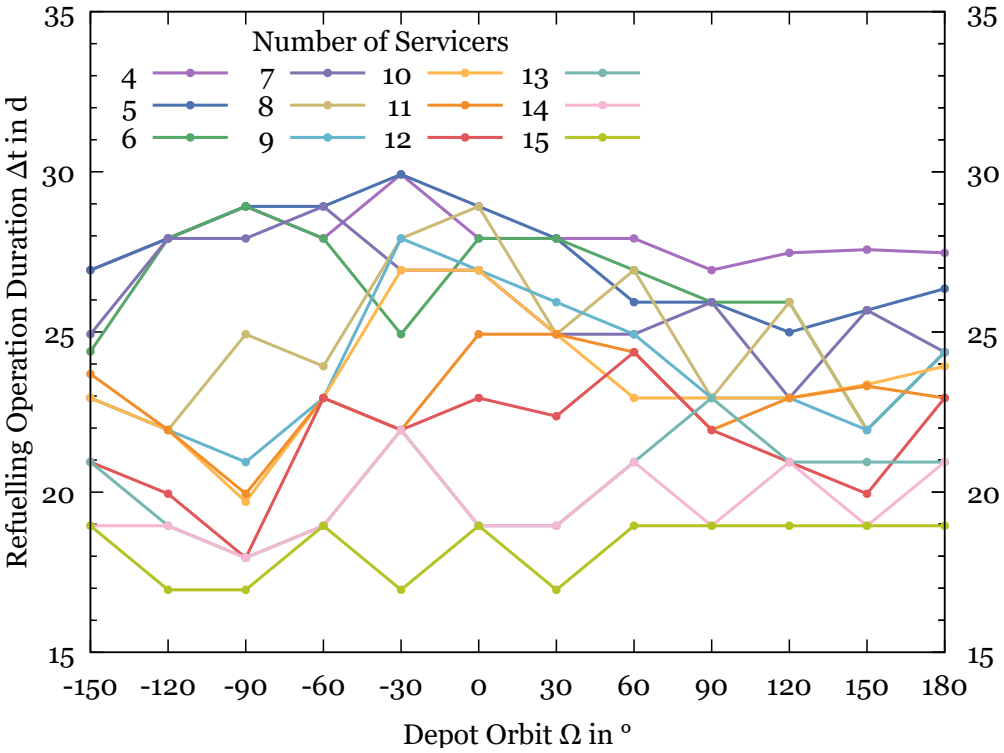

Figure 4.16.: Refuelling Operation Duration $\Delta t_{OOR,tot}(\Omega)$ of OOR Architecture Designs

As with fleet size in figure 4.11, the case of minimal total cost, involving four servicers, is examined in more detail here. Total mission cost and duration mirror the peaks observed in OOR costs and durations in figure 4.17. It confirms the advantage of the depot location around $\Omega = 0°$, offering a substantially lower cost, with a duration only one day longer than the duration-optimal location. The architecture's launch cost from GTO to GEO includes simultaneous circularization and out-of-plane manoeuvres to reach zero inclination. The RAAN change required at insertion, which depends on depot location, does not impact overall trends, as the single-thrust manoeuvre is dominated by altitude and

inclination changes, which remain constant across all depot locations. Since all clients are visited regardless of the depot's orbit, proximity manoeuvres add uniform cost increments across all depot orbits, resulting in a consistent increase in both cost and duration.

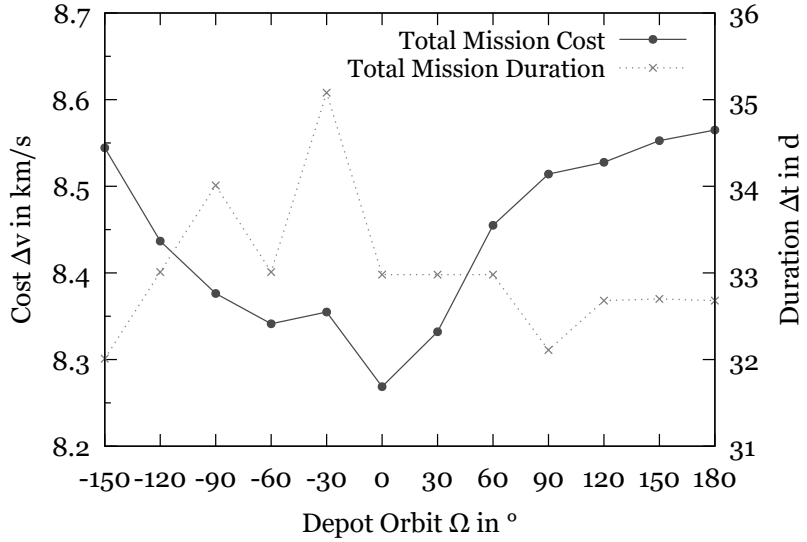

(a) Overall Mission Δv_{tot} and Δt_{tot}

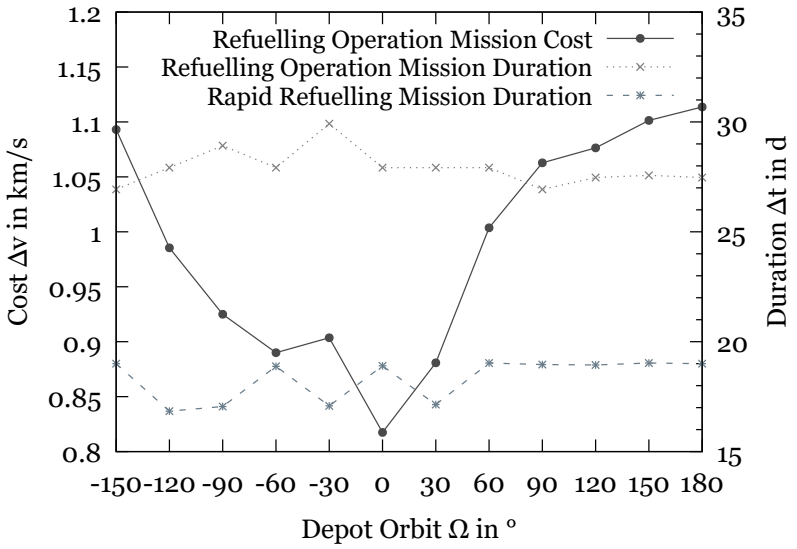

(b) OOR Operation $\Delta v_{OOR,tot}$ and $\Delta t_{OOR,tot}$

Figure 4.17.: Mission Performance: Total Cost and Duration for 4 Servicers

In contrast to servicer fleet size selection, the depot orbit choice does not significantly influence the trend of average cost per servicer in figure 4.18 relative to $v_{OOR,tot}$ in figure 4.17b. Although total costs are minimal for depot orbits within the range of $\Omega = -30°$

to 30°, the deviations in mean servicer costs remain notably higher. This suggests that some servicers handle multiple clients, while others follow shorter routes, as seen in the servicer route distribution as in figure 4.5. Specifically, two servicers manage clients near the depot, while the other two service clients along more expensive routes. Although these routes may minimize total mission cost, it would necessitate different mass configurations for the servicers to adapt to their respective routes. As a result, this leads to significant variations in propellant consumption, causing high standard deviations in residual propulsion propellant mass, as shown in figure 4.20. For depot orbits with smaller differences between servicer routes, such as at $\Omega = 150°$, all four routes have roughly equal costs and are not split into notably short or long routes.

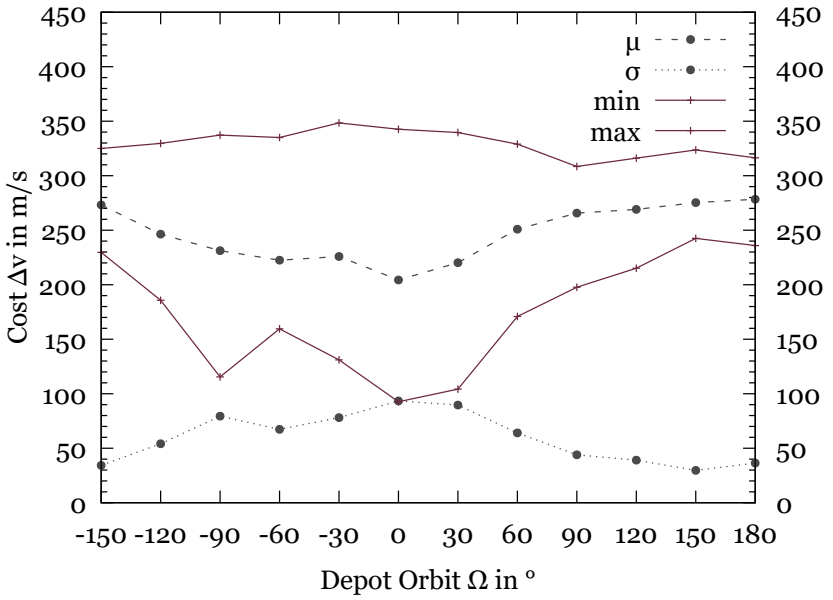

Figure 4.18.: Servicer Statistics for Refuelling Operation Cost $\Delta v_{OOR,tot}$ for 4 Servicers

Figure 4.19 supports this reasoning. The routes depicted in 4.19b show that, at $\Omega = -150°$, three out of the four routes encompass relatively high phase differences, whereas at $\Omega = 60°$ in figure 4.19a, there are only two extended routes. As previously shown for $\Omega = 0°$, only one route is particularly long. As the number of servicers increases, figures 4.19c and 4.19d demonstrate that longer routes are progressively shortened, as fewer clients are serviced per route. Concurrently, shorter routes closer to the depot which are less costly for depot transfer handle an increasing number of return trips to the depot.

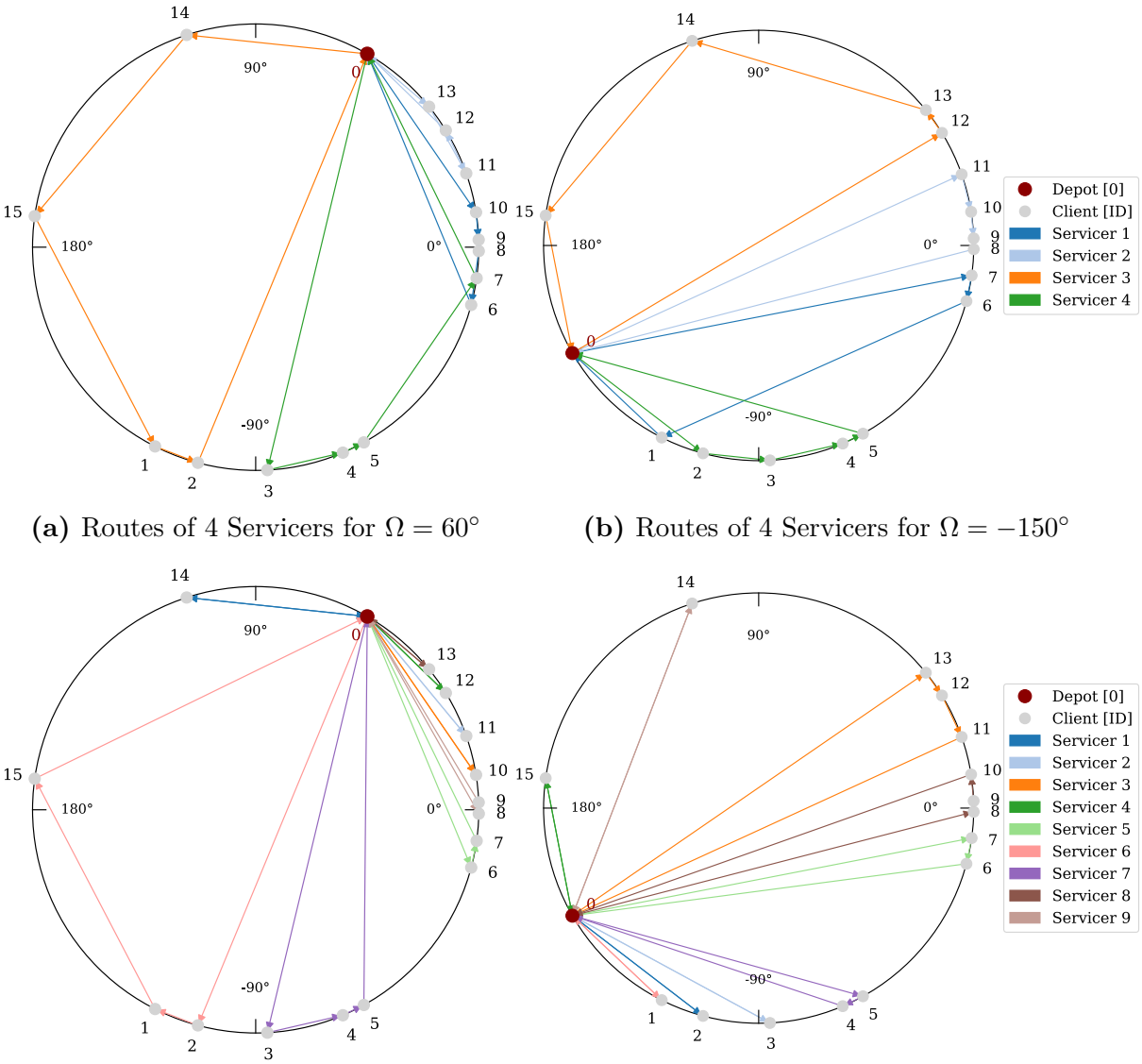

(a) Routes of 4 Servicers for $\Omega = 60°$

(b) Routes of 4 Servicers for $\Omega = -150°$

(c) Routes of 9 Servicers for $\Omega = 60°$

(d) Routes of 9 Servicers for $\Omega = -150°$

Figure 4.19.: Change of Servicing Routes with Depot Orbit Ω

The impact of depot placement on total residual propellant mass is less significant than that of fleet size. As illustrated in figure A.21, total residual propellant mass is mainly influenced by the remaining fuel in propulsion tanks, while the remaining payload mass is fixed by the constant total client demand for a given number of servicers. To gain a deeper insight, figure 4.20 shows the impact of depot Ω on the propellant characteristics per servicer. The consumed propellant mass serves as an indicator of the fuel efficiency of the servicer routes. At $\Omega = 0°$, the most fuel remains in terms of mean mass per servicer μ, as the optimized routes exhibit the lowest $\Delta v_{OOR,tot}$.

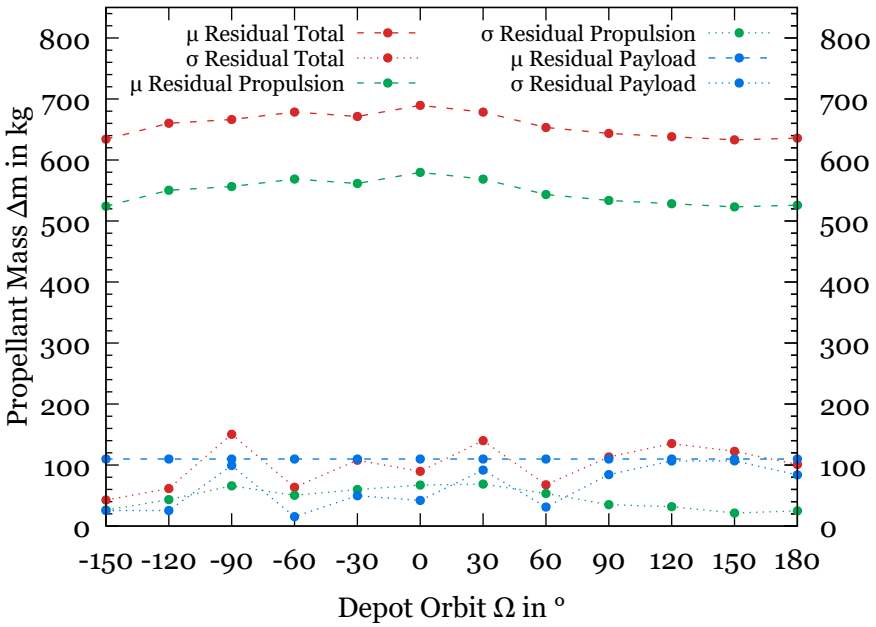

(a) Constitution and Distribution

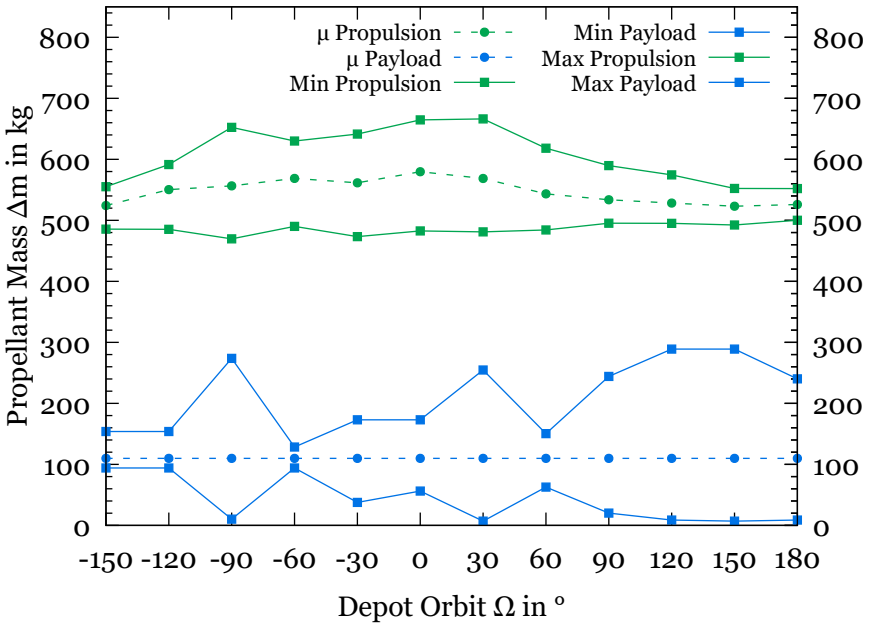

(b) Extreme Values

Figure 4.20.: Servicer Statistics for Residual Propellant for 4 Servicers

Figure 4.20b indicates that, at various locations, the residual payload propellant mass in one servicer is as low as 8 kg, while another servicer retains a significantly higher residual payload mass of nearly 300 kg. The standard deviation σ, as depicted in plot 4.20a, highlights these high discrepancies between the minimum and maximum remaining fuel mass among servicers in the fleet. The residual payload propellant mass σ is

highly dependent on the visited clients varying in fuel demand. In cases where greater deviations in residual mass are observed, the differences in number of visited clients or total propellant demand between the servicer routes are correspondingly larger.

The KPI for rapid refuelling, $\Delta t_{OOR,rapid}$, is solely dependent on the depot location, as it is defined by the duration of the longest transfer in the O2O scenario. Figure 4.21a thus plots $\Delta t_{OOR,rapid}$ against various depot placements in terms of Ω on the x-axis.

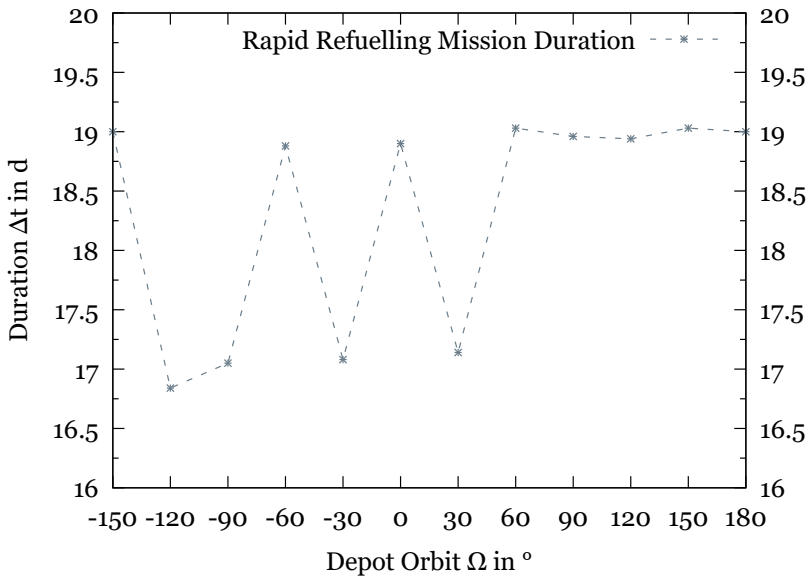

(a) Rapid Refuelling Duration $\Delta t_{OOR,rapid}(\Omega)$

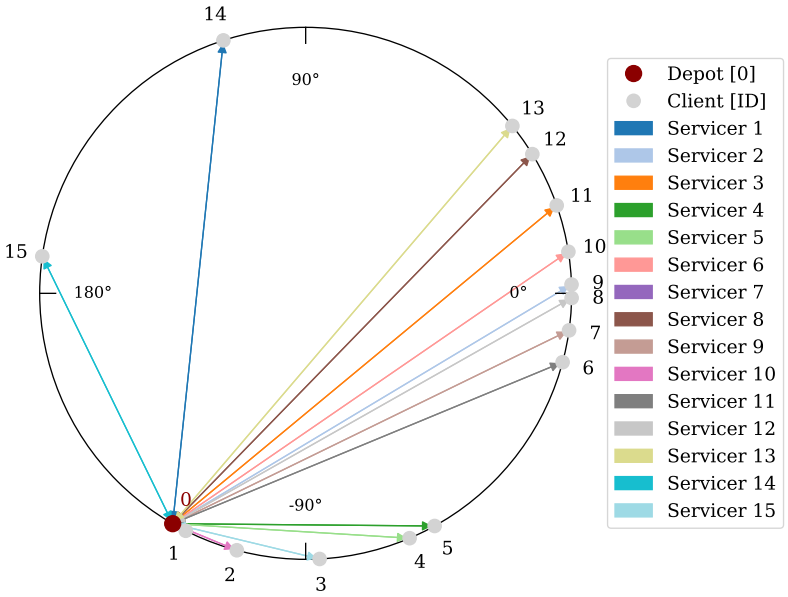

(b) Routes of 15 Servicers for $\Omega = -120°$

Figure 4.21.: Rapid Refuelling Performance $\Delta t_{OOR,rapid}$

$\Omega = -120°$ is the most favourable compared to other depot orbits with 16.75 days. The corresponding routes for direct servicing from the depot are depicted in figure 4.21b. In the discrete phasing solutions, faster routes can be identified for similar costs, particularly for clients with the maximum phase difference. Comparing depot locations with lower costs, it is observed that depot orbits at $-30°$ and $30°$ offer an advantage in rapid refuelling over $0°$. Interestingly, the values for depot orbits between $60°$ and $180°$ exhibit minimal variation, stabilizing around 19 days. Refinement of the depot locations to the range of $-30°$ to $30°$ yields the performance results shown in figure A.22. In the next iteration, the range of $\Omega = -10°$ to $10°$ is investigated. A.23 provides the results within this interval. The refined $\Delta v_{OOR,tot}$ plots are closely aligned, yet they still allow for the identification of the interval $\Omega = -5°$ to $5°$ as a region for further refinement using a step size of only one degree, with the results shown in figure 4.22 and A.24. The successive steps reveal that not only do the cost curves for different fleet sizes converge, but also the cost plots for the depot's RAAN range approach a near-constant line. The graphs therefore underline that $\Delta v_{OOR,tot}$ is converging.

$\Omega = 2°$ emerges as the most promising depot orbit for most fleet sizes, the design point of four servicers among them. A computation of the mean RAAN position based on client orbit phase differences yields a value of $-5.3°$. The obtained results show a deviation from that value due to consideration of transfer durations as well as slightly inclined orbits. To ensure that the small differences in solutions across most servicer numbers are not introduced by randomness in the solution algorithm, but rather represent the optimal depot locations based on servicer count, the population of the genetic algorithm was expanded. The results illustrated in figure A.25 confirm the choice of depot location. For a fleet of four servicers, the lowest overall $\Delta v_{OOR,tot}$ is achieved at a depot location with $\Omega = 2°$, making this the most ideal design point in terms of overall cost in this investigation. At the optimal design point, the KPIs given in table 4.2 reflect a total mission duration of 33 days, with nominal refuelling operation incurring a cost of 810 m/s.

Table 4.2.: KPIs for Optimal Design Point Depot Location $\Omega = 2°$ with 4 Servicers

KPI	Value
Overall Mission Cost Δv_{tot}	8 261 m/s
Nominal Refuelling Cost $\Delta v_{OOR,tot}$	810 m/s
Total Mission Duration Δt_{tot}	33 d
Nominal Refuelling Duration $\Delta t_{OOR,tot}$	28 d
Rapid Refuelling Duration $\Delta t_{OOR,rapid}$	19 d

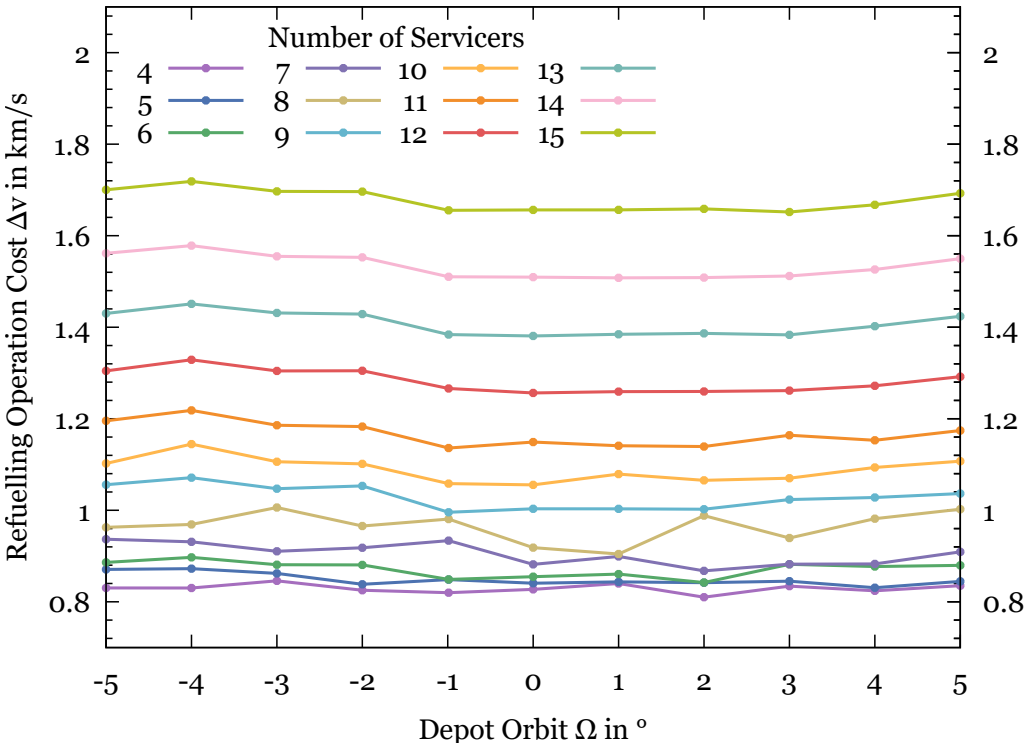

(a) $\Delta v_{OOR,tot}$

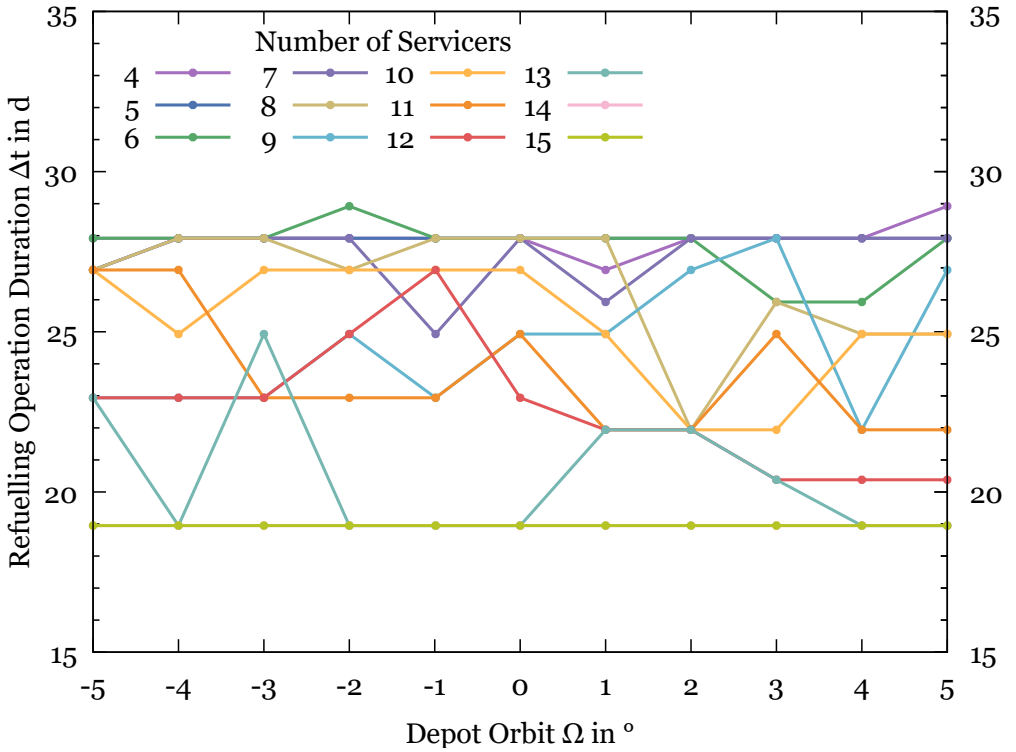

(b) $\Delta t_{OOR,tot}$

Figure 4.22.: Refuelling Operation Cost and Duration for Refined Depot $\Omega \in [-5°, 5°]$

4.3. Discussion

The findings of this study demonstrate a clear advantage in using smaller servicing fleets with higher payload capacity, when the objective is to optimize and evaluate total refuelling operation cost. Such an architecture design represents the longest-duration option and may therefore be unsuitable for cryogenic propellants, where boil-off is a critical factor, necessitating faster transfer routes to minimize propellant loss. While it might initially appear that deploying a single servicer would be the ideal solution for minimizing overall mission costs, and would eliminate the need for route optimization, this approach presents significant limitations. Designing a spacecraft with such a large payload capacity would inevitably lead to increased fuel consumption, which, in turn, would require a greater launch mass. This would render the overall approach suboptimal from both logistical and economic perspectives. Additionally, the analysis reveals that the average servicer cost is minimized when the number of servicers is neither at the minimum nor the maximum, but rather at an intermediate fleet size. This configuration leads to more balanced routes, which is particularly beneficial for propellant consumption when the servicers are uniformly sized. Smaller servicers would consume less fuel, reducing the total mass that needs to be launched into space. The study can be interpreted as a scenario where a single servicer refuels multiple clients over several routes, while being resupplied at the depot. In this case, the route optimization process becomes crucial for mission planning, whether one or multiple servicers are deployed. However, the mission duration would need to be reassessed in the case of fewer servicers being resupplied, as the total duration would then become the sum of all route durations, rather than being limited by the longest route. Consequently, the overall mission duration would increase substantially. An architecture that balances lower average servicer costs and more evenly distributed routes, adjusted to the appropriate spacecraft sizing, could result in a significant reduction in the total launch mass. Such a system could strike a compromise between maximum mission duration and the number of servicers deployed for the routes. To determine an overall optimal system design including spacecraft sizing and mission planning, the optimization objective would need to be refined. A multi-objective minimization strategy should be employed, taking into account not only refuelling operation cost in terms of Δv, but also directly launch mass, propellant mass consumption, and mission duration, while treating servicer design as a key design variable. This approach would allow for a more holistic assessment, ultimately leading to a more sustainable and efficient mission architecture for On-Orbit Refuelling.

The design methodology presented in this study introduces certain limitations in the application of the developed strategies and the accuracy of the results obtained. The trade-off parameter $p_{\Delta v/\Delta t} = 0.1$ enables adaptive optimization, where the balance between Δv and Δt is dynamically adjusted based on external mission priorities. This provides flexibility according to mission context and client demands. While individual client requirements for refuelling times could be critical in a real mission, they were not accounted for in this analysis. In actual mission planning, external factors, such as satellite operational schedules, client servicing windows, and communication constraints, might impose additional limitations that were not incorporated here. Adjusting $p_{\Delta v/\Delta t} = 0.1$, along with decreasing the maximum allowed time of flight, would yield shorter mission timelines, although the methodology would still inherently optimize for cost, even if it is a lower priority when $p_{\Delta v/\Delta t} > 0.5$. In such cases, switching to a pure minimization of total mission duration could improve overall time performance. For intermediate parameter values, a multi-objective optimization that accounts for both time and cost could yield more valuable results, balancing the competing objectives effectively.

The genetic algorithm allows for optimization of both, servicer fleet size and depot placement, identifying an optimal depot orbit RAAN value within a range of approximately $+/-1°$. A comparison between figure 4.22a, which displays ultimately refined depot locations and the corresponding high-population results in figure A.25b allow for identification of that range. However, the remaining inherent randomness of GA-based solutions is accepted due to otherwise exceedingly high computational cost. The individual optimal cost for each design point, when resolved to $1°$ precision, carries an uncertainty of around $10 - 20\,\mathrm{m/s}$ in total cost for smaller fleets. Uncertainty is highest for lower servicer numbers as the problem complexity is higher. In the unlikely case of premature convergence, which occurs only once in 165 data points within the refined interval, deviation in total cost reaches at most $50\,\mathrm{m/s}$. This level of uncertainty may slightly alter the relative prioritization of design points, necessitating careful interpretation of the results.

Furthermore, the logistics optimization methodology is based on a geosynchronous case and does not incorporate the relative motion of client satellites within their actual orbits. A time-dependent logistics optimization approach, although far more complex, would enable the application of this design methodology to more general orbital environments, including LEO servicing missions. Additionally, this would allow exploration of depot orbits at higher or lower altitudes, potentially reducing servicing costs by eliminating phase differences without the need for extensive manoeuvring.

In limit cases of heterogeneous fuel demand, the optimization of the CVRP may not represent the most fuel-efficient solution. For instance, visiting a high-demand client first reduces the mass of the servicer for subsequent transfers, which could lower fuel consumption. This highlights the necessity for incorporating multi-objective optimization strategies that account for servicer sizing as a design variable, alongside the conventional objectives of cost and time.

4.4. Design Recommendations

The findings of this study can be synthesised into design recommendations for On-Orbit Servicing infrastructure, encompassing not only the technical aspects of the infrastructure design but also the methodological approaches used in its optimisation and implementation. These recommendations provide a holistic framework for guiding both the architectural development of OOS systems and the strategic methodologies employed in trajectory and logistics planning.

The findings of this study lead to the following recommendations on the design of servicing architectures:

- While a lower number of servicers allows for significantly more efficient routes in terms of total mission cost, many servicers operating in parallel manifest duration benefits. The corresponding orders of magnitude are predominately determined by the trade-off parameter $p_{\Delta v/\Delta t}$ and the constraint for maximum allowed time of flight for phasing manoeuvres. For lower duration solutions, it is therefore recommended to investigate reducing the maximum allowed transfer durations for phasing before increasing the number of servicers. Especially beyond the number of servicers where the mean individual route cost as well as the total route cost increase, this option for duration decrease becomes more viable.

- In the use case of an agglomeration of client satellites spread across the longitudes of the European continent, with a depot ideally located within that range, small servicing fleets show the highest mean servicer costs and greater deviations. This effect is explained by imbalanced routes, which is the result of minimizing total refuelling cost. When spacecrafts are sized with homogeneous mass configurations within the system of systems design framework, such imbalanced route demands

necessitate spacecraft over-dimensioning, leading to unnecessary propellant mass consumption. This suggests that incorporating servicer sizing as a design variable would yield more optimal solutions using intermediate fleet sizes.

- Distant clients significantly increase total route cost and create greater imbalance among servicer costs. Two potential strategies arise from these findings: developing servicers in multiple weight classes to handle different cost levels in routes, or introducing additional depots to service clusters of satellites more efficiently. An additional consideration is the potential exclusion of satellites as clients if they are not positioned within agglomerated clusters. To achieve more efficient designs, the number of vehicles can be redistributed across multiple routes. For instance, in the case of four servicers with depot at $\Omega = 0°$ in figure 4.5, servicer one could complete route four after finishing its own route, before servicer three returns to the depot. This strategy would maintain the same total refuelling cost and duration, provided that the missing payload propellant can be supplemented by residual payload propellant or refuelling at the depot. Another significant benefit is the reduction in the number of servicing spacecraft in orbit, which ultimately mitigates the risk of additional space debris.

- As the influence of the depot orbit becomes more pronounced in OOR mission design with an increasing number of servicers, optimizing the depot orbit, rather than selecting from a discrete set, becomes increasingly relevant for designs where the number of servicers approaches the number of clients. Iteratively refining depot locations provides a computationally efficient method for optimizing depot orbits, yielding accurate results in this study.

- The optimal depot location for nominal refuelling and rapid refuelling are not aligned, necessitating a prioritization of mission operation modes during infrastructure design, or the identification of a compromise between the two scenarios.

- Circularization in GEO from GTO requires an apogee thrust of approximately 1 500 m/s, representing the most fuel-intensive manoeuvre for servicers and serving as a critical determinant for the spacecraft's wet mass. Regardless of the absolute mass values, the required propellant ratio for the insertion Δv is approximately 38%. Significant servicer and depot mass reductions could be attained by delivering the spacecraft directly into GEO reducing required dry mass or increasing payload capacity. Incorporating insertion into GEO via a kick-stage would thus enable a more tailored mass configuration design for the servicing operations themselves. A

comparative analysis of this scenario would provide valuable insights into the impact of such a modification on the total launch mass. However, this approach would also result in additional kick-stage in orbit, which would contribute to space debris once their mission is complete.

In addition, methodological considerations for advancing the design of servicing missions are derived, offering insights for future developments in optimizing mission planning, trajectory design, and further aspects in OOS architectures design:

- Rigorously design trajectories for improving routing decisions: In the trajectory calculations for servicing manoeuvres, it is crucial to simultaneously account for both in-plane and out-of-plane changes. Even for inclinations below 1°, manoeuvres involving inclination changes become significant when compared to the overall costs. It becomes relatively important when client orbits exhibit small differences in RAAN. In the current use case, inclination-related costs can constitute up to 20% of the total orbit change expenditure in case of small phasing angles, despite the maximum inclination change being just 0.1°. Such factors could induce modifications to the routing of servicing vehicles. As the differences in orbital inclinations grow and more client satellites cluster around similar RAAN values, accurate trajectory calculations including in-plane and out-of-plane manoeuvres become more essential.

- Consider mission constraints and priorities in servicing infrastructure design: The selection of trajectory and its corresponding $\Delta v/\Delta t$ preference directly influence routing decisions, thereby affecting the overall performance of the servicing infrastructure. Additionally, when considered alongside the maximum allowable duration for phasing manoeuvres, these factors play a critical role in determining the range and scale of available discrete solutions.

- Simultaneously optimize spacecraft and architecture design: The architecture design, as explored in this study, including the number of servicers, depot orbit, and trajectory design, must be integrated with spacecraft sizing decisions. Identifying the optimal architecture for a given servicer design is only meaningful when sizing decisions are considered in conjunction with other factors. Since Δv is directly linked to propellant consumption, which is dependent on the spacecraft's total mass at any given time, routing should also account for the mass reduction benefits following initial refuelling, especially for higher-cost transfers. A multi-objective optimization encompassing refuelling operation costs, mass launched into space, propellant mass

consumption and mission duration would offer valuable insights into the coupled behaviour of the system of systems and spacecraft design in its operational context, potentially revealing less costly and more viable solutions.

- Design the OOR architecture for a realistic planned large group of GEO clients: A change in client satellites will inevitably impact the architecture design. This study, by intentionally focusing on a set of representative European client satellites over an extended time frame, allows for general conclusions regarding a European OOR system. With the availability of more precise orbital data for planned satellites, the proposed methodology can be applied to derive optimized solutions for specific spacecraft designs. In the goal of designing a long-term reusable architecture, it is essential to account for a broader set of client satellites to be serviced, given the system's sensitivity to client locations and numbers. By extending the allowable mission duration, operational costs can be significantly reduced. Refuelling clients at scheduled points during their operational lifetimes allows for servicing more clients, as longer service durations reduce the cost per client. Furthermore, incorporating concrete operational constraints, not only based on client propellant demands but also on time-sensitive operational requirements, will be critical in refining the servicing architecture for future missions. Nominal and rapid refuelling priorities highlighting distinct optimal depot locations, underscores the need for careful consideration of operational focus.

- Evaluate sustainability: Incorporate the assessment of reusability and space debris risks into the evaluation of various OOS infrastructure designs. The growing number of servicing spacecraft, depots, and potentially kick-stages introduces additional objects into GEO. It is essential to simulate the reusability of infrastructure, considering multiple servicing missions and depot refuelling from Earth, and to integrate these factors into the overall evaluation of infrastructure. A comprehensive Life Cycle Assessment (LCA) of the proposed servicing missions should complement detailed analyses of reusability and space debris mitigation to assess sustainability for space. The aspect of sustainability is not taken into account so far. Given the potential of OOS to enhance sustainability in space, investigating its actual ecological benefits for both orbital and Earth environments is crucial. Integrating a sustainability rating into the optimization process for OOS infrastructure design would be a significant step towards ensuring the sustainable use of space assets.

5. Conclusion and Outlook

In this thesis, a comprehensive methodology was developed for the design and optimization of an On-Orbit Refuelling infrastructure, aiming at servicing geosynchronous satellites. The approach integrates trajectory selection, logistics optimization, and mission simulation, incorporating mission cost and duration priorities and constraints. The methodology was applied to a representative use case, evaluating the performance of various mission architectures and offering insights into minimizing operational servicing Δv, aiming at enhancing system efficiency.

The developed approach addresses the inherent variability in cost and time trade-off within trajectory design, enabling the integration of system of systems priorities before optimization. This methodology is valuable for concurrent engineering processes, as it can be extended beyond the specific use case explored herein, particularly when applying a generalized trajectory selection model. Both in-plane and out-of-plane manoeuvres are considered for general orbit changes, which allows for a broader range of feasible geosynchronous client orbits. Thereby, more sophisticated route optimization is enabled. The optimization process employs a genetic algorithm specifically tailored to the servicing scenario. The algorithm's robustness assures reliable results, even as client numbers and payload capacities vary. The integration of mission simulation subsequently to the optimization process extends prior research efforts focused on operational optimization. This allows to take into account infrastructure deployment, close proximity operations as well as analysis of propellant consumption along optimized routes. The developed tool is capable of adapting to a wide range of input parameters and user preferences. This adaptability underscores the flexibility of the tool and its potential for scalable applications. It provides a holistic framework for evaluating mission performance across varying GEO client satellite configurations and servicer designs. Moreover, the scenario is transferable to other servicing tasks beyond refuelling, offering the potential to contribute to the development of more general servicing infrastructures. This positions the tool as a critical component in the broader vision of creating a sustainable, long-term logistics ecosystem for space.

For the use case examined in this thesis, the methodology has successfully provided an optimal refuelling infrastructure in terms of operational Δv. The lifespan of 15 European client satellites can be extended by five years through an optimized OOR architecture design with four servicing routes and the depot placed in geostationary orbit at $\Omega = 2°$. 3.96t of propellant are supplied at a cost of 810 m/s within 28 days. General design recommendations are derived based on the analysis of the different architecture designs. Fewer routes are preferable in terms of Δv whereas more servicers decrease mission duration. Total mission cost minimization results in high imbalance across individual routes for refined depot orbits. This points to novel strategies such as client clustering around multiple depots or development of different servicer classes for performance improvement. The findings identify further potential improvements in design methodology.

This study highlights avenues for further refinement through multi-objective optimization. Additionally incorporating spacecraft sizing as a design variable might enable more viable missions when it comes to not only total mission cost and duration, but also propellant consumption, total launch mass, and route efficiency. This would allow for more adaptive infrastructure that can scale with future mission needs and evolving satellite constellations. Expanding the methodology to time-dependent logistics optimization would enable more general orbital servicing beyond GEO, including applications in LEO. This could open new possibilities for multi-mission infrastructure capable of servicing a variety of satellite orbits. The system's performance is highly sensitive to client satellite locations and numbers. Consequently, it is imperative to consider a broader set of real clients with according operational constraints when designing OOR infrastructure.

With the increasing deployment of larger satellite constellations, the need for efficient servicing infrastructures becomes more crucial. The proposed OOR design can serve as a foundation for future servicing missions, but will require continuous refinement to accommodate new mission profiles, client demands, and operational constraints. Lastly, efforts must lie on minimizing the accumulation of space debris by ensuring that servicing spacecraft and depots are reusable. Incorporating the evaluation of space debris risk of the different designs is substantial to ensure that satellite servicing indeed creates more sustainable practices. A Life Cycle Assessment (LCA) of the entire OOS mission cycle would yield further insights into its impacts. These improvements would contribute to a more sustainable space environment as refuelling missions scale in the future.

A. Appendix

A.1. Additional Theoretical Background

A.1.1. Design of OOS and OOR Architectures

Exploration missions may involve depots, in-space transportation vehicles, and In-Situ Resource Utilization (ISRU), with a primary focus on the Moon and the cislunar environment, including the Artemis program and the Lunar Gateway. Tiffin and Friz [84] highlight superior delivery performance of a fully reusable architecture serving both LEO and Near Rectilinear Halo Orbit (NRHO) compared to traditional expendable architectures. Reusable habitat modules with contingency propellant depots enable greater payload capacity for human exploration missions [40], while Smitherman and Woodcock [79] propose a propellant depot infrastructure for Earth-Moon, asteroid, and Mars missions, supporting 90% of propulsion needs for commercial and exploration operations. H. Chen and Ho [13] find significant improvements in initial mass for Earth-Moon-Mars missions through the use of in-orbit depots and ISRU. Crewed missions, supported by high- and low-thrust technologies for return campaigns to the Moon, are further studied by Jagannatha and Ho [43]. Recent work on Low-Energy Transfer (LET) trajectories for lunar exploration [34, 82] and multi-mission scheduling optimization for Artemis [33] continue to refine lunar exploration strategies.

Mathematical Formulations of Logistic Models involve various approaches to optimize space servicing scenarios. Discrete event simulations, pioneered by MIT and resulting in the SpaceNet tool, do not support vehicle routing or architecture optimization. Mixed-Integer Linear Programming (MILP) is widely applied to various problem formulations [22, 75, 88], with the Location Routing Problem (LRP) modelled as an ILP by T. Zhang et al. [100]. Binary Linear Programming (BLP) addresses Facility Location Problems [35, 77]. Non-linear programming focuses on fuel minimization via Δv and transfer durations [101], while Mixed-Integer Non-linear Programming (MINLP) handles complex tasks like multi-spacecraft rendezvous [44, 99] and combined mission planning

and spacecraft design [13, 33]. MINLP is also applied to time-expanded supply chains for varying demand and resupply [72] and to design servicing infrastructures [20]. Generalized Multi-Commodity Network Flow (GMCNF) incorporates resource transformations [72], while Hybrid Optimal Control optimizes P2P strategies [98].

A.1.2. Terminology for Orbital Classes

The ESA Space Debris Office [24] defines orbital classes and their corresponding parameters, as outlined in table A.1. The terminology used in this work adheres to these definitions.

Table A.1.: Orbital Classes

Type	Description	h_p $[km]$	h_a $[km]$	i $[°]$
GEO	Geostationary Orbit	$h_p \in [35586, 35986]$	$h_a \in [35586, 35986]$	$i \in [0, 25]$
GTO	GEO Transfer Orbit	$h_p \in [0, 2000]$	$h_a \in [31570, 40002]$	$i \in [0, 90]$
IGO	Inclined Geosynchronous Orbit	$a \in [37948, 46380]$	$e \in [0.00, 0.25]$	$i \in [25, 180]$
EGO	Extended Geostationary Orbit	$a \in [37948, 46380]$	$e \in [0.00, 0.25]$	$i \in [0, 25]$
GEO_{IADC}	IADC GEO Protected Region	$h \in [35586, 35986]$	$\delta \in [-15, 15]$	

A.1.3. Solution of CVRP with Heuristic Approach

The CVRP to be solved is an NP-hard optimization problem for which heuristic approaches are adapted when approximate solutions are sufficient. Exact solutions are only adapted to small networks [50]. The **Clarke and Wright Savings** algorithm is the best-known approach for solving the CVRP efficiently with a complexity of $O(n^2 \log n)$ [51]. The number of vehicles is free, the algorithm allows therefore to identify the number of servicing vehicles as a variable. It does not require a constant demand among all clients. The algorithm starts with the initial solution of n servicers individually dispatching to one of the n clients with total tour length $2\sum_{i=1}^{n} d(N_0, i)$. Combination of clients i and j in a single tour reduces the total distance by the saving

$$\begin{aligned} s(i,j) &= 2d(N_0,i) + 2d(N_0,j) - [d(N_0,i) + d(i,j) + d(N_0,j)] \\ &= d(N_0,i) + d(N_0,j) - d(i,j) \end{aligned} \tag{A.1}$$

A combination of i and j in a single tour is forbidden if it results in CVRP constraint violation. The algorithm follows the steps in flow chart A.1. The CVRP solutions are the final created routes.

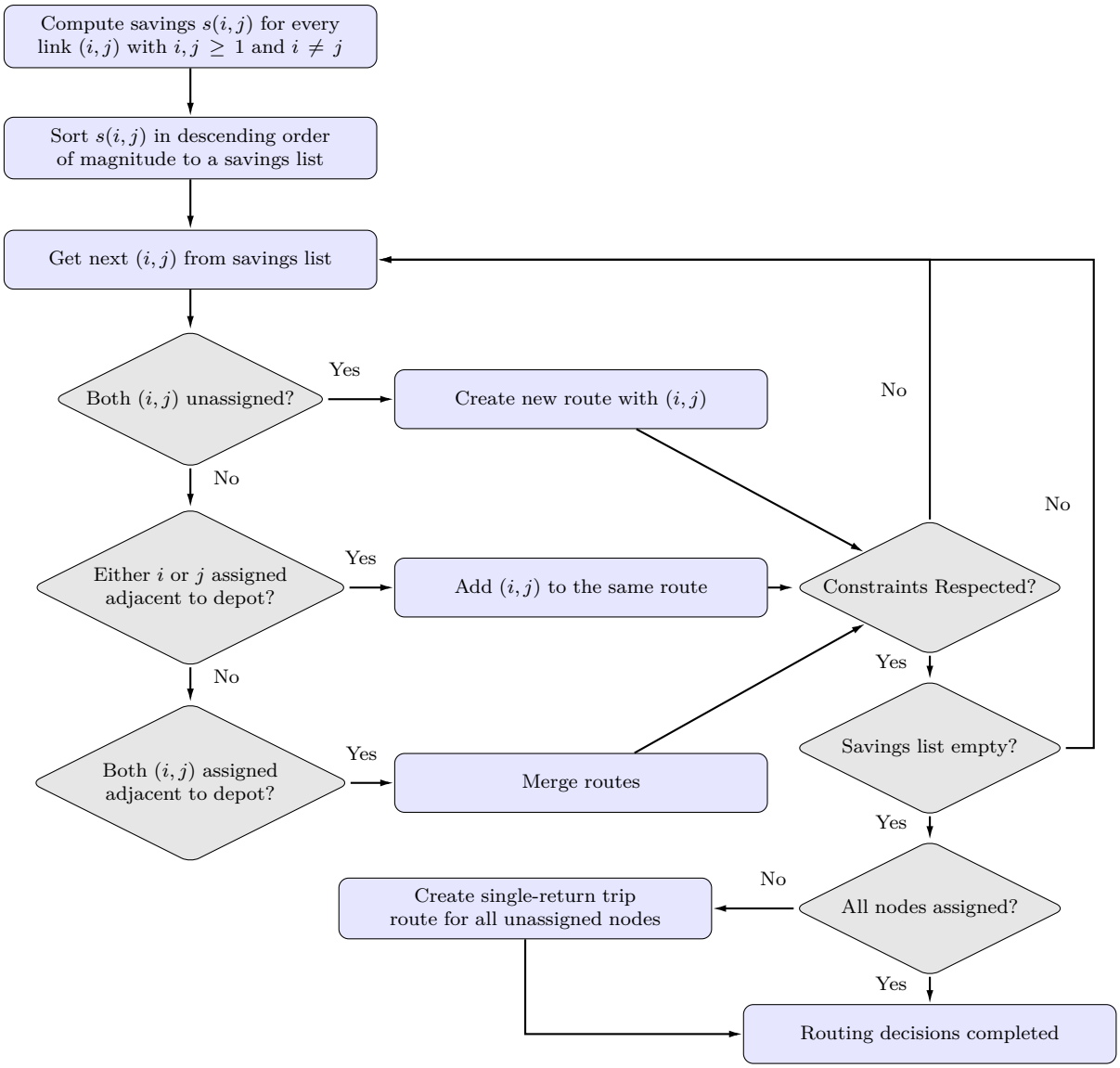

Figure A.1.: Clarke and Wright Savings Algorithm

A.2. Additional Methodological Developments

A.2.1. Design Flow

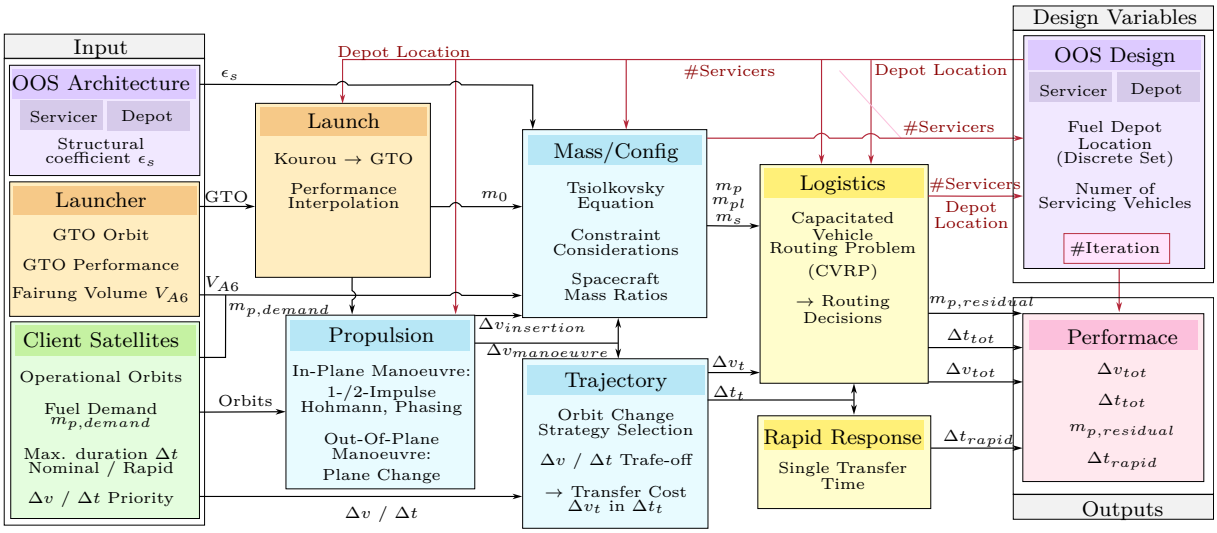

Figure A.2.: Design Flow

A.2.2. Transfer Manoeuvres

Phasing

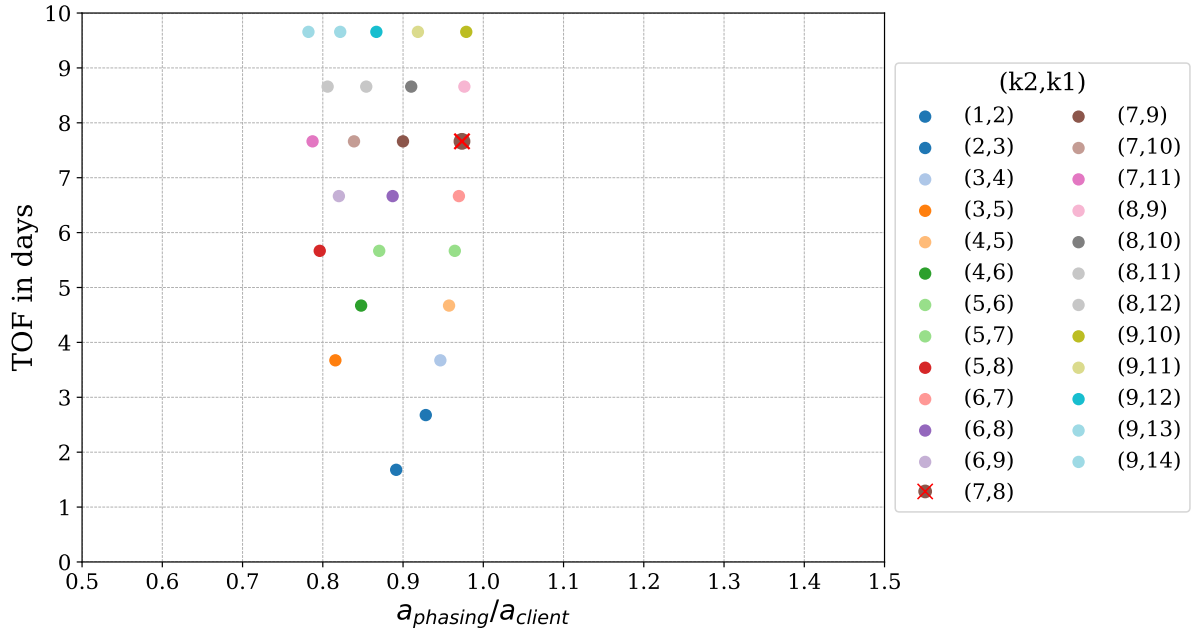

Figure A.3.: TOF Comparison of Subsynchronous Phasing Manoeuvres

Hohmann Transfer with Selection

Depending on start and target orbit properties and relations, the most energy efficient transfer might not be the single thrust strategy [56]. Coplanar manoeuvres alter geometric properties of the conic section to modify size and shape of the orbit. The Hohmann Transfer (2.24) is the Δv optimal two-impulse transfer manoeuvre. It is also energy optimal for coaxial coplanar elliptic orbits [65] which was proven in 1986 [41]. In a the general case of an elliptic Hohmann transfer from initial elliptical orbit 1 to the target elliptical orbit 2 via a transfer ellipse t, different cases of transfer scenarios are possible changing a and e simultaneously by change of radii of apogee and perigee. Thrusting at apogee raises perigee if acceleration and lowers it in case of deceleration. Analogous, thrusting at perigee lowers or raises apogee. Pontani [68] proves two-impulse globally optimal transfers. He states that final ellipses are optimally oriented when they are coaxial and aligned having their perigees on the same side which leaves the following two scenarios:

1. Case I: First thrust at perigee of initial ellipse $e1$ to apogee of final ellipse $e2$.
2. Case II: First thrust at apogee of initial ellipse $e1$ to perigee of final ellipse $e2$.

Equation (A.4) is the total cost of the Hohmann transfer between elliptic orbits with a first impulse at r_1 (A.2) on the initial orbit at apogee or perigee and a second impulse at r_2 (A.3) on the target orbit. The transfer orbit depends on the selected transfer strategy following $a_t = (r_1 + r_2)/2$.

$$\Delta v_1 = \left| v_t\left(r_1\right) - v_1\left(r_1\right) \right| = \left| \sqrt{\frac{2\mu}{r_1} - \frac{\mu}{a_t}} - \sqrt{\frac{2\mu}{r_1} - \frac{\mu}{a_1}} \right| \tag{A.2}$$

$$\Delta v_2 = \left| v_2\left(r_2\right) - v_t\left(r_2\right) \right| = \left| \sqrt{\frac{2\mu}{r_2} - \frac{\mu}{a_2}} - \sqrt{\frac{2\mu}{r_2} - \frac{\mu}{a_t}} \right| \tag{A.3}$$

$$\Delta v_{\text{tot}} = \Delta v_1 + \Delta v_2 \tag{A.4}$$

To identify the most efficient strategies, Hohmann transfer orbits for Case I Δv_{PEtoAP} and Case II Δv_{APtoPE} are calculated within a range around the GEO orbit of $r_a, r_p \in [30\,000,\, 40\,000]$ km. Plotting over apogee and perigee ratios of target and initial orbit allows for classification of orbital transfers as figure A.5 shows. For a transfer to an orbit at higher apogee, thrusting first at perigee is more efficient $\Delta v_{PEtoAP}/\Delta v_{APtoPE} < 1$, while the thrusting at perigee in a second burn is advantageous for lowering the apogee

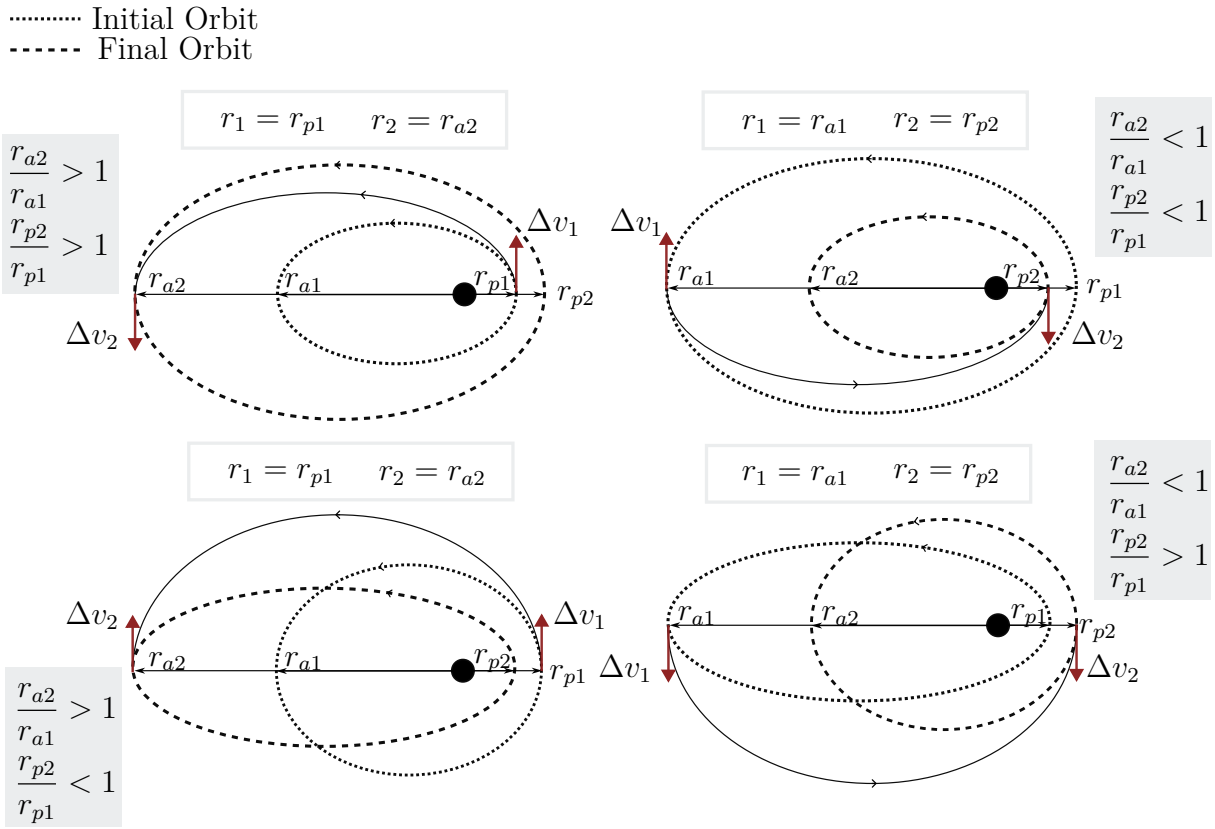

Figure A.4.: Hohmann Strategies: Classification for identification of most effective transfer manoeuvres between elliptic orbits. First thrust at perigee on the left, first thrust at apogee on the right.

$\Delta v_{PEtoAP}/\Delta v_{APtoPE} > 1$. Where the ratios are equal to one, both transfers are equally efficient $\Delta v_{PEtoAP}/\Delta v_{APtoPE} = 1$ and thrusting at apogee for $r_{a2}/r_{a1} = 1$ or perigee for $r_{p2}/r_{p1} = 1$ first is equivalent to a single-impulse transfer in coinciding points of the orbit. The diagonal line for $r_{a2}/r_{a1} = r_{p2}/r_{p1}$ corresponds to purely circular transfers where any point of the orbit is suitable to initiate the manoeuvre or orbits with the same eccentricity. For elliptic orbits where cost as well as time of transfer are equivalent, the strategy with the shortest waiting time is initiated, depending on the actual position of the spacecraft.

In case of two orbits intersecting on either apogee or perigee, a single impulse manoeuvre on the apsidal line is feasible and the required tangential velocity change simply amounts to

$$\Delta v = v_2\left(r_{a/p,2}\right) - v_1\left(r_{a/p,1}\right) \tag{A.5}$$

This is intrinsically incorporated in the Hohmann transfer strategy selection.

The transfer time depends only on the semi-major axis of the transfer orbit a_t following

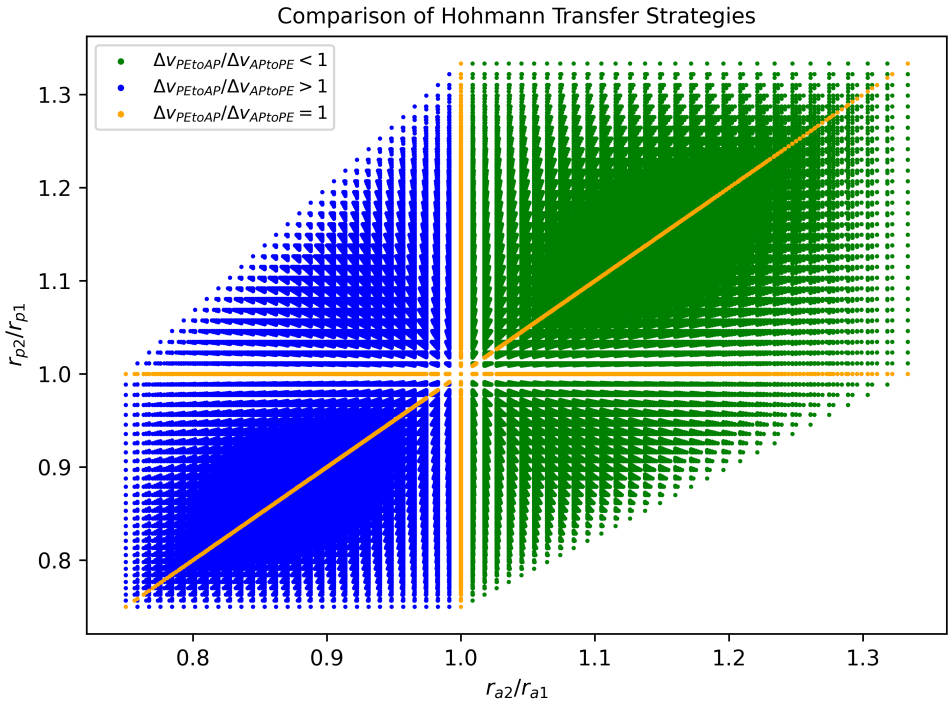

Figure A.5.: Comparison of Hohmann Transfer Strategies: Transfer Cost Δv

equation (2.25) and is therefore also strategy dependent. The thrusting strategy impacts transfer time. Figure A.6 points out the most time efficient transfer strategies. Only for circular orbits, the transfer time is equal. When $r_{p2}/r_{p1} > r_{a2}/r_{a1}$, first thrusting at perigee results in lower transfer times while thrusting first at apogee allows faster transfers if $r_{p2}/r_{p1} < r_{a2}/r_{a1}$.

Comparing the two figures A.5 and A.6 underlines contradicting strategy selections which result in the need for a trade-off between time and cost. Only for a transfer to a higher orbit with both perigee and apogee ratio superior to one and $r_{p2}/r_{p1} > r_{a2}/r_{a1}$ as well as for a transfer to a lower orbit where $r_{p2}/r_{p1} < r_{a2}/r_{a1}$ the strategies for time and cost effectiveness coincide. With an the input priority of cost to time $p_{\Delta v/\Delta t}$, the Hohmann transfer selection function takes another input. The choice is taken into account for selecting the most efficient strategy for either cost or time.

The time on an orbit for reaching apogee or perigee is denoted waiting duration. To calculate the waiting duration from the current true anomaly to transfer initiation, the true anomaly as given in equation (2.8) is used which requires transformation to the eccentric anomaly from the true anomaly first following equation (2.7).

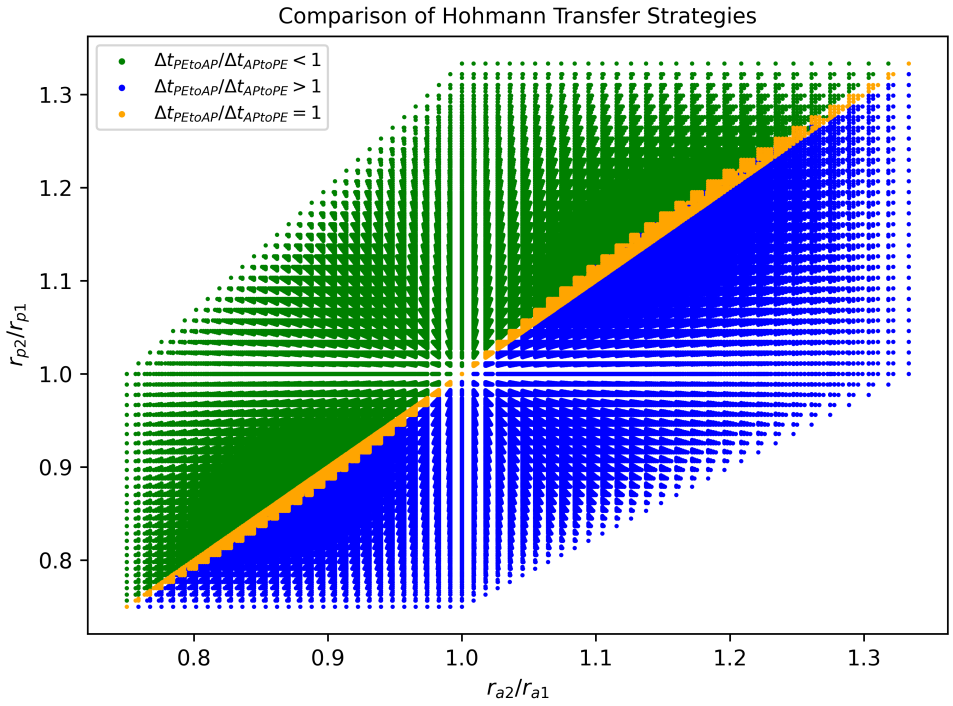

Figure A.6.: Comparison of Hohmann Transfer Strategies: Transfer Time Δt

$$\Delta t_{\text{wait}} = \frac{M_2(\nu_2, e) - M_1(\nu_1, e)}{\sqrt{\frac{\mu}{a^3}}} \tag{A.6}$$

The direction of motion on the orbit is relevant such that $\nu_2 < \nu_1$ requires adaption to $\nu_2 + 2\pi > \nu_1$ for computation of the actual waiting time to reach ν_2 from ν_1. The orbit reached through the Hohmann transfer has required a and e, but also changed true anomaly of $\nu_{\text{arrival}} = \nu_{\text{transfer}} + \pi$ calculated depending on the transfer strategy.

Finally, for the case of increasing the perigee and lowering apogee, Case II is optimal with initial acceleration and deceleration at insertion (first raise perigee, then lower apogee). To lower perigee and increase apogee, the opposite strategy of Case I is optimal by same thrusting actions (first raise apogee, then lower perigee). To lower both apogee and perigee, decelerating impulses are performed first in apogee, then in perigee which corresponds to Case II (first lower apogee, then lower perigee). The opposite scenario of pure acceleration in first perigee, then apogee as in Case I is the optimal strategy for raising both perigee and apogee (first raise perigee, then raise apogee). Concluding from those theoretical results: Strategy in Case II is performed for lowering apogee while Case I is chosen for raising apogee.

Rendezvous through Hohmann Transfer

A Hohmann transfer for rendezvous is feasible only when the angle of advance of the target to the first Hohmann thrust in the initial orbit is Θ_H [15]

$$\Theta_H = \pi \left[1 - \left(\frac{1 + r_1/r_2}{2} \right)^{3/2} \right] \tag{A.7}$$

For a deviation from Θ_H by $\Delta\Theta = \nu_2 - \nu_1 - \Theta_H$, a waiting time $t_{\text{wait,Hohmann}}$ is introduced before initiation of the manoeuvre raising the transfer duration [15] .

$$t_{\text{wait,Hohmann}} = \frac{\Delta\Theta}{\frac{2\pi}{P_1} - \frac{2\pi}{P_2}} \tag{A.8}$$

A simultaneous Hohmann transfer and true anomaly correction are usually time costly. The spacecrafts must initiate the transfer in apogee or perigee when the true anomaly in the final orbit can be reached at the end of the apsidal line. For circular orbits, the problem has been formulated by Chobotov [15] allowing for calculation of Hohmann phasing angle θ_H (A.7) and waiting time during cruising $t_{\text{wait,Hohmann}}$ (A.8). This transfer scenario is only selected for circular orbits, as the restriction of alignment of apsidal lines for elliptic orbits would increase waiting time even further. Nevertheless, the transfer option is also implemented within the tool for changes between elliptic orbits.

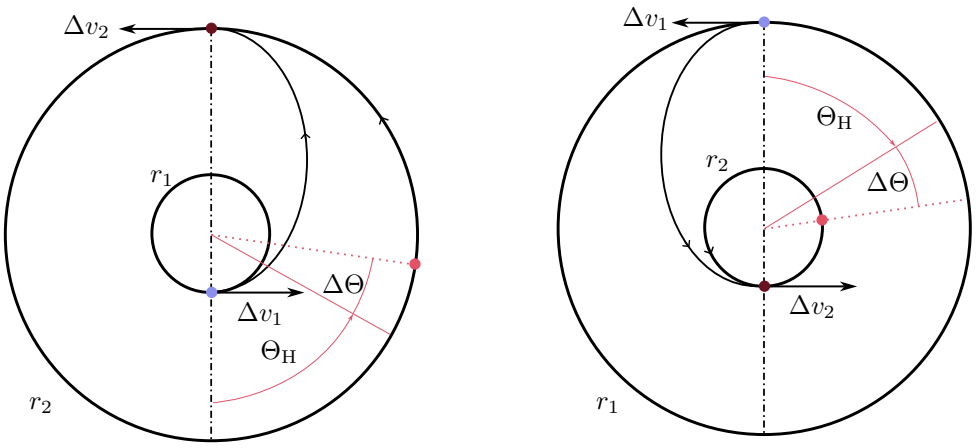

Figure A.7.: Hohmann Transfer with Rendezvous

Applying the same formula for both transfers of lowering and raising the orbit, $\Theta_H < 0$ and $\Delta\Theta < 0$ $r_1 > r_2$ as depicted in figure A.7 with $\Delta\Theta = \nu_2 - \nu_1 - \Theta_H$. Equation (A.7) gives the limit of $|\Theta_H| < 0.64645\pi$. The servicer needs to leave its orbit at $\nu_{\text{transfer}} =$

$2\pi t_{\text{wait,Hohman}}/P_1$. When $\Delta\Theta < 0$, 2π are added increasing the waiting time accordingly instead of assuming infeasibility when $r_1 < r_2$. The opposite is valid for $r_2 < r_1$, when $\Delta\Theta > 0$, 2π are deducted.

Simultaneous Inclination Change and Hohmann Transfer

Inclination change can be applied either at apogee or perigee of the Hohmann transfer ellipse or within the line of intersection of the two orbital planes for single-thrust manoeuvres. Simultaneous speed and plane change are more efficient than subsequently changing both [17]. Thrusting at apoapsis, where distance to the attractor is the highest, requires the smallest Δv as there is no radial velocity contribution and speed is lower than in perigee. Following the law of cosines (2.32) induces a rotation around the common apsidal line of Δi.

$$\Delta v = \sqrt{v_1^2 + v_2^2 - 2v_1 v_2 \cos(\Delta i)} \tag{A.9}$$

The inclination change may also be split among the two impulses at combination with two-impulse manoeuvres which can be optimized to minimize the Δv by plane change requiring an iterative solution scheme [15]. Vallado and McClain [93] present an approximate solution at accuracy of 0.5° to estimate the ideal distribution of Δi among the two burns: $s\Delta i$ are changed at first impulse, which leads to remaining angular change of $(1-s)\Delta i$ at second impulse.

$$\Delta v = \sqrt{v_1^2 + v_{t,1}^2 - 2v_1 v_{t,1} \cos(s\Delta i)} + \sqrt{v_2^2 + v_{t,2}^2 - 2v_2 v_{t,2} \cos\big((1-s)\Delta i\big)} \tag{A.10}$$

The approximative solution is [93]

$$s \approx \frac{1}{\Delta i} \arctan\left(\frac{\sin \Delta i}{\frac{v_1 v_{t,1}}{v_2 v_{t,2}} + \cos \Delta i}\right) \tag{A.11}$$

If the total inclination change is smaller than the accuracy of the approximation, the inclination is not split across the two impulses, but applied only at perigee. Simultaneous inclination change and Hohmann transfer for rendezvous for circular orbits are not considered, since the pure inclination change is restricted to transfer initiation in ascending and descending node which limits the rendezvous options and leads to high waiting times, if the transfer is even feasible.

Lambert Problem

The Lambert transfer enables rendezvous between two orbits within a set time, eliminating phase differences when the servicer and client share the same orbit. However, due to its iterative, fuel-intensive nature and fixed time requirement, it is not used here. Instead, energy-efficient Lambert transfers for phasing ($r_1 = r_2$) and Hohmann transfers ($r_1 \neq r_2$) are applied.

To achieve rendezvous of two objects in space, the active spacecraft must not only transfer to the passive spacecraft's orbit, bust must also match its true anomaly. The Lambert's Problem describes the orbit change between to given points in space within a given time of flight, and direction of flight. The time of flight (TOF) depends on the the semi-major axis of the transfer orbit, the distance between the points as well as the radii of the points. It results that for a given time of flight, a maximum number of revolutions N_{max} is possible leading to $2N_{max} + 1$ choices for the transfer orbit a. Comparing the required Δv for the two-impulse transfer manoeuvre, minima are found for introducing a coasting time which reduces the time of flight to its actual duration. Such local energy minima correspond to **phasing manoeuvres** when radii of initial and final point are equivalent. Here, the two points coincide and the impulses are provided at the same position. The optimal solution for orbits at different altitudes is the **Hohmann transfer** which requires a sufficient time of flight. [21]

If only single revolution transfers are considered, two solutions for the short elliptic and long ellitpic transfer exist for a given TOF $\Delta t_{Lambert}$ if only one direction of flight is considered [67]. The Lambert equation to be solved is

$$\Delta t_{Lambert} = \sqrt{\frac{a^3}{\mu}} \left(\alpha - \beta - (\sin\alpha - \sin\beta)\right) \tag{A.12}$$

$$\sin\left(\frac{\alpha}{2}\right) = \sqrt{\frac{s}{2a}} \tag{A.13}$$

$$\sin\left(\frac{\beta}{2}\right) = \sqrt{\frac{s-c}{2a}} \tag{A.14}$$

where $c = \|\overrightarrow{r_2} + \overrightarrow{r_1}\|$ is the chord and $s = \frac{c+r_1+r_2}{2}$ is the semi-perimeter. The equation can be solved for identifying a, using a bisection algorithm which converges to a unique solution for elliptic transfers if it exists [67]. With the identified transfer orbits, velocities at the corresponding intersection points can be determined, and Δv can be

computed. Minimum and maximum TOF can be determined for a Lambert transfer from the geometry of the problem: The minimum TOF corresponds to a parabolic flight time while the minimum semi-major axis $a_{min} = s/2$ allows to determine the maximum TOF [67]. The Multiple-Revolution Lambert Problem changes the Lambert equation to $\Delta t_{Lambert} = \sqrt{\frac{a^3}{\mu}} \left(2\pi N\alpha - \beta - (\sin\alpha - \sin\beta)\right)$ [70].

For small changes in ν, Hohmann transfer can achieve lower transfer times than solutions to the Lambert's problem [15]. With a rise in angular difference, Hohmann transfer times increases rapidly while Lambert's phasing manoeuvres decrease in time and Δv. The Lambert technique or semi tangential techniques is therefore interesting, when time is restrictive and Δv is available.

Semitangential Transfer

Semitangential transfer manoeuvres are more fuel intensive than Hohmann transfer intersecting the target orbit twice allowing for two potential points of rendezvous. The impulse applied at apogee or perigee exceeds the Hohmann impulse, and with known radius at intersection, properties of the transfer orbit and Δv can be calculated taking into account the required change of flight path angle γ at insertion in final orbit [15].

One tangent burn transfers have parabolic or hyperbolic orbits between coaxial aligned elliptic orbits. With known initial and final radii r_1 r_2 and true anomaly ν_2 at second burn point of the final orbit, properties of the transfer orbit a_t, e_t and required Δv and transfer time are determined. [93]

With $R^{-1} = \frac{r_1}{r_2}$, change at periapsis $(-)$ or apoapsis $(+)$, the transfer orbit follows $\Phi_2 = \arctan\left(\frac{e_t \sin\nu_2}{1 + e_t\cos\nu_2}\right)$.

$$e_t = \frac{R^{-1} - 1}{\cos\nu_2 \mp R^{-1}} \tag{A.15}$$

$$a_t = \frac{r_1}{1 \mp e_t} \tag{A.16}$$

For transfers at perigee, $\nu_2 < 180°$ and at apogee $\nu_2 > 180°$. r_1 is equivalent to the apoapsis or periapsis.

$$\Delta v_1 = \sqrt{\frac{2\mu}{r_1} - \frac{\mu}{a_t}} - \sqrt{\frac{2\mu}{r_1} - \frac{\mu}{a_1}} \tag{A.17}$$

$$\Delta v_2 = \sqrt{v_{t,2}^2 + v_2^2 - 2v_{t,2}v_2\cos\Phi_2} \quad \text{with} \quad v_2 = \sqrt{\frac{2\mu}{r_2} - \frac{\mu}{a_2}} \quad v_{t,2} = \sqrt{\frac{2\mu}{r_2} - \frac{\mu}{a_t}} \tag{A.18}$$

$$\Delta v = |\Delta v_1| + |\Delta v_2| \tag{A.19}$$

$E_0 = 0°$ if the transfer starts at periapsis and $E_0 = 180°$ for first burn at apogee. With $E = \arccos\left(\frac{e_t + \cos\nu_2}{1 + e_t\cos\nu_2}\right)$, the time of transfer, which is shorter than the Hohmann transfer, is calculated with the general form of the Kepler's equation

$$\Delta t = \sqrt{\frac{a_t^3}{\mu}}\left[2k\pi + (E - e_t\sin E) - (E_0 - e_t\sin E_0)\right] \tag{A.20}$$

with the number of completed revolutions in addition between moving between two locations k for computing the eccentric anomaly. It is assumed $k = 0$ for all the transfers regarded in this work. E is chosen out of the two solutions $E_2 = 360° - E_1$ to be in the same half $[0 - 180°]$ or $[180 - 360°]$ as the true anomaly.

Implementation: The semitangential transfer adapts the true anomaly by transfer from an initial orbit at perigee or apogee to a final orbit at specified true anomaly. As the true anomaly is specified, orbit size, shape and true anomaly can be adapted simultaneously. Δv for the transfer as given in equation (A.19) is higher than for a Hohmann transfer, but a semitangential transfer generally has lower transfer time as indicated in equation (A.20). The transfer is initiated in perigee, if the true anomaly is lower than π, while it takes place at apogee when the true anomaly surpasses that value. It corresponds to a Hohmann transfer for $\nu_2 = \pi$ which is therefore excluded from this transfer technique. Testing shows that the transfers are only feasible for certain combinations of eccentricities and final true anomalies. For certain geometric cases, there might therefore not exist the alternative faster transfer to the Hohmann transfer with direct anomaly adaption.

A.2.3. Trajectory Selection

Complete Trajectory Selection for Orbital Transfers between GEO Orbits

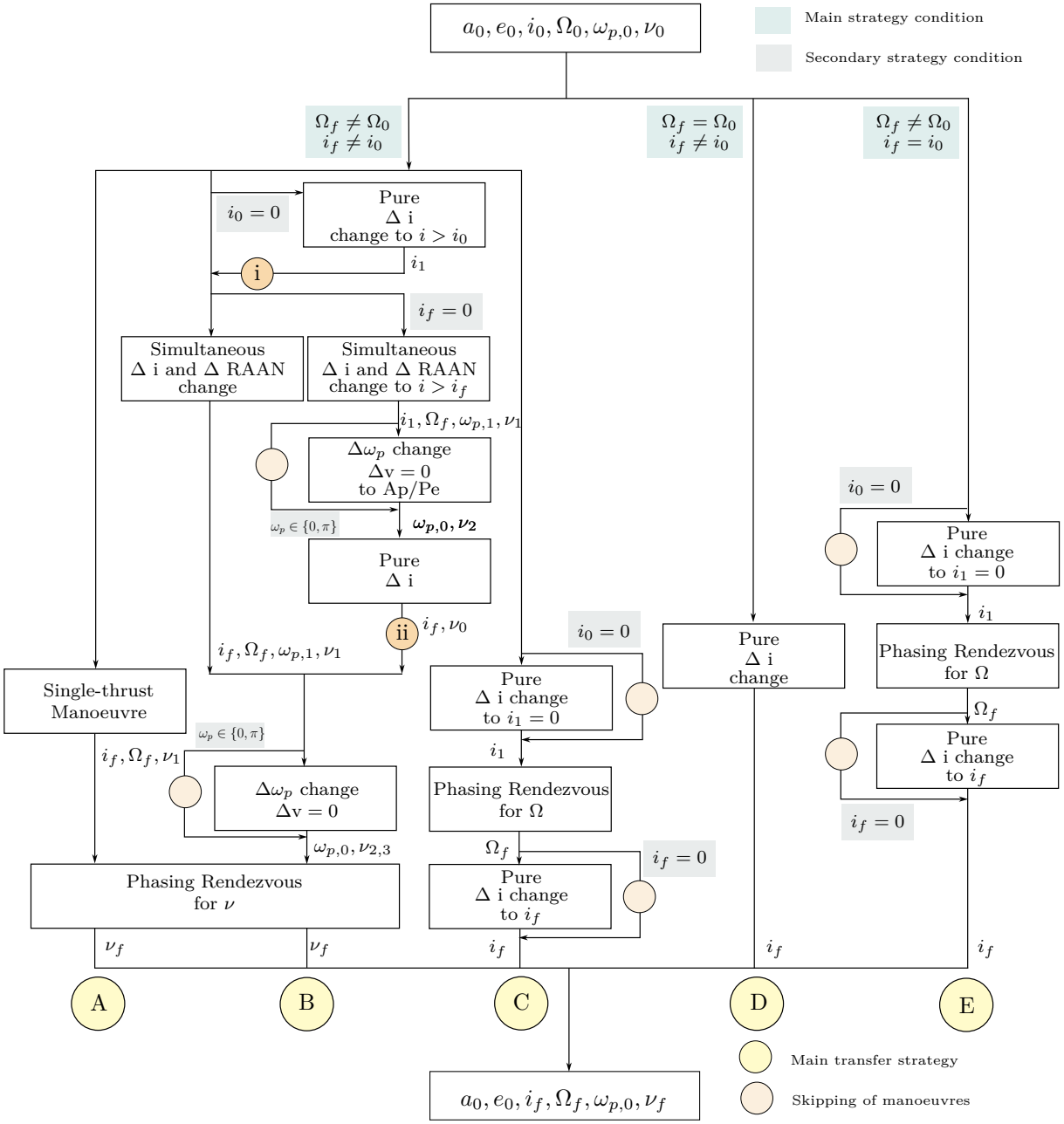

Figure A.8.: Trajectory Strategies for Stationary Orbit Change

Complete Trajectory Selection for General Orbital Transfers

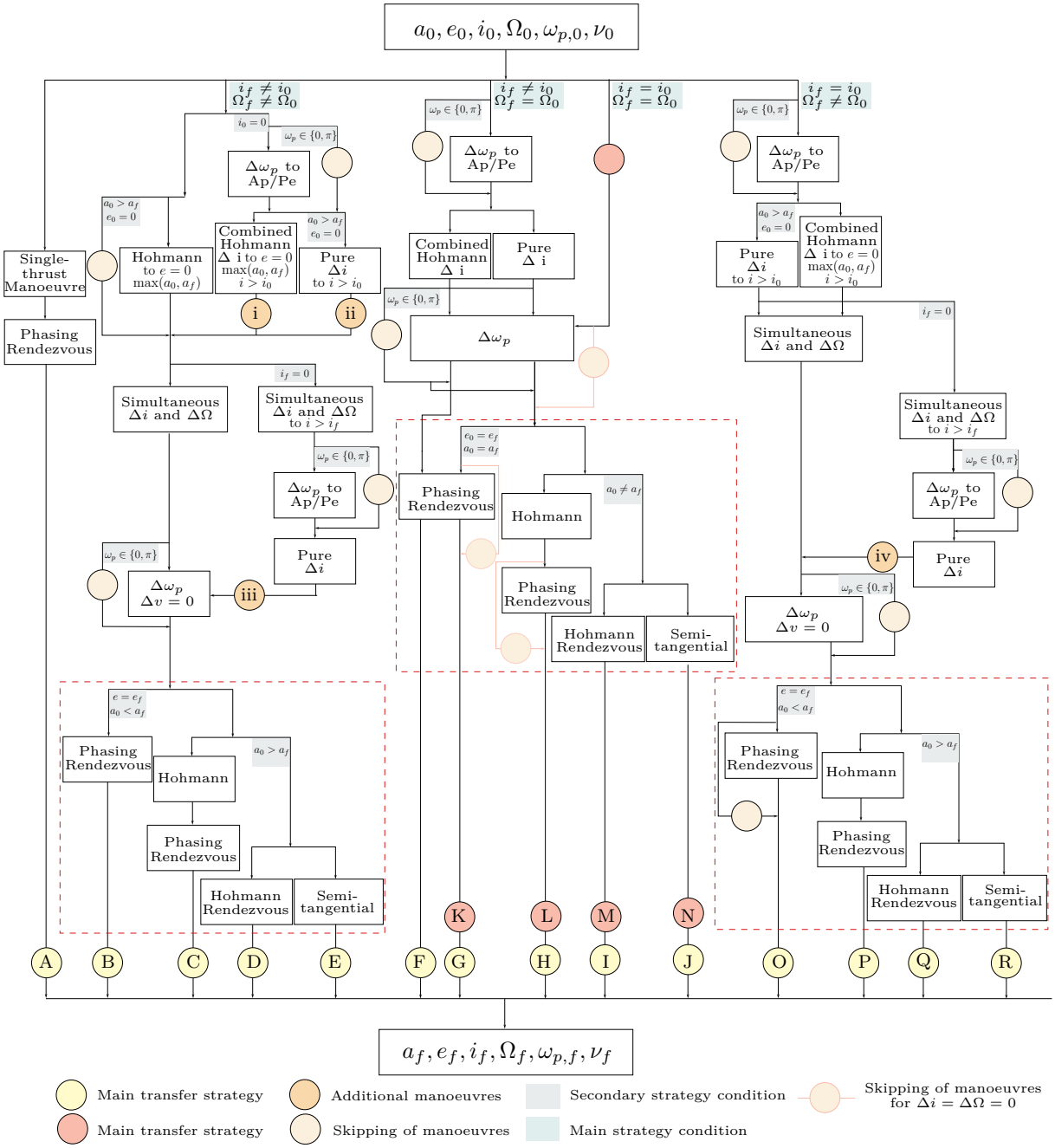

Figure A.9.: Trajectory Strategies for General Orbit Change

Verification of the general transfer mode with the stationary transfer mode: In the context of a geosynchronous orbit, both the stationary and general transfer strategies serve as verification mechanisms for the overall transfer modes. When a change in RAAN and inclination is required, strategies A and B are applicable in both modes. However, strategy C with RAAN phasing, which offers temporal advantages, is exclusively valid

for stationary orbit modes, although it results in equivalent costs to other strategies. For manoeuvres solely involving pure inclination change, both modes require analogous manoeuvres. In particular, strategy A or G in the general mode correspond to strategy D in the stationary mode. Conversely, when a change in RAAN is the sole requirement, strategies A and O correspond to Strategy E in the stationary mode. The single impulse transfer further delivers the same results as the multiple impulse strategies for the case of initial condition at perigee or apogee if the intersection search selects the same point of intersection for the single impulse manoeuvre as is computed in the other trajectory paths.

A.3. Detailed Scenario and Use Case Data

A.3.1. Reference Data

Industry Standards for Servicer and Depot Sizing: The values presented in table A.2 are broad estimates aligned with industry standards for On-Orbit Refuelling scenarios, though they may vary based on specific mission requirements and technological capabilities. Dry mass is contingent on the propulsion system, mission profile, structural design, and scale. Refuelling capacities are sized according to the number of client satellites and fuel demands, with GEO depots designed to support multiple refuelling operations.

Table A.2.: OOR Industry Standards for Servicer and Depot Characteristics

	Servicer	Depot
Dry mass m_{dry}	200kg-2 000kg	1 000kg-5 000kg
Capacity m_{cap}	100kg-1 000kg	1 000kg-10 000kg or more
Fuel Mass m_{fuel}	50kg-500kg	

Spacecraft sizing of past and planned OOR and OOS missions are further indications for mass configurations in this study. Progress MS delivers up to 850 kg of propellant with a total cargo of 2350 kg and a mass of 7280 kg [31]. In 2019, OrbitFab successfully resupplied the ISS with water as part of the Furphy project [9]. Thianzhou-2 delivered 1.95 t of propellant and additional cargo, totalling 4.69 t of payload, with a launch mass of 13.5t to the Chinese Space Station [45]. Tanker-001 is a small satellite, weighing 35 kg designed to demonstrate the capabilities of OrbitFab's Rapidly Attachable Fluid Interface (RAFTI) system in orbit. The refuelling adapter provides a flow rate of 500 ml/min at low pressure [62]. Given the density of hydrazine as 1.01 g/ml [92], this flow rate corresponds to approximately 0.505 kg/min. The OrbitFab Tanker 002 heading to GEO will carry 90.7 kg of hydrazine [23]. The Exploration Company's reusable and refuelable Nyx vehicle, features a mass of 10.5 t, a volume of 4×7.5 m, and is equipped with 20×200 N thrusters for depot refuelling. D-Orbit's ION Satellite Carrier has conducted 13 missions since 2020, deploying over 100 satellites, with a 500 kg mass and 40% propellant ratio. The GEA Logistics Vehicle, set for a 2028 launch, will transport 2.5 t clients to GEO and perform OOS. ArianeGroup's ASTRIS Kick-stage, with a dry mass of ~900 kg and volume of 4.2×1.14 m, supports missions for 2 t payloads, achieving a fuel-to-mass ratio of 0.49 with a 2100 m/s Δv. [8]

Client satellites:

The European GEO satellite constellations include HYLAS (3x), Eutelsat (34x), Hellas-Sat (x), Amazonas (5x), Hispasat (4x), INMARSAT (13x), SES Satellites (20x), Astra by SES (14x), and NSS by SES (6x).

Table A.3.: European GEO Client Satellites

ID	Satellite	Ω [°]	h_p [km]	h_a [km]	e	i [°]	m_0 [kg]	m_p [kg]	$\frac{m_p}{m_0}$	EOL	Operator
01	Eutelsat 117 West B	−116.8	35779	35795	1.90e−4	0.02	5500	3200	0.582	2030	France
02	SES-11	−105	35785	35801	1.90e−4	0	5200	2829	0.544	2032	LUX
03	SES-2	−87	35778	35798	2.37e−4	0.01	3200	1755	0.548	2029	UK/LUX
04	SES-10	−67	35777	35799	2.61e−4	0	5271	2463	0.467	2032	LUX
05	Eutelsat 65 West A	−65	35776	35796	2.37e−4	0.08	6654	3896	0.586	2031	France
06	Amazonas-5	−61	35785	35789	4.74e−5	0.04	5900	3429	0.581	2032	Spain
07	Telestar 12V	−15	35645	35727	9.75e−5	0.1	4900	2666	0.544	2030	Canada
08	Eutelsat 8 West B	−8	35773	35814	4.86e−4	0.1	5800	3155	0.544	2030	France
09	Thor-7	−1	35782	35790	1.66e−4	0	4600	2800	0.609	2030	Norway
10	BulgariaSat-1	1.9	35774	35797	2.73e−4	0	3669	1995	0.544	2032	Bulgaria
11	Eutelsat 3B	3	35782	35791	1.07e−4	0.07	5967	3244	0.544	2029	France
12	Eutelsat 9B	9	35780	35792	1.42e−4	0.08	5200	2829	0.544	2031	France
13	Astra 1L	19.3	35772	35798	3.08e−4	0.05	4500	2247	0.499	2032	LUX
14	Astra 2G	28.2	35785	35789	4.74e−5	0.09	6000	3264	0.544	2029	LUX
15	Astra 5B	31.55	35787	35793	7.12e−5	0.05	5724	3114	0.544	2029	LUX
16	Hellas-Sat 3	39	35685	35788	1.22e−3	0	5780	3280	0.567	2032	Greece/UK
17	SES-9	108.02	35787	35791	1.90e−4	0.05	5271	2436	0.462	2031	UK/LUX
18	Eutelsat 172B	172	35772	35816	5.22e−4	0	3600	1958	0.544	2032	France
						Total	**96836**	**49800**	**0.544**		

Table A.4.: Selected European GEO Client Satellites for Refuelling Scenario

ID	Satellite	Ω [°]	h_p [km]	h_a [km]	e	i [°]	m_0 [kg]	m_p [kg]	$\frac{m_p}{m_0}$	m_d [kg]	EOL
01	Eutelsat 117 West B	−116.8	35779	35795	1.90e−4	0.02	5500	3200	0.582	367	2030
02	SES-11	−105.0	35785	35801	1.90e−4	0.00	5200	2829	0.544	282	2032
03	SES-2	−87.0	35778	35798	2.37e−4	0.01	3200	1755	0.548	178	2029
04	SES-10	−67.0	35777	35799	2.61e−4	0.00	5271	2463	0.467	152	2032
05	Amazonas-5	−61.0	35785	35789	4.74e−5	0.04	5900	3429	0.581	392	2032
06	Telestar 12V	−15.0	35645	35727	9.75e−5	0.10	4900	2666	0.544	266	2030
07	Eutelsat 8 West B	−8.0	35773	35814	4.86e−4	0.10	5800	3155	0.544	314	2030
08	Thor-7	−1.0	35782	35790	1.66e−4	0.00	4600	2800	0.609	347	2030
09	BulgariaSat-1	1.9	35774	35797	2.73e−4	0.00	3669	1995	0.544	198	2032
10	Eutelsat 9B	9.0	35780	35792	1.42e−4	0.08	5200	2829	0.544	282	2031
11	Astra 1L	19.3	35772	35798	3.08e−4	0.05	4500	2247	0.499	177	2032
12	Astra 5B	31.6	35787	35793	7.12e−5	0.05	5724	3114	0.544	310	2029
13	Hellas-Sat 3	39.0	35685	35788	1.22e−3	0.00	5780	3280	0.567	358	2032
14	SES-9	108.0	35787	35791	1.90e−4	0.05	5271	2436	0.462	143	2031
15	Eutelsat 172B	172.0	35772	35816	5.22e−4	0.00	3600	1958	0.544	195	2032
						Total	**81985**	**42997**	**0.544**	**3960**	

A.3.2. Parameters

Table A.5.: Servicer and Depot Characteristics

	Servicer Small	Servicer Large	Depot
Number of Vehicles in Ariane 6.4	3	2	1
Initial Mass m_0	3 500kg	5 500kg	11 000kg
Dry Mass/ Structural Mass m_s	1 050kg	1 650kg	3 300kg
Capacity/ Payload Mass m_{pl}	1 100kg	1 500kg	3 100kg
Initial propellant mass m_p	1 350kg	2 350kg	4 600kg
Engine	BERTA	BERTA	10 x 400 N BI
Thrust T	5kN	5kN	4.25kN
Specific Impulse I_{sp}	320s	320s	321s
Thruster Mass	26kg	26kg	43kg
Refuelling Interface	RAFTI	RAFTI	RAFTI
Refuelling Interface	1.1kg	1.1kg	1.1kg
Refuelling Transfer Rate	0.505kg/min	0.505kg/min	0.505kg/min
Height h	1.5m	3m	10m
Diameter d	4.5m	4.5m	4.5m
Volume $V = \pi d^2/4$	$24m^3$	$48m^3$	$160m^3$

Table A.6.: Input Parameter Details

Parameter	Value	Description
Scenario Type	refuelling	Name of scenario type
`scenario`		String
Verbose Mode	false	Debug (display figure)
`verbose`		Boolean
Starting Epoch	2028-01-01 00:01:10	Starting time of the mission
`starting_epoch`		String (Datetime)
Output File Path	./Results	Filepath for all output files
`dir_path_for_output_files`		String (Filepath)
Cost vs Duration	0.1	Trade-off factor for $\Delta v/\Delta t$
`cost_vs_duration`		Float, range: 0.0-1.0
Demand Percentage	0.33	Demand level of the mission
`demand_percentage`		Float, range: 0.1-1.0
Client Database Usage	true	Client definition through database
`clients_use_database`		Boolean
Client Constellation Name	GEO	Name of constellation of client satellites
`constellation_name`		String
Servicer Initial Fuel Mass	1350.0 kg	Fuel mass at the start for the servicer
`servicer_initial_fuel_mass`		Float, kg

Parameter	Value	Description
Servicer Payload Capacity	1100.0 kg	Payload capacity of the servicer
`servicer_payload_capacity`		Float, kg
Servicer Prop Thrust	5000.0 N	Thrust of the servicer propulsion
`servicer_prop_thrust`		Float, N
Servicer Prop Isp	320 s	Specific impulse of the servicer propulsion
`servicer_prop_isp`		Float, s
Servicer Prop Dry Mass	26.0 kg	Dry mass of servicer propulsion system
`servicer_propulsion_dry_mass`		Float, kg
Servicer Docker Dry Mass	1.1 kg	Mass of the docking module for the servicer
`servicer_docking_module_dry_mass`		Float, kg
Servicer Structural Mass	1022.9 kg	Structural mass of the servicer
`servicer_struct_mass`		Float, kg
Servicer Default Volume	24.0 m^3	Default volume of the servicer
`servicer_default_volume`		Float, m^3
Servicer Propulsion Type	Bi-propellant	Type of propulsion for the servicer
`servicer_propulsion_type`		String
Depot Initial Fuel Mass	4600.0 kg	Fuel mass at the start for the depot
`depot_initial_fuel_mass`		Float, kg
Depot Payload Capacity	3100.0 kg	Payload capacity of the depot
`depot_payload_capacity`		Float, kg
Depot Prop Thrust	4250.0 N	Thrust of the depot propulsion
`depot_prop_thrust`		Float, N
Depot Prop Isp	321 s	Specific impulse of the depot propulsion
`depot_prop_isp`		Float, s
Depot Prop Dry Mass	43.0 kg	Dry mass of the depot propulsion system
`depot_propulsion_dry_mass`		Float, kg
Depot Docker Dry Mass	1.1 kg	Mass of the docking module for the depot
`depot_docking_module_dry_mass`		Float, kg
Depot Structural Mass	3255.9 kg	Structural mass of the depot
`depot_struct_mass`		Float, kg
Depot Default Volume	160.0 m^3	Default volume of the depot
`depot_default_volume`		Float, m^3
Depot Propulsion Type	Bi-propellant	Type of propulsion for the depot
`depot_propulsion_type`		String
Propellant Transfer Rate	0.505 kg/s	Rate of propellant transfer
`propellant_transfer_rate`		Float, kg/s
Launcher Name	Ariane 64	Name of the launch vehicle
`launcher_name`		String
Launcher Launch Site	Kourou	Name of the launch site
`launcher_launch_site`		String
Launcher Orbit Type	GTO	Type of orbit for launch

Parameter	Value	Description
`launcher_orbit_type`		String
Perigee Launcher Insertion	250.0 km	Perigee altitude after insertion
`perigee_launcher_insertion`		Float, km
Inclination Launcher Insertion	6.0 °	Inclination at launch insertion
`inc_launcher_insertion`		Float, degrees
RAAN Launcher Insertion	-171.0 °	RAAN at launch insertion
`raan_launcher_insertion`		Float, degrees
Argument of Perigee Launcher Insertion	0.0 °	Argument of perigee at launch insertion
`argp_launcher_insertion`		Float, degrees
Apogee Launcher Disposal	N/A	Apogee altitude after disposal
`apogee_launcher_disposal`		Float, km
Perigee Launcher Disposal	N/A	Perigee altitude after disposal
`perigee_launcher_disposal`		Float, km
Inclination Launcher Disposal	N/A	Inclination after disposal
`inc_launcher_disposal`		Float, degrees
Apogee Infrastructure Disposal	N/A	Apogee altitude after infrastructure disposal
`apogee_infrastructure_disposal`		Float, km
Perigee Infrastructure Disposal	N/A	Perigee altitude after infrastructure disposal
`perigee_infrastructure_disposal`		Float, km
Inclination Infrastructure Disposal	N/A	Inclination after infrastructure disposal
`inc_infrastructure_disposal`		Float, degrees

Table A.7.: Scenario Parameter Details

Parameter	Value	Description
INC_FOR_RAAN_DELTA	$1 \cdot 10^{-5}$ rad	Δi adjustment for change manoeuvre
MAX_TRANSFER_COST	2000 m/s	Max. cost for one orbit change
MAX_DURATION	12.0 d	Max. duration for one orbit change
TOLERANCE_EQUAL_ORBITS_A	0.001	Tolerance for distance equivalence
TOLERANCE_EQUAL_ORBITS_ANGULAR	0.001	Tolerance for angular equivalence
TOLERANCE_EQUAL_EPOCH	1 s	Tolerance for epoch equivalence
PHASING_TOF_MIN	0.01 d	Min. time of flight for phasing
PHASING_TOF_MAX	10.0 d	Max. time of flight for phasing
PHASING_ALTITUDE_DELTA_SEARCH_FACTOR	0.5	Search factor for phasing orbit a_{max}
MINIMUM_INCLINATION_CHANGE_FOR_OPTI	0.5°	Min. Δi for optimized distribution of Δi with simultaneous Hohmann burns
TOLERANCE_AT_RANGE_BOUNDARIES	$1 \cdot 10^{-5}$ rad	Angular tolerance for range [0, 2π) rad
DEPOT_RAAN_STEPSIZE	30°	Step size for depot RAAN iteration
DEPOT_INC_STEPSIZE	1°	Step size for depot inclination iteration
DEPOT_RAAN_MAX	180°	Maximum RAAN for depot location
DEPOT_RAAN_MIN	-150°	Minimum RAAN for depot location
DEPOT_INC_MAX	0°	Maximum depot inclination
DEPOT_INC_MIN	0°	Minimum depot inclination
DOCKING_DURATION	60.0 min	Duration for docking and undocking

Parameter	Value	Description
APPROACH_DURATION	12.0 h	Duration for close proximity
APPROACH_MASS	20.0 kg	Mass consumption for close proximity
DEPOT_PAYLOAD_CAPACITY_FOR_SERVICER_REFUELLING	0.99	Percentage of depot capacity used for servicer refuelling phase
SATELLITE_DEFAULT_ISP	320 s	Default Isp of passive satellites
REFUELLING_SERVICER_FUEL_CONTINGENCY	0.0	Fuel contingency for refuelling servicer
REFUELLING_SERVICER_PROP_MODULE_MASS_CONTINGENCY	0.0	Propulsion module mass contingency for refuelling servicer
DEPOT_FUEL_CONTINGENCY	0.0	Fuel contingency for depot
DEPOT_PROP_MODULE_MASS_CONTINGENCY	0.0	Propulsion module mass contingency for depot
LAUNCHER_PAYLOAD_MASS_CONTINGENCY	0.0	Payload mass contingency for launcher

A.4. Implementation

The current version of the **Technology Combination Analysis Tool (TCAT)**, developed by the EPFL Space Center, is documented in its user manual [7]. TCAT simulates space logistics scenarios, currently focusing on ADR and constellation deployment. It supports engineers in the preliminary stages of mission design by evaluating different mission architectures and spacecraft configurations. The implementation is based on Object-Oriented Programming (OOP) in Python. This work aims to enhance TCAT's functionality by integrating an OOR scenario.

The **global architecture** of the program is depicted in Unified Modelling Language (UML) in figure A.10. The scenario is set up through user input, where a constellation of passive satellites acting as clients and a fleet of active spacecraft are defined based on the operational requirements. This setup includes specifying relevant orbits and spacecraft properties, including the visitation sequence for clients. During scenario execution, the fleet mission plan is executed. This involves configuring the required number of launch vehicles and other supporting spacecraft, such as servicers and depots, according to the scenario specifications. The spacecraft are initialized by defining their modules, which include propulsion, structure, payload, and docking systems. Once the fleet is operational, each spacecraft is assigned to service specific client satellites. The mission profile is then outlined, consisting of distinct mission phases, each associated with specific spacecraft modules. The subsequent execution of the mission plan applies each phase sequentially, modifying the state of the spacecraft and its modules, thereby simulating the entire mission progression. Upon successful simulation, KPIs and a detailed mission report are generated.

For implementation of the defined refuelling scenario and its use case, the TCAT tool is **extended with enhanced orbital transfer modelling, scenario optimization capabilities and OOR specific classes and corresponding methods**. The new orbital transfer model supports full orbital parameter modification, enabling rendezvous, whereas the previous version only allowed for Hohmann transfers, inclination changes, and RAAN adjustments via J2 drifting not applicable in GEO. Supporting a $\Delta v/\Delta t$ trade-off, a universally valid trajectory selection process is now integrated, supporting both stationary and general cases within the CompleteOrbitChange class. The execution of this phase computes and applies all manoeuvres for the selected trajectory subsequently to the spacecraft. The new OrbitChangeManoeuvre object represents an orbit

change manoeuvre consisting of multiple burns, replacing the previous class, which was limited to simple single-burn manoeuvres. For refuelling scenario optimization, iterative infrastructure design is now implemented using the described GA, optimizing logistics during scenario setup. New spacecraft classes, such as RefuellingServicer and Depot, are introduced, alongside a Launcher class designed to support missions without kick-stages. The new PayloadModule allows definition and manipulation of mission payloads, acting as propellant payload for OOR. A refuelling phase simulates fuel transfer across multiple actors and modes, and an approach phase models close-proximity operations. The existing capture phase is adapted for docking and undocking simulations. Additionally, the tool now supports a client satellite database, allowing for customizable and adaptable ClientSatellites throughout the mission. These expanded capabilities improve mission flexibilities and capabilities for logistic scenarios.

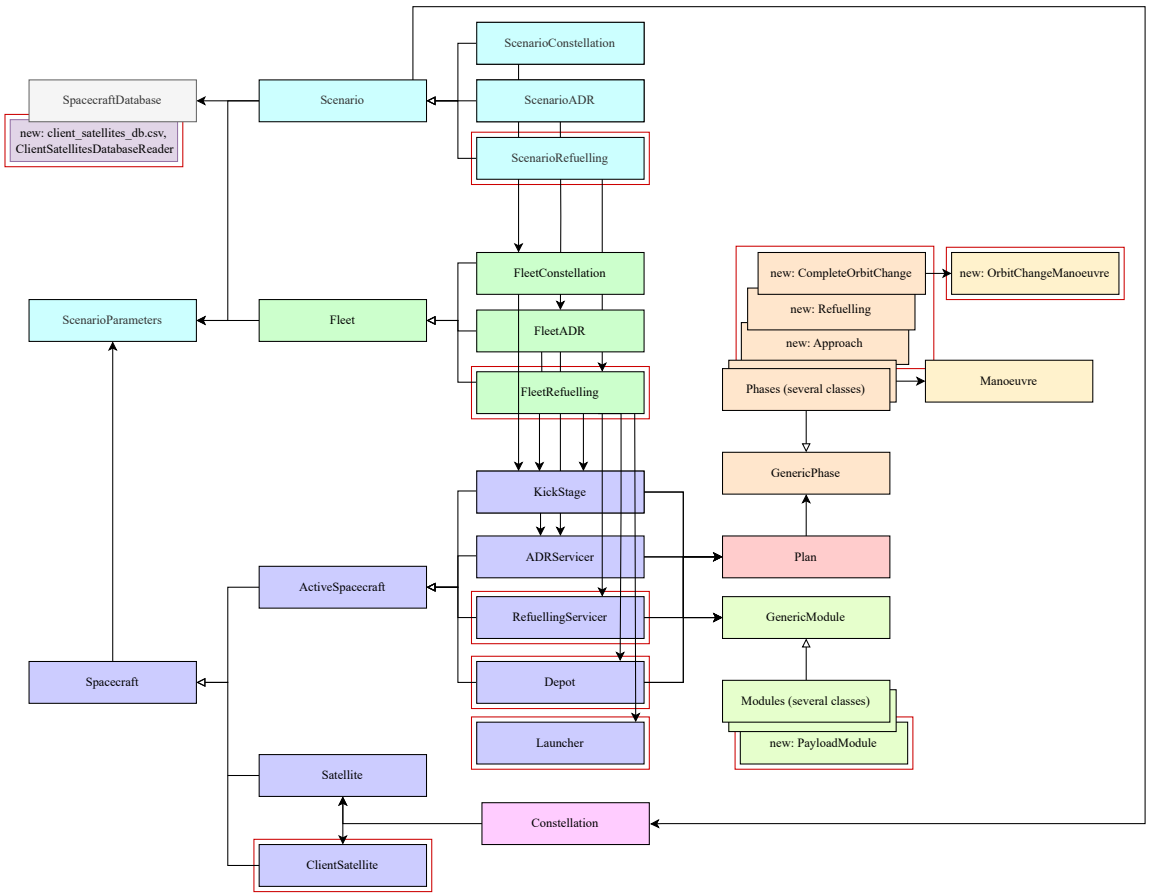

Figure A.10.: TCAT UML of Global Architecture

The entire TCAT code is in the TCAT repository on **GitHub**, in the branch *dev-*

hannah. Two external **libraries** for modelling are used. TCAT utilizes the poliastro library for astrodynamics by Massachusetts Institute of Technology [54]. Orbits are represented as Orbit objects with classical orbital elements, aligned with the definitions given within the state of the art. DEAP is a computational framework for solving evolutionary algorithms in Python employed in this work [71].

The following explanations focus specifically on the refuelling scenario, supplementing the code documentation within TCAT and the general TCAT user manual [7] to enhance clarity and understanding. The global architecture in figure A.10 shows the global **UML diagram**, with newly introduced classes highlighted in red boxes, along with their relationships as implemented in this thesis.

In the current version of TCAT for OOR, all design points are simulated for performance comparison. As a result, *RunTCAT.py*, which contains the ***main()*** method to run the tool, includes iterations over the depot orbit Ω, with boundaries and step sizes defined in the ScenarioParameter specifications. Iteration through inclined depot orbits is also implemented. To incorporate inclined orbits, the inclination boundary parameters are to be adjusted to the desired range. In an inner loop, the method iterates over the number of servicers, ranging between the minimum and maximum values calculated and refined during the scenario setup. A ScenarioRefuelling represents a unique combination of design variables, a specific design point defined by the depot orbit and the number of servicers, resulting in a distinct OOR architecture design. Consequently, the execution of the scenario and mission simulation corresponds exclusively to one of these unique design configurations.

The **ScenarioRefuelling** in UML A.11 represents the entire scenario setup and execution. The ScenarioRefuelling *setup()* reads the client satellite database to create an individual ClientSatellite object for each client as indicated in figure A.14. The propellant mass of the client satellite is then updated to reflect its value at the starting time of the refuelling mission in GEO. The updated clients are finally added to the Constellation instantiated before. Moreover, within the scenario setup, the fleet is defined. The *define_fleet()* method contains, most importantly, the logistics optimization. *optimize_fleet()* solves the VRP for the scenario, which corresponds to an individual design point. To improve computational efficiency, the logistics optimization process is performed for all numbers of servicers within one depot location in an initial step for the minimum number of servicers. Thanks to this approach, the transfer matrix is computed only once

for the optimization problem. The results are saved for all fleet sizes, and then loaded from the existing results data for subsequent design points. *solve_VRP_for_scenario()* thus solves the VRP for all numbers of servicers, and saves the corresponding results. Iterating through the numbers of servicers, *optimize_logistics_scenario()* executes the actual optimization, returning the best route and all its properties. It contains the methods for defining and solving the VRP. *define_VRP()* formulates the VRP to solve, including individual client demands of constellation satellites, capacities and transfer matrices computed specific to the current depot location. The cost matrix computation involves computing all orbital transfers between all nodes within the logistics network. The genetic algorithm is implemented within the *solve_VRP()* method.

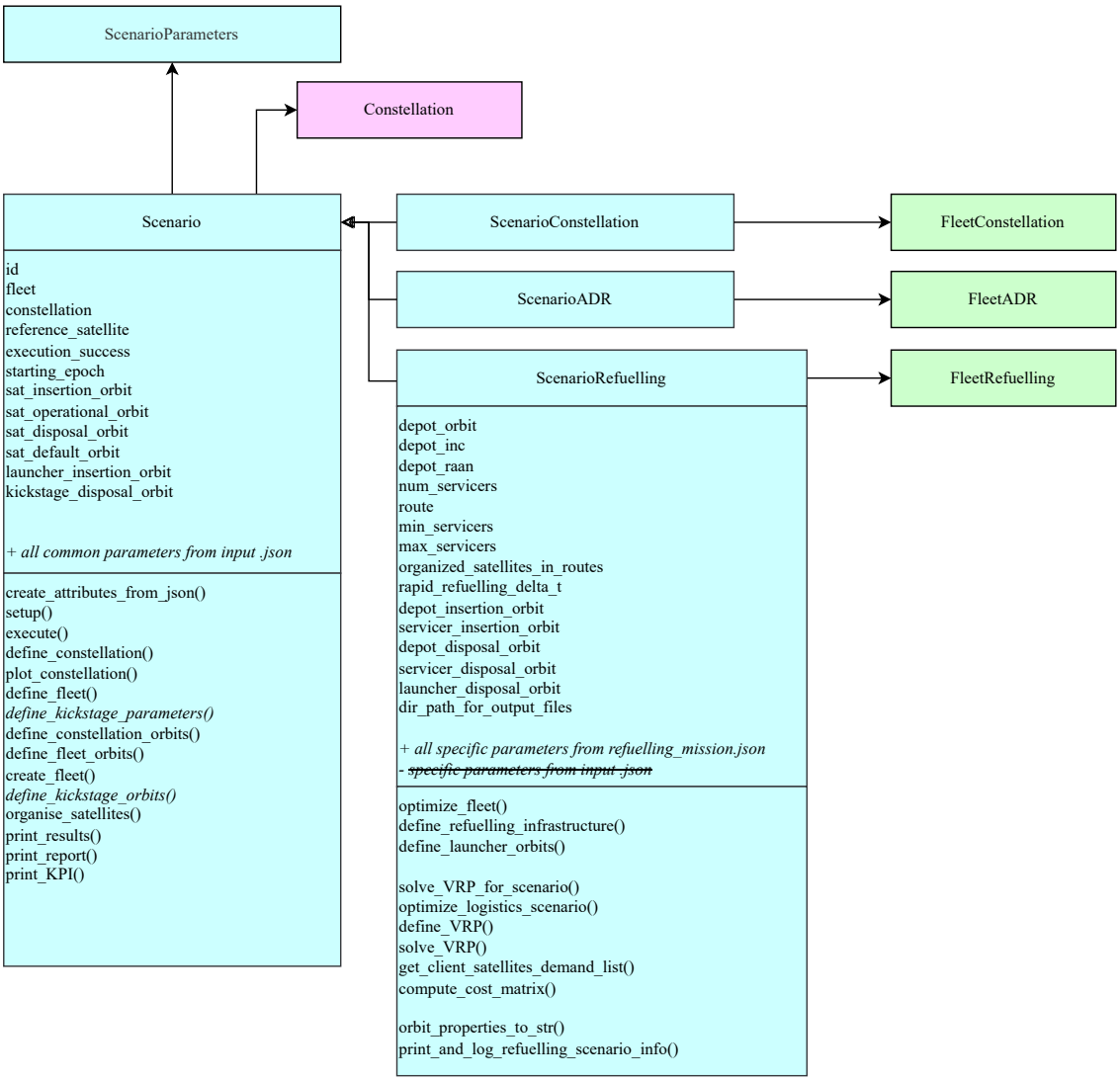

Figure A.11.: TCAT UML of ScenarioRefuelling Class

Execution of the scenario calls execution of the fleet following figure A.12. A **FleetRefuelling** consists of a dictionary of servicers, depots and launchers. In the defined use case, only one depot is relevant. The fleet contains as many servicers as the current design point prescribes. The *execute()* method further computes and creates the required numbers of launchers taking into account allowances in terms of payload mass and fairing volume constraints. The computation of all KPIs is also implemented herein, as only at this level, all spacecraft information are available. Within the fleet, all individual spacecraft *execute()* methods are called.

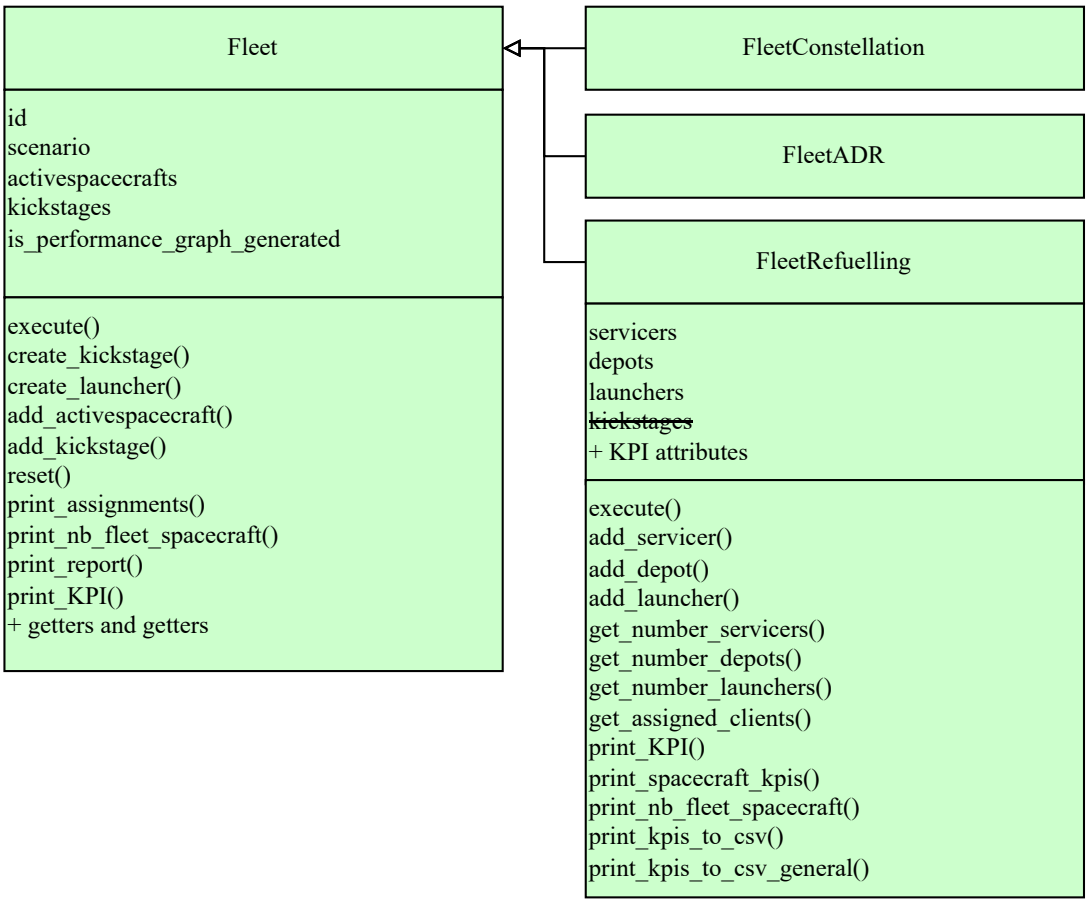

Figure A.12.: TCAT UML of FleetRefuelling Class

The spacecrafts and launcher that make up the fleet are defined as classes for **RefuellingServicer, Depot and Launcher** in figure A.13. A novel class of **ClientSatellite** objects is created to allow for modification of client satellite properties and interaction with its modules. This is specifically required for refuelling the propulsion module and for tracking and updating its propellant levels. Spacecraft now includes a **PayloadModule**,

which represents the propellant designated for refuelling other satellites in this scenario. It is readily extendable to other scenario which require payload definitions. The active spacecrafts, RefuellingServicer and Depot, follow their individual mission plan as described in figure 3.1. The individual phases are defined within the *define_mission_profile()* method, with comments provided within the method for clarity. Finally, executing the spacecraft applies the mission plans, applying each phase sequentially for each spacecraft.

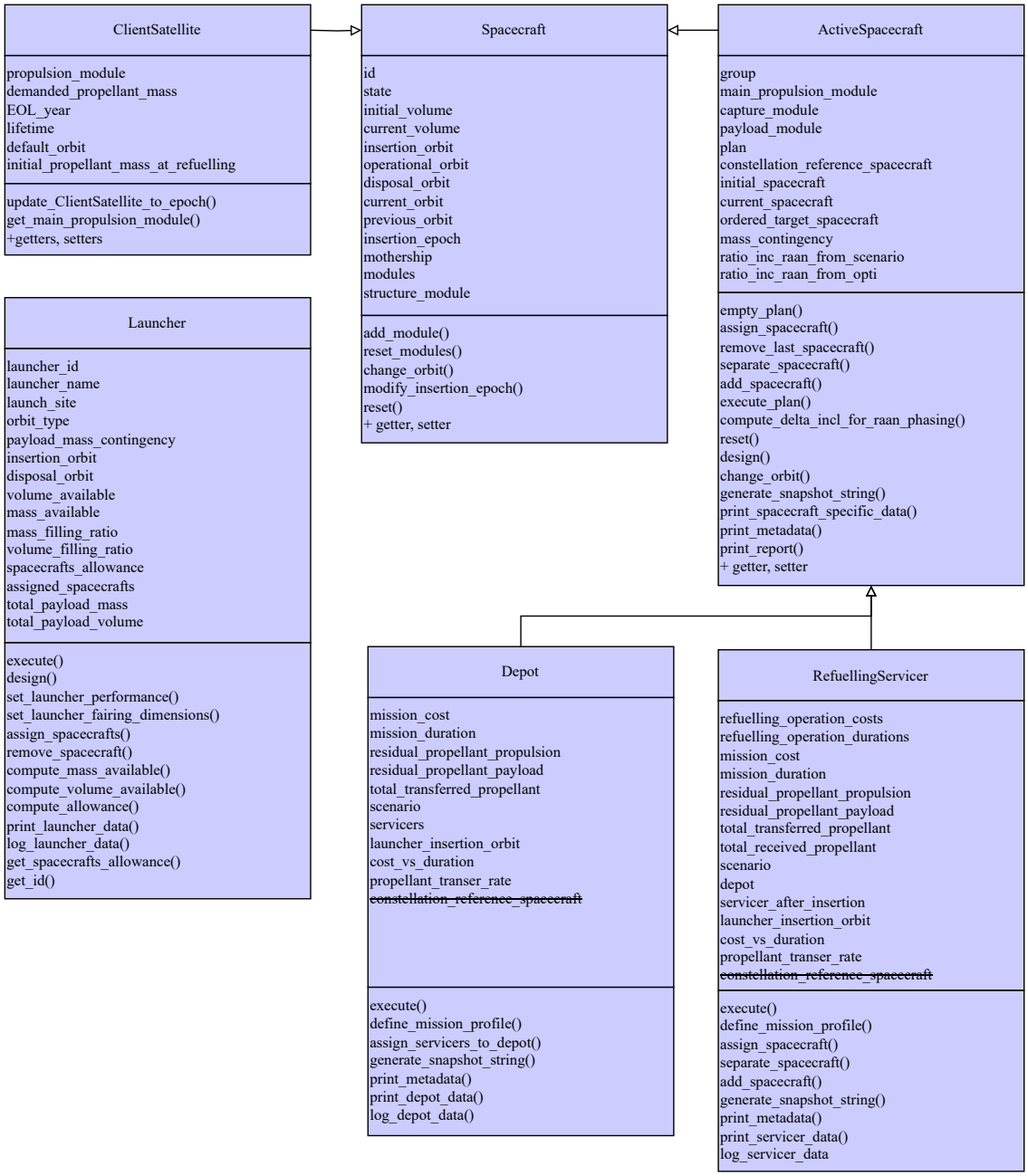

Figure A.13.: TCAT UML of Spacecrafts and Launcher Classes

Figure A.14 presents the handling of **client satellite data**. Database inputs comprise ID, name, RAAN, h_p, h_a, e, i, m_0, m_p, and EOL. Other relevant properties, such as orbit, propellant demand, and fuel level, are computed using methods from the ClientSatellites-DatabaseReader class.

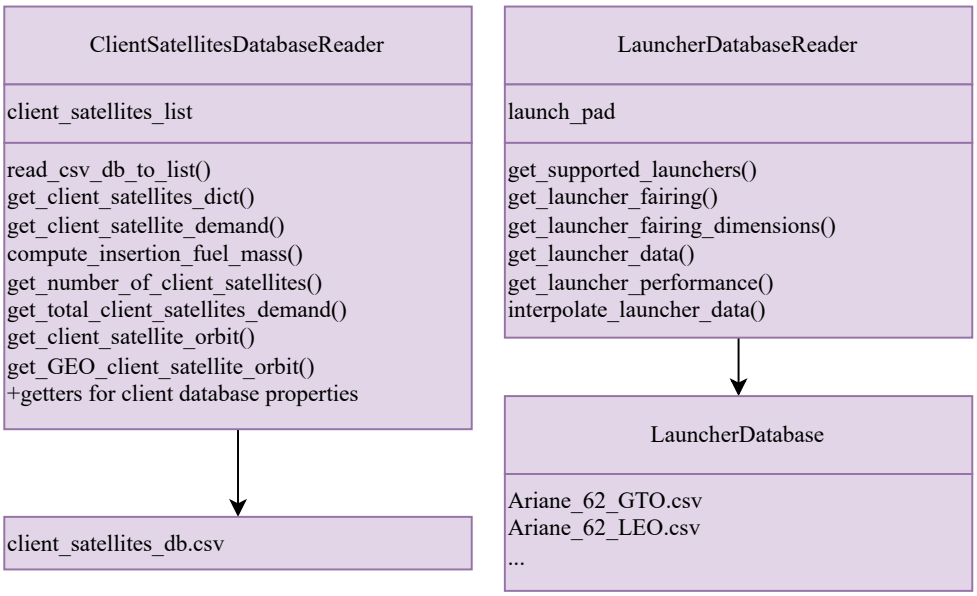

Figure A.14.: TCAT Database Handling

The plan of each ActiveSpacecraft is composed of **phases**. The phases required for the OOR scenario are outlined in figure A.15.

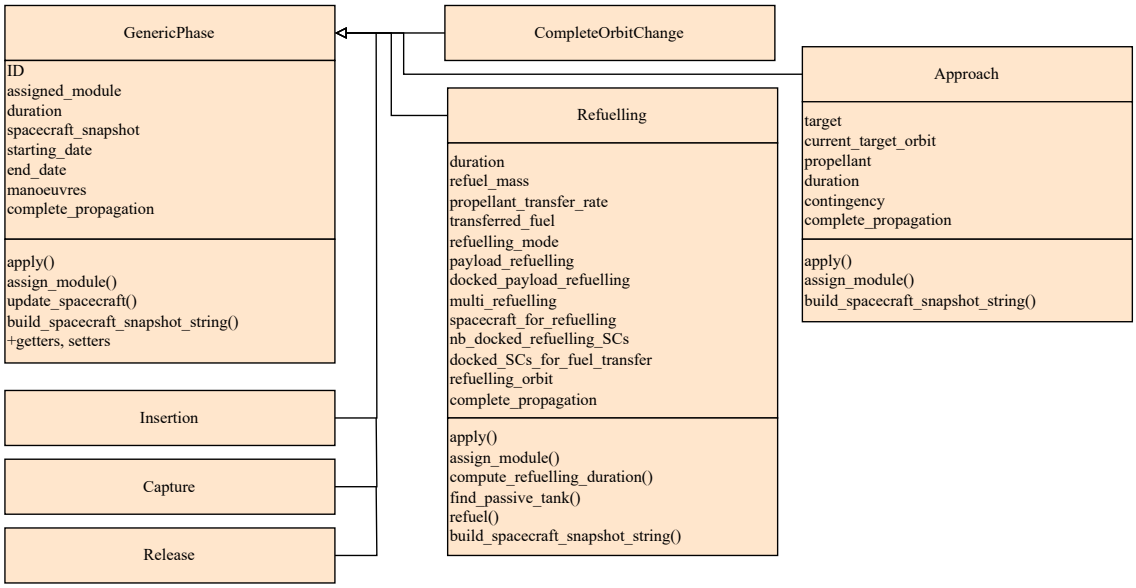

Figure A.15.: TCAT UML of Phases

The **Refuelling phase** is specific to the OOR scenario, allowing for flexible definition of the refuelling mode. Both O2O refuelling and parallel refuelling of multiple spacecraft are possible. During the process, active tanks are emptied while passive tanks are filled, making the phase applicable to both refuelling and being refuelled. Additionally, it must be specified whether propulsion or payload tanks are utilised as modules in this phase. The **Approach phase** represents close-proximity manoeuvres, approximated by constant duration and propellant consumption attributed to the propellant module. Docking and undocking are modelled using the existing Capture and Release phases. The developed orbital dynamics for modelling orbit changes are utilised within the CompleteOrbitChange phase in figure A.16, managing orbit changes with rendezvous.

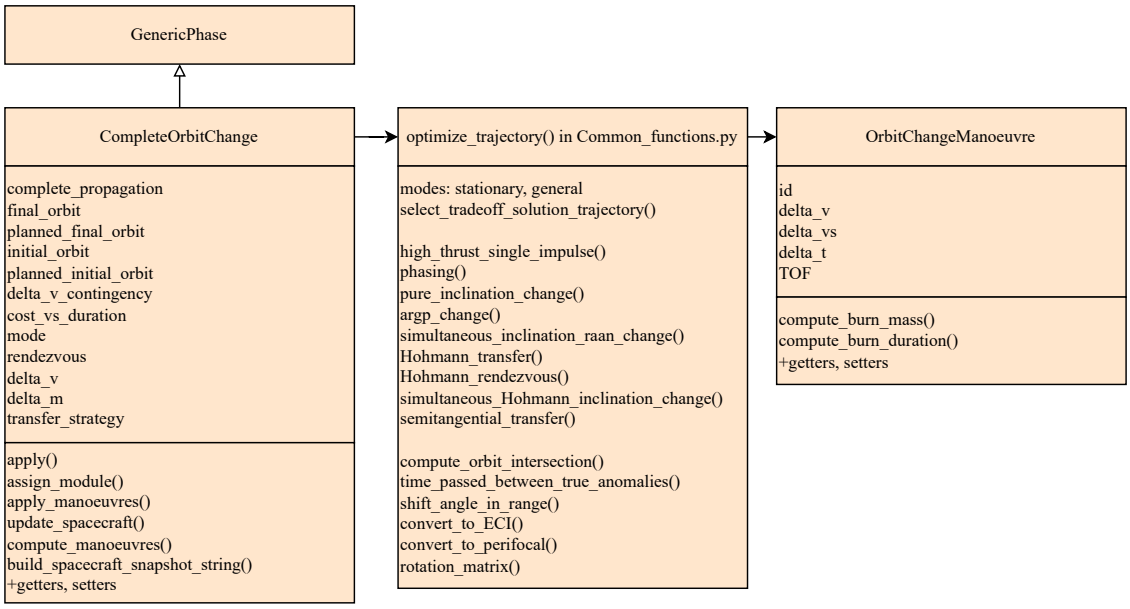

Figure A.16.: Implementation of Trajectory Selection and Orbit Change Manoeuvres

To conduct a **CompleteOrbitChange** between two spacecraft orbits for rendezvous, the trajectory must be defined as described in chapter 3.2.3. Applying the phase implies *apply_manoeuvres()*, which calls *compute_manoeuvres()*, ultimately invoking the trajectory selection method *optimize_trajectory()*. The required inputs include the initial and final orbits, the cost-duration trade-off parameter $p_{\Delta v/\Delta t}$, the trajectory mode (specified as either stationary or general), and an indication of whether rendezvous is required. The trajectory selection method *optimize_trajectory()* strictly adheres to the specified options and manoeuvre sequences: In stationary mode, it precisely follows the trajectory and manoeuvre sequences detailed in figure A.8. Figure A.9 illustrates the general trajectory

design mode. Within the OOR scenario, the stationary mode is applicable for all orbit changes except GEO insertion from GTO.

The strategy is selected using the *select_tradeoff_solution_trajectory()* method representing equation (3.14). *optimize_trajectory()* returns Δv, transfer duration for the entire orbit change including all individual transfer durations and waiting durations, a list of the transfer manoeuvres, and the selected transfer strategy notion. Each individual manoeuvre method returns Δv, Δv_1, Δv_1, transfer duration, waiting duration to transfer initiation, arrival orbit, and the corresponding OrbitChangeManoeuvre. The new **OrbitChangeManoeuvre** object represents an orbit change manoeuvre consisting of multiple burns, replacing the previous class, which was limited to simple single-burn manoeuvres. The computations adhere to detailed transfer manoeuvres for changes of all orbital parameters in chapter 3.2.2. The newly implemented transfer manoeuvres available in TCAT are as follows:

- Single impulse high thrust manoeuvres *high_thrust_single_impulse()* that require finding an intersection between orbits. The optimization for orbit intersection is contained in *compute_orbit_intersection()*.
- Phasing manoeuvres taking into account $p_{\Delta v/\Delta t}$ in the selection from discrete phasing solutions for rendezvous of spacecrafts. The corresponding method, *phasing()*, also provides a graphical representation of the solution space in its individual application.
- Out-of-plane changes with simultaneous change of RAAN and inclination *simultaneous_inclination_raan_change()*, and the specific case of a pure inclination change *pure_inclination_change()*.
- Hohmann transfer including the selection of the most efficient transfer option at apogee or perigee for $p_{\Delta v/\Delta t}$ implemented within *Hohmann_transfer()*. Plotting of solutions is also available herein. Variants of the Hohmann transfer are additionally implemented.
- For simultaneous change of true anomaly for rendezvous *simultaneous_Hohmann_inclination_change()* computes the transfer.
- *simultaneous_Hohmann_inclination_change()* applies in-plane and out-of-plane manoeuvres simultaneously at Hohmann burn points. For angles above a specified value defined within ScenarioParameters `MINIMUM_INCLINATION_CHANGE_FOR_OPTI`,

now at 0.5°, the inclination change distribution among the two impulses is optimized.

- Semitangential transfer manoeuvres for rendezvous at lower duration and higher Δv are additionally implemented within *semitangential_transfer()*. The implementation, based on computations from the literature, produces results that could not be verified here and therefore raise doubts about its accuracy. Consequently, this option is excluded from the trajectory selection method in the current version of OOR implementation in TCAT.

The methods further contain a check of requirements that need to be fulfilled in order for the manoeuvre to be applicable as detailed in chapter 3.2.2. Otherwise the manoeuvre methods return None values. All methods have been verified either through hand calculations or by cross-checking identical orbit changes using validated methods.

A.5. Results

Figure A.17 presents the duration matrix corresponding to cost matrix 4.6 for describing optimized routes of four servicing vehicles for the depot location at $\Omega = 0°$.

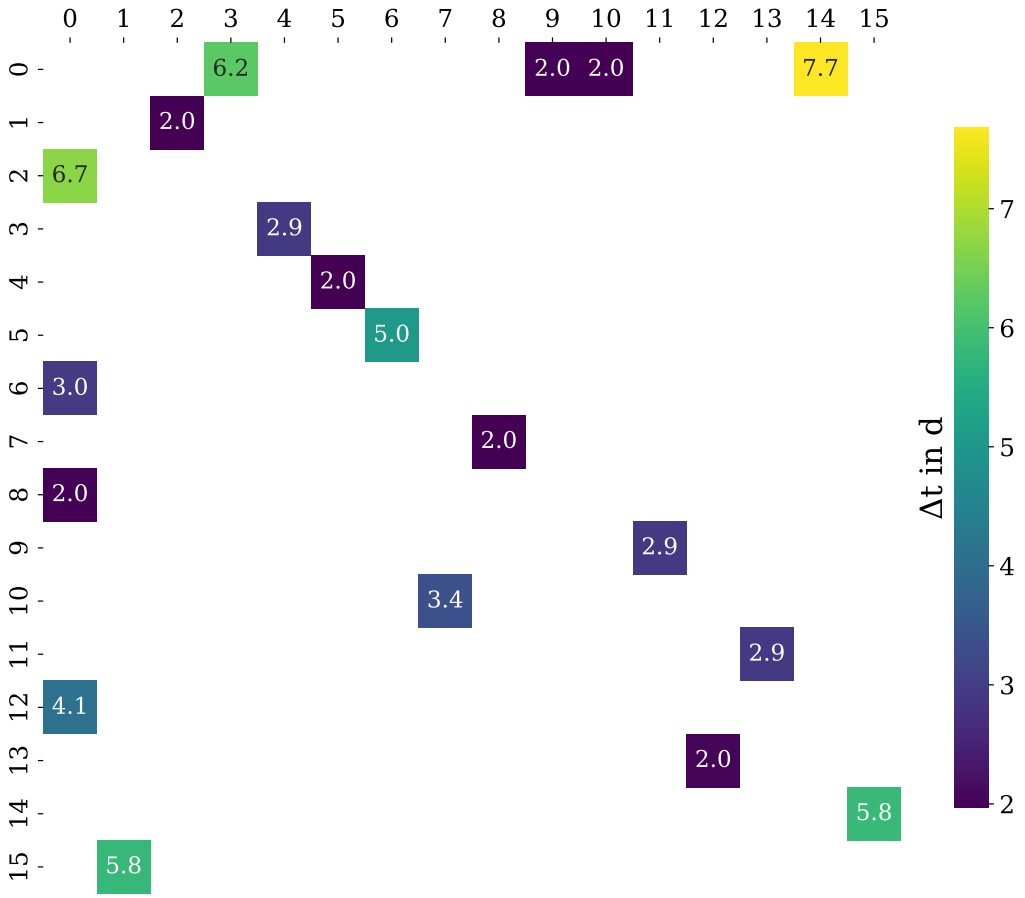

Figure A.17.: Selected Route Durations for 4 Servicers, with $p_{\Delta v/\Delta t} = 0.1$ and $\Omega = 0°$

Figure A.18 presents the cost and duration matrices as well as performance results obtained with complete cost priority in parameter $p_{\Delta v/\Delta t} = 0.0$. Total mission durations are close to or exceed $\mathrm{TOF}_{\max} = 10\,\mathrm{d}$ staying below the maximum transfer duration of 12 d always.

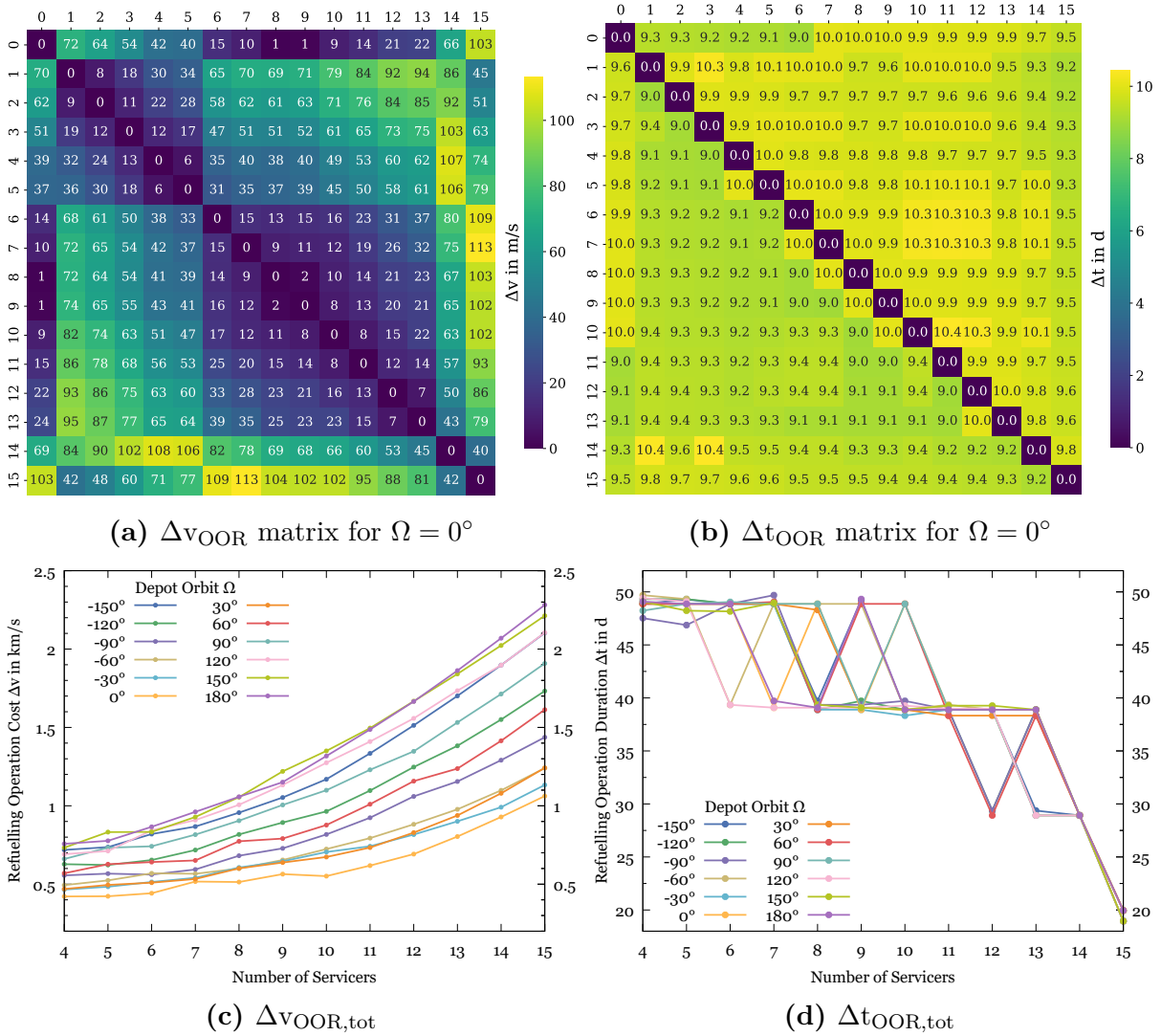

(a) Δv_{OOR} matrix for $\Omega = 0°$

(b) Δt_{OOR} matrix for $\Omega = 0°$

(c) $\Delta v_{\mathrm{OOR,tot}}$

(d) $\Delta t_{\mathrm{OOR,tot}}$

Figure A.18.: Transfer Matrices and OOR Cost and Duration for different Architecture Design Points, with cost priority $p_{\Delta v/\Delta t} = 0.0$

Figure A.19 presents the cost and duration matrices as well as performance results obtained with cost duration trade-off parameter $p_{\Delta v/\Delta t} = 0.3$ selecting faster transfers at the expense of cost compared to the defined parameter in this study.

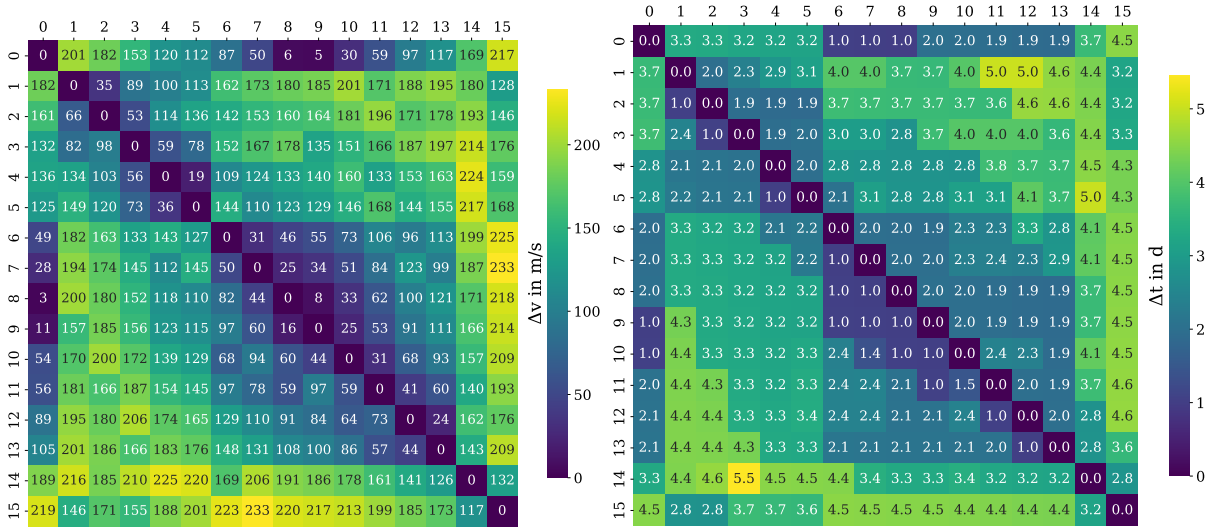

(a) Δv_{OOR} matrix for $\Omega = 0°$ **(b)** Δt_{OOR} matrix for $\Omega = 0°$

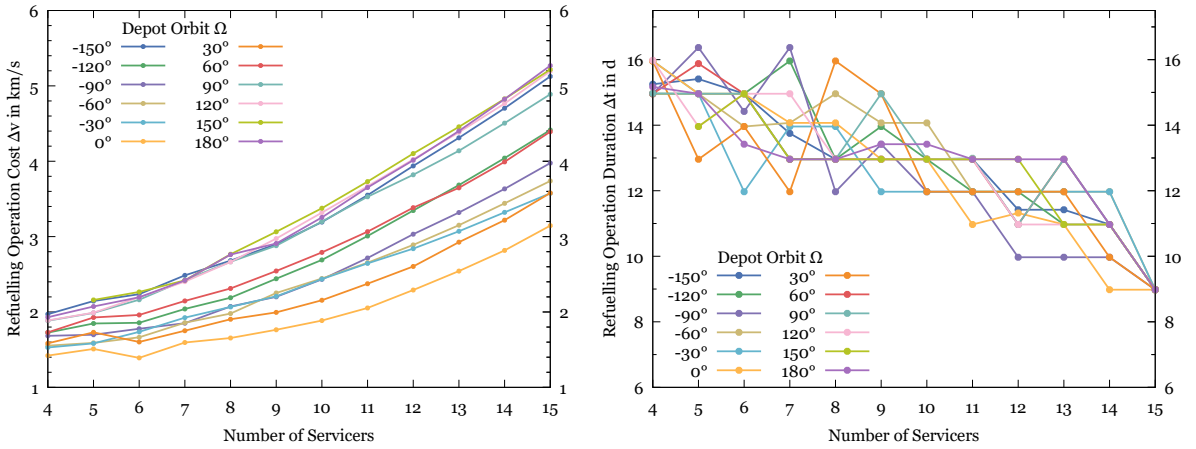

(c) $\Delta v_{OOR,tot}$ **(d)** $\Delta t_{OOR,tot}$

Figure A.19.: Transfer Matrices and OOR Cost and Duration for different Architecture Design Points, with cost priority $p_{\Delta v/\Delta t} = 0.3$

Figure A.20 shows the development of refuelling operation servicer duration statistics across different depot locations.

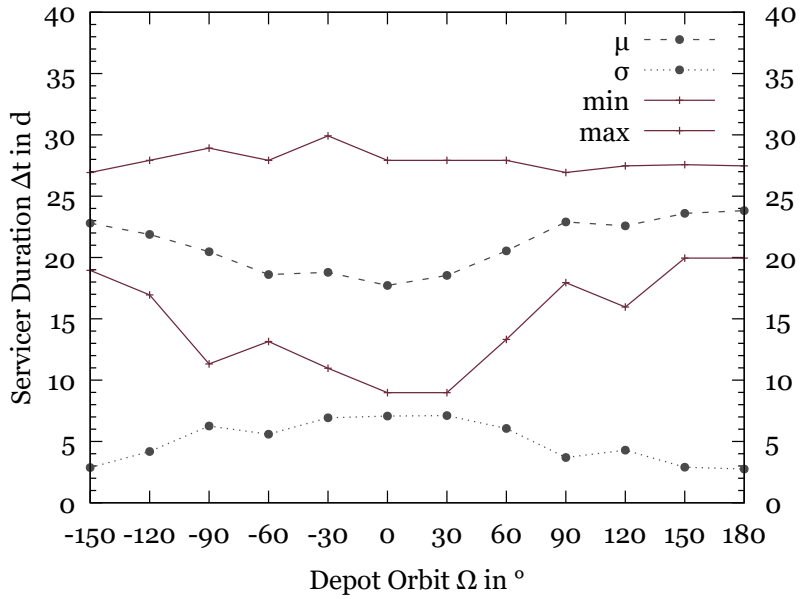

Figure A.20.: Servicer Statistics for Refuelling Operation Duration $\Delta t_{OOR,tot}$ for 4 Servicers

Figure A.21 gives information on overall remaining residual propellant mass in payload and propulsion tanks of servicers for different depot locations.

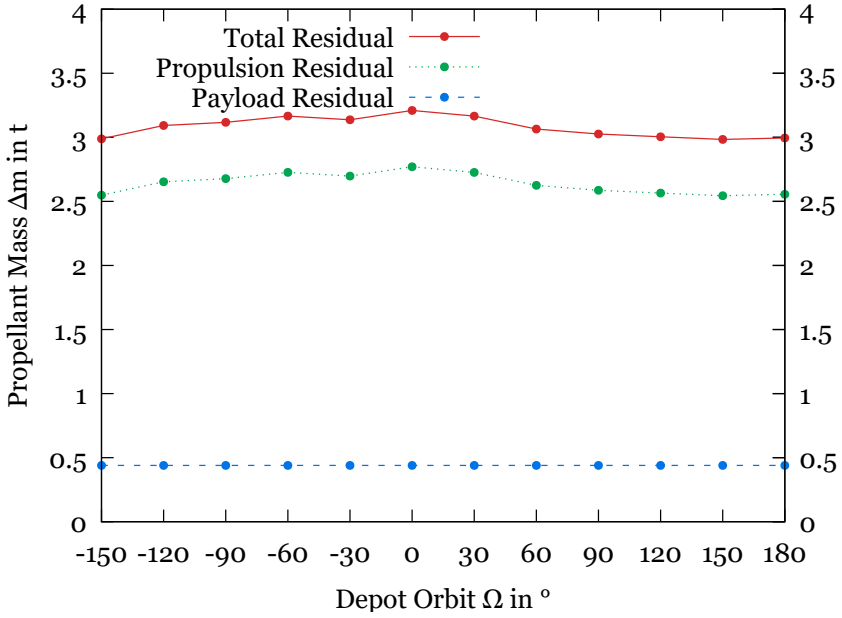

Figure A.21.: Overall Mission Residual Propellant Mass for 4 Servicers

Figure A.22 presents the results after first depot location refinement for $\Omega \in [-30°, 30°]$ with a step size of $\Delta\Omega = 10°$.

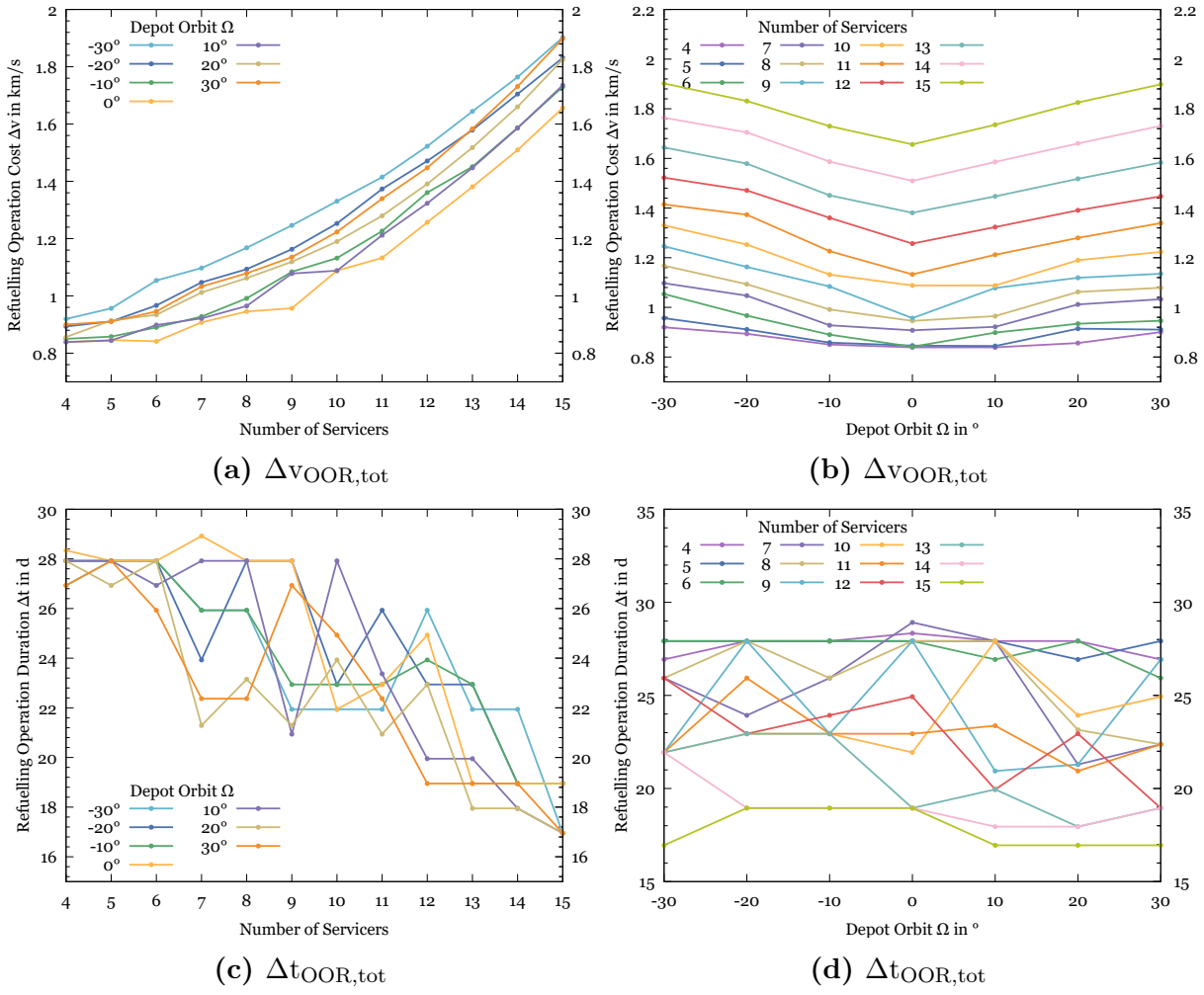

(a) $\Delta v_{OOR,tot}$ **(b)** $\Delta v_{OOR,tot}$

(c) $\Delta t_{OOR,tot}$ **(d)** $\Delta t_{OOR,tot}$

Figure A.22.: Refuelling Operation Performance for Refined Depot $\Omega \in [-30°, 30°]$

Figure A.23 presents the results after second depot location refinement for $\Omega \in [-10°, 10°]$ with a step size of $\Delta\Omega = 5°$.

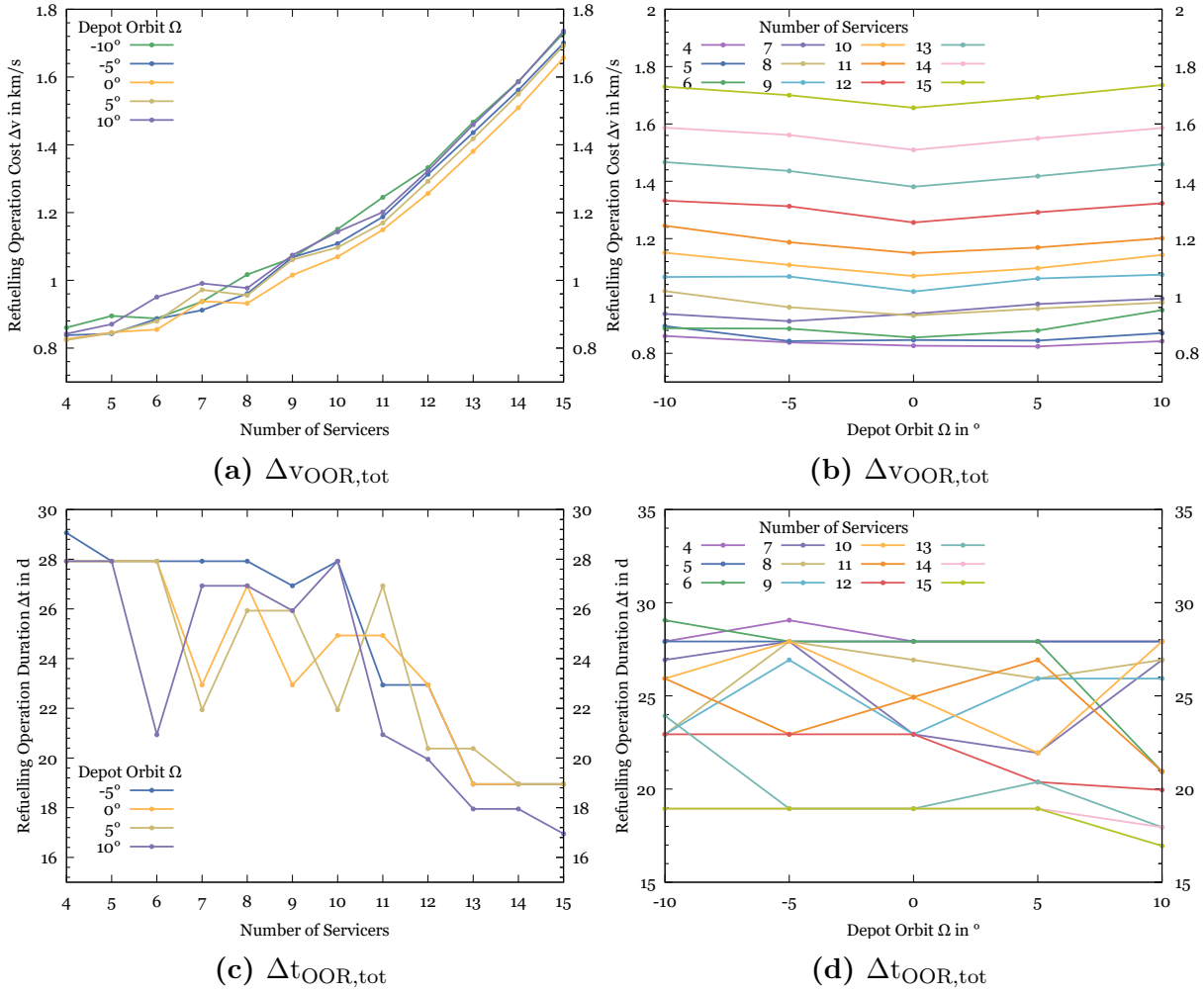

(a) $\Delta v_{OOR,tot}$ **(b)** $\Delta v_{OOR,tot}$

(c) $\Delta t_{OOR,tot}$ **(d)** $\Delta t_{OOR,tot}$

Figure A.23.: Refuelling Operation Performance for Refined Depot $\Omega \in [-10°, 10°]$

Figure A.24 presents the results after final depot location refinement for $\Omega \in [-5°, 5°]$ with a step size of $\Delta\Omega = 1°$ plotted over different numbers of servicers.

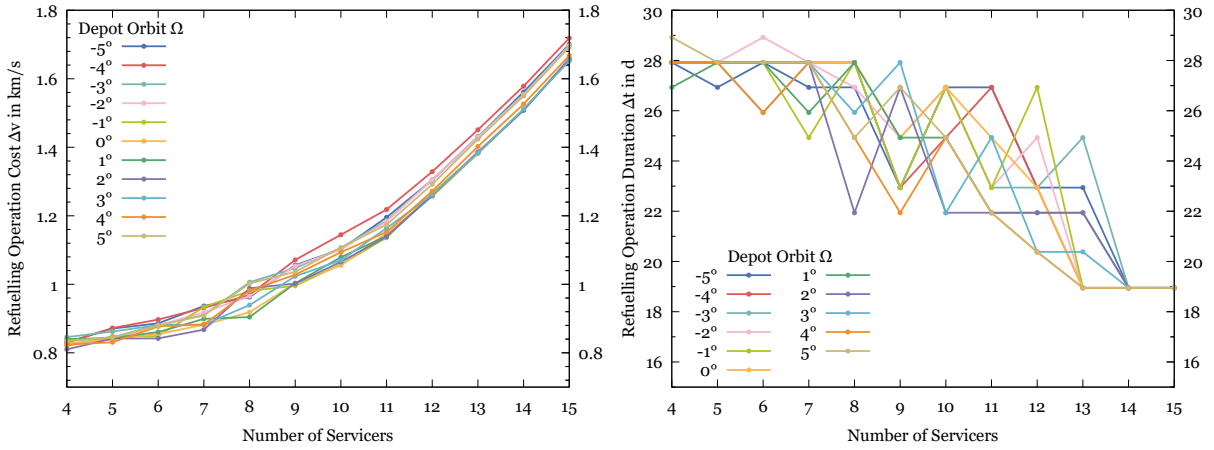

(a) $\Delta v_{OOR,tot}$ **(b)** $\Delta t_{OOR,tot}$

Figure A.24.: Refuelling Operation Cost and Duration for Refined Depot $\Omega \in [-5°, 5°]$

Figure A.25 presents the results after final depot location refinement for $\Omega \in [-5°, 5°]$ with a step size of $\Delta\Omega = 1°$ with increase population size in the GA.

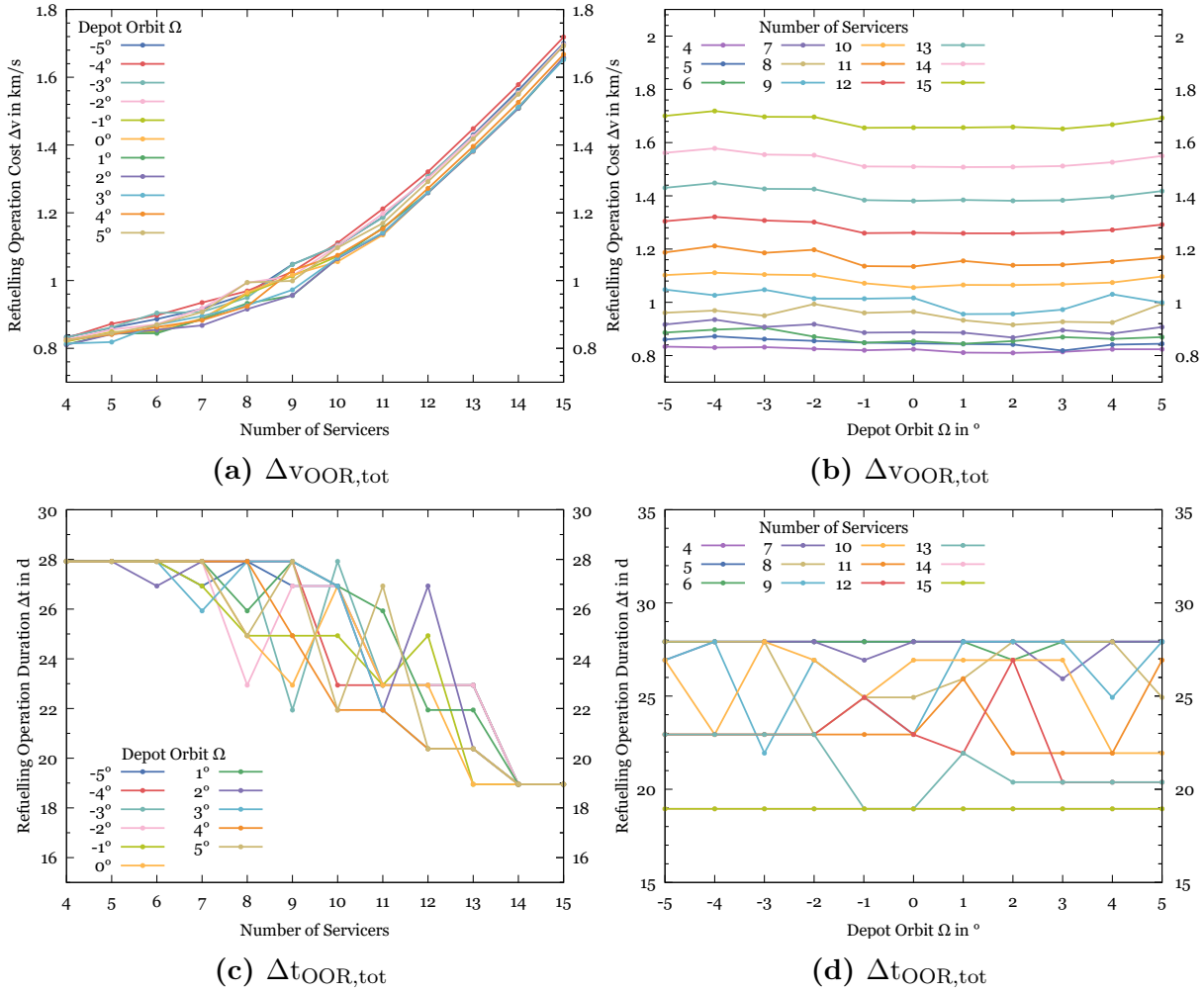

(a) $\Delta v_{OOR,tot}$ **(b)** $\Delta v_{OOR,tot}$

(c) $\Delta t_{OOR,tot}$ **(d)** $\Delta t_{OOR,tot}$

Figure A.25.: Refuelling Operation Performance for Refined Depot $\Omega \in [-5°, 5°]$ and Increased GA Population Size

A.6. Contribution to ESA Clean Space Days 2024

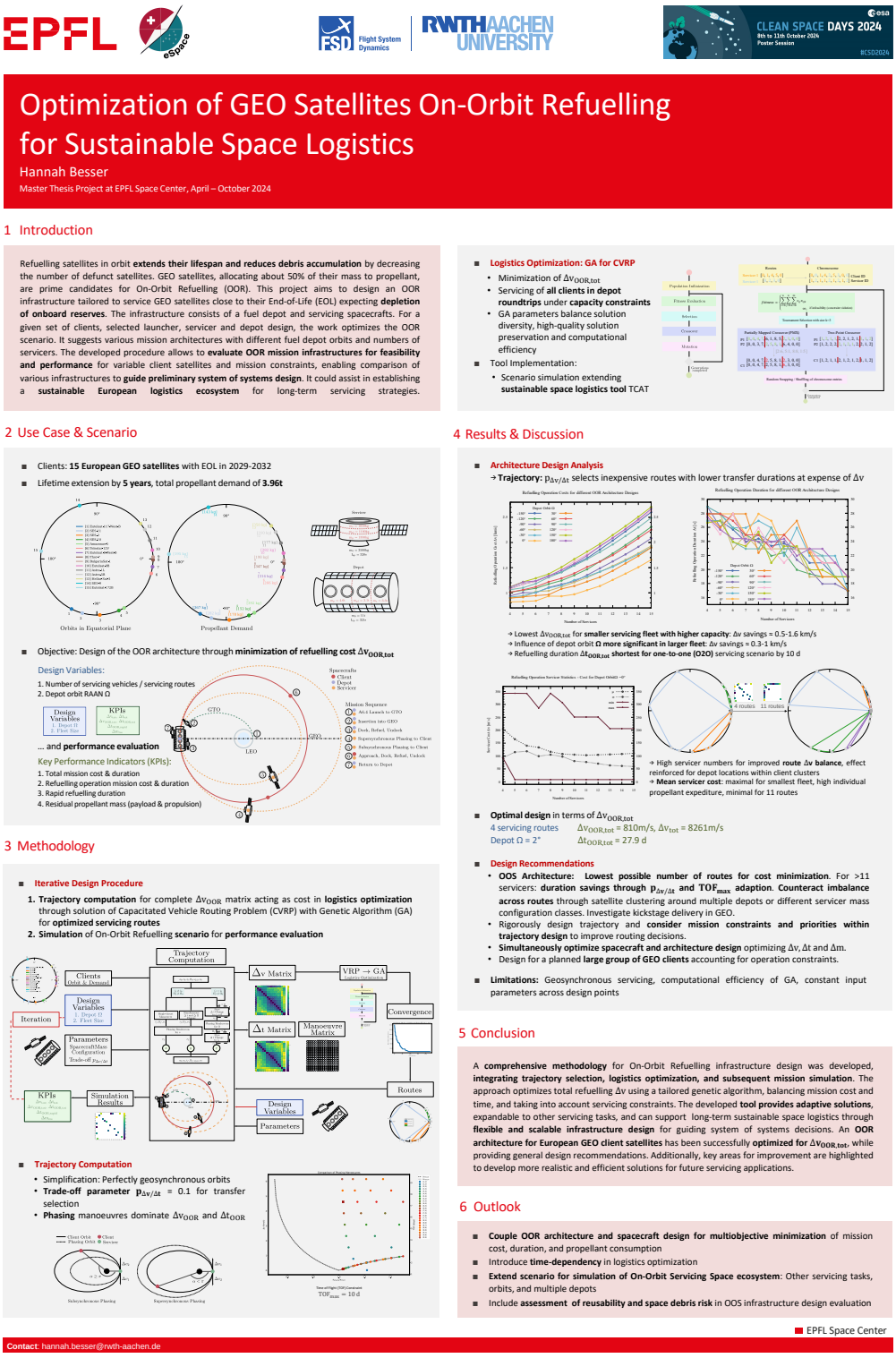

Figure A.26.: Poster Contribution to ESA CSD24

Bibliography

[1] Alfriend, K.; Lee, D.; Creamer, G.: Optimal Servicing of Geosynchronous Satellites. Journal of Guidance, Control, and Dynamics, Vol. 29, pp. 203–206, 2006.

[2] arianegroup Orbital Propulsion: Chemical Bi.Propellant Thrust Family. 10N, 200N, 400N. Datasheet, 2021.

[3] arianespace: Ariane 6 User's Manual. User's Manual, 2021.

[4] Arney, D.; Mulvaney, J.; Williams, C.; Stockdale, C.; Gelin, N.; Le Gouellec, P.: In-space Servicing, Assembly, and Manufacturing (ISAM) State of Play. 2023 Edition, 2023.

[5] Bo, X.; Feng, Q.: Research on constellation refueling based on formation flying. Acta Astronautica, Vol. 68, No. 1, pp. 1987–1995, 2011.

[6] Bourjolly, J.; Gurtuna, O.; Lyngvi, A.: On–orbit servicing: a time–dependent moving–target traveling salesman problem. International Transactions in Operational Research, Vol. 13, pp. 461–481, 2006.

[7] Brancato, F.; Udriot, M.: EPFL Space Center's DAWN. Technical Note 4: User Manual. User Manual, 2022.

[8] Breteau, J.; Tincelin, Y.; Scheper, M.; Zeller, S.; Ferreira, E.; Jasjukevics, A.; Antonetti, S.; Palun, A.; Hassin, J.; Terekhova, M.; Uwarowa, I.: In-Space Transportation Club Session #1: Docking. In-Space Transportation Club. Speech, Feb. 21, 2024.

[9] Bultitude, J.; Burkhardt, Z.; Harris, M.; Jelderda, M.; Suresh, S.; Fettes, L.; Faber, D.; Schiel, J.; Cho, J.; Levitt, D.: Development and Launch of the World's First Orbital Propellant Tanker. In: 35th Small Satellite Conference (SSC), SSC, The Aerospace Corporation, 2021.

[10] Cafini, R.; Caramelli, F.; Rinalducci, A.; Truscelli, G.: The Space Rider System key-role as European reusable IOS platform. 2024 ESA Clean Space Days Space Transportation. Speech, 2024.

[11] Caiazzo, A.: In-Orbit Servicing and Circular Economy. Clean Space Days 2024 Introduction Session Presentation, 2024.

[12] Caswell, D.; Visentin, G., Ortega, G.; Kam, J. de; Nugteren, P.; Scholten, H.: ConeXpress Orbital Life Extension Vehicle. A Commercial Service for Communications Satellites. Bulletin, esa bulletin 127, 2006.

[13] Chen, H.; Ho, K.: Integrated Space Logistics Mission Planning and Spacecraft Design with Mixed-Integer Nonlinear Programming. Journal of Spacecraft and Rockets, Vol. 55, No. 2, pp. 365–381, 2018.

[14] Chen, X.; Yu, J.: Optimal mission planning of GEO on-orbit refueling in mixed strategy. Acta Astronautica, Vol. 133, pp. 63–72, 2017.

[15] Chobotov, V.: Orbital Mechanics. Third Edition, Reston, Virginia (USA): American Institute of Aeronautics and Astronautics (AIAA), ISBN 1-56347-537-5, 2002.

[16] ClearSpace: ENCORE – In-Orbit Servicing of an Operational Spacecraft. Executive Summary Report, CS–ESA–ENC–PRL–002, 2022.

[17] Curtis, H.: Orbital Mechanics for Engineering Students. Chapter 6: Orbital Maneuvers, Butterworth-Heinemann, 2014.

[18] Daneshjou, K.; Mohammadi-Dehabadi, A.; Bakhtiari, M.: Mission planning for on-orbit servicing through multiple servicing satellites: A new approach. Advances in Space Research, Vol. 60, pp. 1148–1162, 2017.

[19] Du, B.; Zhao, Y.; Dutta, A.; Yu, J.; Chen, X.: Optimal scheduling of multi-spacecraft refueling based on cooperative maneuver. Advances in Space Research, Vol. 55, pp. 2808–2819, 2015.

[20] Du Sarton Jonchay, T.; Chen, H.; Gunasekara, O.; Ho, K.: Framework for Modeling and Optimization of On-Orbit Servicing Operations under Demand Uncertainities. Journal of Spacecraft and Rockets, Vol. 58, No. 4, 2021.

[21] Dutta, A.: Optimal Cooperative and Non-Cooperative Peer-to-Peer Maneuvers for Refuellign Satellites in Circular Constellations. PhD thesis, 2009.

[22] Dutta, A.; Tsiotras, P.: Asynchronous Optimal Mixed P2P Satellite Refueling Strategies. The Journal of the Astronautical Sciences, Vol. 54, No. 3, pp. 543–565, 2006.

[23] Ehn, E.: Mutidisciplinary Architectural Study of On-Orbit Space Vehicle Refueling. Master thesis, 2022.

[24] ESA Space Debris Office: ESA's Annual Space Environment Report. Report, GEN-DB-LOG-00288-OPS-SD, 2023.

[25] ESA Space Debris Office: ESA's Annual Space Environment Report, GEN-DB-LOG-00288-OPS-SD, 2024.

[26] ESA Space Rider Team: Space Rider User Guide. Technical Note (TN), ESA-STS-SR-TN-2018-0002, 2023.

[27] European Space Agency: ESA moves ahead with In-Orbit Servicing missions, https://www.esa.int/Enabling_Support/Preparing_for_the_Future/Discovery_and_Preparation/ESA_moves_ahead_with_In-Orbit_Servicing_missions2 (accessed 05/08/2024), 2023.

[28] European Space Agency: ESA to build first in-orbit servicing mission with D-Orbit, https://www.esa.int/Space_Safety/ESA_to_build_first_in-orbit_servicing_mission_with_D-Orbit (accessed 10/17/2024), 2024.

[29] European Space Agency: ESA's In-Space Transportation Club Highlights Advanced Dockign Interfaces, https://commercialisation.esa.int/2024/09/esas-in-space-transportation-club-highlights-advanced-docking-interfaces/ (accessed 10/18/2024), 2024.

[30] Forbes, S.: Robotic Servicing of Geosynchronous Satellites (RSGS), https://www.darpa.mil/program/robotic-servicing-of-geosynchronous-satellites (accessed 10/18/2024).

[31] Garcia, M.: Visiting Vehicles, https://www.nasa.gov/international-space-station/space-station-visiting-vehicles/ (accessed 08/22/2024), Aug. 17, 2024.

[32] Geiman, C.; Burkhardt, Z.; O'Leary, A.; Case, K.; Bultitude, J.; Kendall-Bell, G.; Spessert, E.; Faber, D.: A Shuttle and Depot Architecture for Reliable and Cost-Effective Refueling Operations in All Orbits. In: 73rd International Astronautical Congres (IAC), IAC, International Astronautical Federation, 2022.

[33] Gollins, N.; Ho, K.: Hierarchical Framework for Space Exploration Campaign Schedule Optimization. Journal of Spacecraft and Rockets, 2024.

[34] Gollins, N.; Shimane, Y.; Ho, K.: Translunar Logistics with Low-Energy Transfers. In: AAS/ AIAA Astrodynamics Specialist Conference, Astrodynamics Specialist Conference, American American Astronautical Society; Institute of Aeronautics and Astronautics, 2023.

[35] Gürtuna, Ö.; Trépanier, J.: On-Orbit Satellite Servicing: A Space-Based Vehicle Routing Problem. In: Operations Research in Space and Air. Applied Optimization. New York: Springer-Science+Business Media, B.V., pp. 123–141, ISBN 978-1-4020-1218-1, (cit. on pp. 1, 7–12, 22, 93), 2003.

[36] Hartl, R.: An introduction to VRP. Transoportation Logistics. Lecture, 2012.

[37] Hassanat, A.; Almohammadi, K.; Alkafaween, E.; Abunawas, E.; Hammouri, A. Prashat, S.: Choosing Mutation and Crossover Ratios for Genetic Algorithms. Information, Vol. 10(12), No. 390, 2019.

[38] Hill, S.: Orbit Fab Refuelling Interface and Service Mission Development Progress in Europe. Clean Space Days 2024. Speech, 2024.

[39] Ho, K.: Modeling and Optimization for Space Logistics Operations. In: SciTech 2024 Forum, AIAA SciTech, American Institute of Aeronautics and Astronautics, 2024.

[40] Ho, K.; Gerhard, K.; Nicholas, A.; Buck, A.; Hoffman, J.: On-Orbit Depot Architecture Using Contingency Propellant. Acta Astronautica, Vol. 96, pp. 217–226, 2014.

[41] Innocenti, M.: Orbit Transfer – Orbital Maneuvers. Orbital Mechanics Part 3. Lecture, 2021.

[42] Jackson, B.: Minimum energy maneuvering strategies for multiple satellite inspection missions. In: 2005 IEEE Aerospace Conference, IEEE Aerospace Conference, Institute of Electrical and Electronics Engineers, 2005.

[43] Jagannatha, B.; Ho, K.: Optimization of In-Space Supply Chain Design Using High-Thrust and Low-Thrust Propulsion Technologies. Journal of Spacecraft and Rockets, Vol. 55, No. 3, 2018.

[44] Jin Zhang; YaZhong Luo; GuoJin Tang: Hybrid planning for LEO long-duration multi-spacecraft rendezvous mission. Science China: Technological Sciences, Vol. 55, No. 1, pp. 233–243, 2012.

[45] Jones, A.: Chinese spacecraft reenters atmosphere ahead of new space station missions, `https://spacenews.com/chinese-spacecraft-reenters-atmosphere-ahead-of-new-space-station-missions/` (accessed 08/22/2024), 2022.

[46] Kalifa, H.: Active Debris Removal Market. ESA Clean Space Days. Speech, 2024.

[47] Katoch, S.; Chauhan, S.; Kumar, V.: A review on genetic algorithm: past, present, and future. Multimedia Tools and Applications, pp. 8091–8126, 2020.

[48] Kong, L.; Zhou, Y.: Multiobjective Mission Planning for Multiple Geosynchronous Spacecraft Refueling. International Journal of Aerospace Engineering, Vol. 2023, pp. 1–14, 2023.

[49] Kramer, H.: MEV-1 & 2 (Mission Extension Vehicle-1 and -2), https://www.eoportal.org/satellite-missions/mev-1#mission-status (accessed 08/22/2024), 2020.

[50] Laporte, G.: The Vehicle Routing Problem: An overview of exact and approximate algorithms. European Journal of Operational Research, Vol. 59, pp. 345–358, 1992.

[51] Larson, R.; Odoni, A.: Urban Operations Research. Chapter 6: Applications of Network Models, Prentice-Hall, 1981.

[52] Lavagna, M.: e.Inspector: a 12U microsat to support future IOS missions by VIS-IR imaging Proba I. Clean Space Days 2024: Towards a Sustainable Future in Space. Speech, 2024.

[53] Luu, M.; Hastings, D.: Review of On-Orbit Servicing Considerations for Low-earth Orbit Constellations. In: ASCEND 2021, AIAA ASCEND, American Institute of Aeronautics and Astronautics, 2021.

[54] Massachusetts Institute of Technology: poliastro - Astrodynamics in Python. API Reference, https://docs.poliastro.space/en/stable/api.html#api-reference (accessed 06/21/2024), 2023.

[55] Meng, B.; Huang, J.; Li, Z.; Huang, L.; Pang, Y.; Han, X.; Zhang, Z.: The orbit deployment strategy of OOS system for refueling near-earth orbit satellites. Acta Astronautica, No. 159, pp. 486–498, 2019.

[56] Moormann, D.: Raumflugmechanik I. Vorlesungsumdruck, 2022.

[57] NASA: Robotic Refueling Mission. NASAfacts. Factsheet, 2023.

[58] NASA Goddard Space Flight Center: On-Orbit Satellite Servicing Study. Project Report, 2010.

[59] O'Brien, F.; Sichler, E.: Rapid Maneuverability Requirements for On-Orbit GEO Logistics Architectures. In: SciTech 2024 Forum, AIAA SciTech, American Institute of Aeronautics and Astronautics, 2024.

[60] OrbitFab: OrbitFab. Creating the First Commercial Spacecraft Refueling Service, https://www.orbitfab.com/ (accessed 08/22/2024), 2023.

[61] OrbitFab: OrbitFab Fuel Shuttles and Depots, https://www.orbitfab.com/resources/#technical-publications (accessed 08/22/2024), 2024.

[62] OrbitFab: RAFTI Rapid Attachable Fluid Transfer Interface. Datasheet, DOC-00133, 2024.

[63] OuYang, Q.; Xu, H.: The study of comparisons of three crossover operators in genetic algorithm for solving single machine scheduling problem. International Conference on Manufacturing Science and Engineering (ICMSE 2015), pp. 293–297, 2015.

[64] Parsonson, A.: ESA Selects Companies to Develop in-Orbit Fuel Storage and Refilling Tech, `https://europeanspaceflight.com/esa-selects-companies-to-develop-in-orbit-fuel-storage-and-refilling-tech/` (accessed 10/29/2024), 2024.

[65] Peet, M.: Spacecraft Dynamics and Control. Lecture 8: Impulsive Orbital Maneuvers. Lecture, 2021.

[66] Peet, M.: Spacecraft Dynamics and Control. Lecture 9: Bi-elliptics and Out-of-Plane Maneuvers. Lecture, 2021.

[67] Peet, M.: Spacecraft Dynamics and Control. Lecture 10: Rendezvous and Targeting - Lambert's Problem. Lecture, 2021.

[68] Pontani, M.: Orbital Transfers: Optimization Methods and Recent Results. Numerical Algebra, Control and Optimization, Vol. 1, No. 3, pp. 435–485, 2011.

[69] Prieto, M.: CAT-IOD. CAT In-Orbit Demonstration Mission for a Prepared Active Debris Removal Scenario. Speech, 2024.

[70] Prussing, J.: A Class of Optimal Two-Impulse Rendezvous Using Multiple-Revolution Lambert Solutions. The Journal of the Astronautical Sciences, Vol. 48, pp. 131–148, 2000.

[71] Rainville, F. de: DEAP documentation. Distributed Evolutionary Algorithms in Python, `https://deap.readthedocs.io/en/master/index.html` (accessed 07/23/2024), 2023.

[72] Roohi, Z.; Robertson, B.; Mavris, D.: Analysis of Infrastructure to Support a Future Space Economy. In: SciTech 2024 Forum, AIAA SciTech, American Institute of Aeronautics and Astronautics, 2024.

[73] Serfonstein, Z.: Astroscale's IOS Missions. Driving Towards a Sustainable Future. Speech, 2024.

[74] Shen, H.; Tsiotras, P.: Optimal Scheduling for Servicing Multiple Satellites in a Circular Constellation. In: AIAA/AAS Astrodynamics Specialist Conference and Exhibit, Astrodynamics Specialist Conference and Exhibit, American Institute of Aeronautics and Astronautics, 2002.

[75] Shen, H.; Tsiotras, P.: Peer-to-Peer Refuelling wihtin a Satellite Constellation. In: 42nd IEEE International Conference on Decision and Control, IEEE International Conference on Decision and Control, Institute of Electrical and Electronics Engineers, 2003.

[76] Shen, H.; Tsiotras, P.: Peer-to-Peer Refuelling within a Satellite Constellation. In: 42nd IEEE International Conference on Decision and Control, IEEE International Conference on Decision and Control, Institute of Electrical and Electronics Engineers, 2003.

[77] Shimane, Y.; Gollins, N.; Ho, K.: Orbital Facility Location Problem for Satellite Constellation Servicing Depots. Journal of Spacecraft and Rockets, pp. 1–18, 2024.

[78] Sirieys, E.; Luu, M.; Weck, O. de: Multidisciplinary Design Optimization of an On-Orbit Servicing Constellation in Low Earth Orbit. In: ASCEND 2021, AIAA ASCEND, American Institute of Aeronautics and Astronautics, 2021.

[79] Smitherman, D.; Woodcock, G.: Space Transportation Infrastructure Supported By Propellant Depots. In: AIAA SPACE 2011, AIAA SPACE Conference & Exposition, American Institute of Aeronautics and Astronautics, 2011.

[80] Sorenson, S.; Pinkley, S.: Multi-orbit routing and scheduling of refuellable on-orbit servicing space robots. Computer & Industrial Engineering, Vol. 176, 2023.

[81] Steimle, C.; Woicke, S.; Metrailler, L.: ClearSpace-1 In-Orbit Demonstration Mission. Clean Space Days. Speech, 2024.

[82] Takubo, Y.; Shimane, Y.; Ho, K.: Optimization of Earth-Moon Low-Thrust-Enhanced Low-Energy Transfer. In: AAS/ AIAA Astrodynamics Specialist Conference, Astrodynamics Specialist Conference, American American Astronautical Society; Institute of Aeronautics and Astronautics, 2023.

[83] Tibert, G.: Earth Satellite Operations. SD2900 Fundamentals of Spaceflight. Lecture, 2023.

[84] Tiffin, D.; Friz, P.: The Space Superhighway: Systems Analysis of an In-Space Logistics Network. In: ASCEND 2022, AIAA ASCEND, American Institute of Aeronautics and Astronautics, 2022.

[85] Tincelin, Y.: Enabling a European In-Space Transportation ecosystem. In: Aerospace Europe Conference - 10th EUCASS - 9th CEAS, Aerospace Europe Conference, European Conference for Aerospace Sciences (EUCASS); Council of European Aerospace Societies (CEAS), 2023.

[86] Tincelin, Y.: In-Space Transportation Proof of Concept-2 (POC-2): In-Orbit Refilling. Preliminary Demonstration Objectives: Future Space Transpotation Preparation - Venture 1, FLPP Space Logistics & Technology Disruptors Element. Technical Note, 2023.

[87] Tokudome, S.; Maru, Y.; Nonaka, S.: Medium-to long-term strategies in the field of space transportation systems formulated by the Institute of Space and Astronautical Science of the Japan Aerospace Exploration Agency under the Inter-University Research Institute System, 2024.

[88] Tsiotras, P.; Nailly, A. de: Comparison Betweeen Peer-to-Peer and Single-Spacecraft Refueling Strategies for Spacecraft in Circular Orbits. In: Infotech@Aerospace 2005, Infotech@Aerospace, American Institute of Aeronautics and Astronautics, 2005.

[89] Umbarkar, A.; Sheth, P.: Crossover Operators in Genetic Algorithms. ICTACT Journal on Soft Computing, Vol. 6, No. 1, pp. 1083–1092, 2015.

[90] Union of Concerned Scientists: The UCS Satellite Database. User Manual, 1-1-17, 2023.

[91] Union of Concerned Scientists: UCS Satellite Database. In-depth details on the 7560 satellites currently orbiting Earth, including their country of origin, purpose, and other operational details, `https://www.ucsusa.org/resources/satellite-database` (accessed 05/22/2024), 2023.

[92] USAF: Propellant Hydrazine, MIL-PRF-26536F, 2011.

[93] Vallado, D.; McClain, W.: Fundamentals of Astrodynamics and Applications. Fourth Edition. Space Technology Library, Hawthorne, California: Microcosm Press and Springer, 2013.

[94] Verstraete, A.; St.Louis, N.; Hudson, J.: GEO Robotic Servicer Trajectory Optimization. In: AIAA SPACE 2016, AIAA SPACE Conferences and Expositions, American Institute of Aeronautics and Astronautics, 2016.

[95] Welberg, D.; Determann, B.; Hessel, C.; Birkc, T.; Da Büchner Costa, T.: The ASTRIS Kickstage Propulsion System Development Status & Outlook. Space Propulsion 2022, SP2022_329, 2022.

[96] Weng, W.: Artificial Intelligence - Genetic Algorithms. In: A Beginner's Guide to Informatics and Artificial Intelligence. Springer, pp. 39–49, (cit. on pp. 11, 23, 52), 2024.

[97] Williams, B. G.: Handbook of Geostationary Orbits. Celestial Mechanics and Dynamical Astronomy, Vol. 65, No. 4, pp. 459–460, 1997.

[98] Yu, J.; Hao, D.: Optimal mission planning for refuelling LEO satellites with peer-to-peer strategy. IOP Conference Series: Materials Science and Engineering, Vol. 715, No. 1, 2020.

[99] Zhang, J.; Parks, G.; Luo, Y.; Tang, G.: Multispacecraft Refueling Optimization Considering the J2 Perturbation and Window Constraints. Journal of Guidance, Control, and Dynamics, Vol. 37, No. 1, pp. 111–122, 2014.

[100] Zhang, T.; Yang, Y.; Wang, B.; Li, Z.; Shen, H.; Li, H.: Optimal scheduling for location geosyncrhonous satellites refueling problem. Acta Astronautica, Vol. 163, pp. 264–271, 2019.

[101] Zhao, S.; Gurfil, P.; Zhang, J.: Optimal Servicing of Geostationary Satellites Considering Earth's Triaxiality and Lunisolar Effects. Journal of Guidance, Control, and Dynamics, Vol. 39, No. 10, pp. 2219–2231, 2016.

[102] Zhou, Y.; Yan, Y.; Huang, X.; Kong, L.: Mission planning optimization for multiple geosynchronous satellites refueling. Advances in Space Research, Vol. 56, pp. 2612–2625, 2015.

[103] Zhou, Y.; Yan, Y.; Huang, X.; Yang, Y.; Zhang, H.: Mission planning optimization for the visual inspection of multiple geosynchronous satellites. Engineering Optimization, Vol. 47, No. 11, pp. 1543–1563, 2015.

[104] Zhu, X.; Chen, J.; Zhang, C.; Qiao, B.: Optimal fuel station arrangement for multiple GEO spacecraft refueling mission. Advances in Space Research, Vol. 66, No. 8, pp. 1924–1936, 2020.

[105] Zhu, X.; Zhang, C.; Su, R.; Chen, J.; Wan, X.: Orbit determination for fuel station in multiple SSO spacecraft refueling considering the J2 perturbation. Aerospace Science and Technology, Vol. 105, No. 1, 2020.